

1 SEARCH FOR PRODUCTION OF A HIGGS BOSON AND A SINGLE TOP  
2 QUARK IN MULTILEPTON FINAL STATES IN  $pp$  COLLISIONS AT  $\sqrt{s} = 13$   
3 TeV.

4 by

5 Jose Andres Monroy Montañez

# A DISSERTATION

7 Presented to the Faculty of

8 The Graduate College at the University of Nebraska

9 In Partial Fulfilment of Requirements

10 For the Degree of Doctor of Philosophy

11 Major: Physics and Astronomy

12 Under the Supervision of Kenneth Bloom and Aaron Dominguez

13 Lincoln, Nebraska

14 July, 2018

15 SEARCH FOR PRODUCTION OF A HIGGS BOSON AND A SINGLE TOP  
16 QUARK IN MULTILEPTON FINAL STATES IN pp COLLISIONS AT  $\sqrt{s} = 13$   
17 TeV.

18 Jose Andres Monroy Montañez, Ph.D.

19 University of Nebraska, 2018

20 Adviser: Kenneth Bloom and Aaron Dominguez

# **21 Table of Contents**

<b>22 Table of Contents</b>	<b>iii</b>
<b>23 List of Figures</b>	<b>vii</b>
<b>24 List of Tables</b>	<b>x</b>
<b>25 1 INTRODUCTION</b>	<b>1</b>
<b>26 2 Theoretical approach</b>	<b>2</b>
27     2.1 Introduction . . . . .	2
28     2.2 Standard model of particle physics . . . . .	3
29         2.2.1 Fermions . . . . .	5
30             2.2.1.1 Leptons . . . . .	6
31             2.2.1.2 Quarks . . . . .	9
32         2.2.2 Fundamental interactions . . . . .	13
33         2.2.3 Gauge Bosons . . . . .	18
34     2.3 Electroweak unification and the Higgs mechanism . . . . .	20
35         2.3.1 Spontaneous symmetry breaking (SSB) . . . . .	28
36         2.3.2 Higgs mechanism . . . . .	32
37         2.3.3 Masses of the gauge bosons . . . . .	34

38	2.3.4	Masses of the fermions . . . . .	35
39	2.3.5	The Higgs field . . . . .	36
40	2.3.6	Higgs boson production mechanisms at LHC. . . . .	37
41	2.3.7	Higgs decay channels . . . . .	41
42	2.4	Associated Production of Higgs Boson and Single Top Quark. . . . .	42
43	2.5	The CP-mixing in tH processes . . . . .	47
44	2.6	Experimental status of anomalous Higg-fermion coupling. . . . .	51
45	<b>3</b>	<b>The CMS experiment at the LHC</b>	<b>53</b>
46	3.1	Introduction . . . . .	53
47	3.2	The LHC . . . . .	54
48	3.3	The CMS experiment . . . . .	64
49	3.3.1	Coordinate system . . . . .	66
50	3.3.2	Pixels detector . . . . .	67
51	3.3.3	Silicon strip tracker . . . . .	69
52	3.3.4	Electromagnetic calorimeter . . . . .	71
53	3.3.5	Hadronic calorimeter . . . . .	72
54	3.3.6	Superconducting solenoid magnet . . . . .	74
55	3.3.7	Muon system . . . . .	75
56	3.3.8	trigger system - HLT- L1 . . . . .	76
57	3.3.9	computing model . . . . .	78
58	3.4	Event generation simulation and reconstruction . . . . .	78
59	3.4.1	event generation . . . . .	78
60	3.4.2	Hard scattering . . . . .	78
61	3.4.3	parton shower . . . . .	78
62	3.4.4	hadronization and decays . . . . .	78

63	3.4.5	underlying events and pileup . . . . .	78
64	3.4.6	MC - MadEvent, MadGraph and madgraphNLO, powheg, pythia, tauola . . . . .	78
65	3.4.7	detector simulation . . . . .	78
66	3.4.8	event reconstruction- particle flow algorithm, vertexing , muon reco, electron reco, photon and hadron reco, jets reco, anti-kt algoritm, jet energy corrections, btagging, MET . . . . .	78
67	3.4.9	MVA methods, NN, BDT, boosting, overtraining, variable ranking . . . . .	78
68	3.4.10	statistical inference, likelihood parametrization . . . . .	78
69	3.4.11	nuisance paraeters . . . . .	78
70	3.4.12	exclusion limits . . . . .	78
71	3.4.13	asymptotic limits . . . . .	78
72	<b>4</b>	<b>Search for production of a Higgs boson and a single top quark in multilepton final states in pp collisions at <math>\sqrt{s} = 13</math> TeV</b>	<b>79</b>
73	4.1	Introduction . . . . .	79
74	4.2	Data and MC Samples . . . . .	81
75	4.2.1	Full 2016 dataset and MC samples . . . . .	81
76	4.2.2	Triggers . . . . .	84
77	4.2.2.1	Trigger efficiency scale factors . . . . .	84
78	4.3	Object Identification and event selection . . . . .	85
79	4.3.1	Jets and $b$ tagging . . . . .	85
80	4.3.2	Lepton selection . . . . .	86
81	4.3.3	Lepton selection efficiency . . . . .	87
82	4.4	Background predictions . . . . .	88

88	4.5 Signal discrimination . . . . .	89
89	4.5.1 Classifiers response . . . . .	93
90	4.6 Additional discriminating variables . . . . .	96
91	<b>5 The CMS forward pixel detector</b>	<b>99</b>
92	5.0.1 The phase 1 FPix upgrade . . . . .	99
93	5.0.2 FPix module production line . . . . .	99
94	5.0.3 The Gluing stage . . . . .	99
95	5.0.4 The Encapsulation stage . . . . .	99
96	5.0.5 The FPix module production yields . . . . .	99
97	<b>Bibliography</b>	<b>99</b>
98	<b>References</b>	<b>100</b>

## <sup>99</sup> List of Figures

100	1.1	$^{14}N$ neutron capture in a PECVD polymerized pyridine film. The Q-value of this reaction is 626 keV. Taken from [22] . . . . .	1
102	2.1	Standard model of particle physics. . . . .	4
103	2.2	WI transformations between quarks . . . . .	12
104	2.3	Fundamental interactions in nature. . . . .	13
105	2.4	SM interactions diagrams . . . . .	14
106	2.5	Neutral current processes . . . . .	21
107	2.6	Spontaneous symmetry breaking mechanism . . . . .	28
108	2.7	SSB Potential form . . . . .	30
109	2.8	Potential for complex scalar field . . . . .	30
110	2.9	SSB mechanism for complex scalar field . . . . .	31
111	2.10	Proton-Proton collision . . . . .	38
112	2.11	Higgs production mechanism Feynman diagrams . . . . .	39
113	2.12	Higgs production cross section and decay branching ratios . . . . .	40
114	2.13	Associated Higgs production mechanism Feynman diagrams . . . . .	43
115	2.14	Cross section for $tHq$ process as a function of $\kappa_t$ . . . . .	45
116	2.15	Cross section for $tHW$ process as a function of $\kappa_{Htt}$ . . . . .	46
117	2.16	NLO cross section for $tX_0$ and $t\bar{t}X_0$ . . . . .	49

118	2.17 NLO cross section for $tWX_0, t\bar{t}X_0$ . . . . .	50
119	2.18 Combined coupling modifiers $\kappa_t$ - $\kappa_V$ fits of ATLAS and CMS. . . . .	51
120	3.1 CERN accelerator complex . . . . .	54
121	3.2 LHC protons source and first acceleration stage. . . . .	55
122	3.3 The LINAC2 accelerating system at CERN. . . . .	56
123	3.4 LHC layout and RF cavities module. . . . .	57
124	3.5 LHC dipole magnet. . . . .	59
125	3.6 2016 CMS Integrated luminosity . . . . .	61
126	3.7 LHC interaction points . . . . .	62
127	3.8 Multiple pp collision bunch crossing at CMS. . . . .	64
128	3.9 CMS detector drawing . . . . .	65
129	3.10 CMS coordinate system . . . . .	66
130	3.11 CMS pixel detector schematic view. . . . .	68
131	3.12 SST Schematic view. . . . .	69
132	3.13 CMS ECAL schematic view . . . . .	71
133	3.14 CMS HCAL schematic view . . . . .	73
134	3.15 CMS solenoid magnet . . . . .	74
135	3.16 CMS Muon system schematic view . . . . .	75
136	4.1 The two leading-order diagrams of $tHq$ production. . . . .	80
137	4.2 Input variables to the BDT for signal discrimination normalized . . . . .	90
138	4.3 Input variables to the BDT for signal discrimination not normalized. . . . .	92
139	4.4 BDT inputs as seen by TMVA against $t\bar{t}$ . . . . .	93
140	4.5 BDT inputs as seen by TMVA against $t\bar{t}\bar{V}$ . . . . .	94
141	4.6 Correlation matrices for the input variables in the TMVA. . . . .	95
142	4.7 MVA classifiers performance. . . . .	95

143	4.8 Additional discriminating variables distributions. . . . .	97
-----	--	----

# <sup>144</sup> List of Tables

145	2.1	Fermions of the SM. . . . .	5
146	2.2	Fermion masses. . . . .	6
147	2.3	Leptons properties. . . . .	9
148	2.4	Quarks properties. . . . .	9
149	2.5	Fermion weak isospin and weak hypercharge multiplets. . . . .	11
150	2.6	Fundamental interactions features. . . . .	15
151	2.7	SM gauge bosons. . . . .	20
152	2.8	Higgs boson properties. . . . .	37
153	2.9	Predicted branching ratios for a SM Higgs boson with $m_H = 125 \text{ GeV}/c^2$ . . . . .	42
154	2.10	Predicted SM cross sections for $tH$ production at $\sqrt{s} = 13 \text{ TeV}$ . . . . .	44
155	2.11	Predicted enhancement of the $tHq$ and $tHW$ cross sections at LHC . . . . .	47
156	4.1	Signal samples and their cross section and branching fraction. . . . .	81
157	4.2	$\kappa_V$ and $\kappa_t$ combinations. . . . .	82
158	4.3	List of background samples used in this analysis (CMSSW 80X). . . . .	83
159	4.4	Leading-order $t\bar{t}W$ and $t\bar{t}Z$ samples used in the signal BDT training. . . .	83
160	4.5	Table of high-level triggers that we consider in the analysis. . . . .	84
161	4.6	Trigger efficiency scale factors and associated uncertainties. . . . .	85
162	4.7	Requirements on each of the three muon selections. . . . .	86

163	4.8	Criteria for each of the three electron selections.	87
164	4.9	MVA input discriminating variables	91
165	4.10	TMVA input variables ranking for BDTA_GRAD method	96
166	4.11	TMVA configuration used in the BDT training.	96
167	4.12	ROC-integral for all the testing cases.	98

<sup>168</sup> Chapter 1

<sup>169</sup> INTRODUCTION

**Figure 1.1:**  $^{14}N$  neutron capture in a PECVD polymerized pyridine film. The Q-value of this reaction is 626 keV. Taken from [22]

# <sup>170</sup> Chapter 2

## <sup>171</sup> Theoretical approach

### <sup>172</sup> 2.1 Introduction

<sup>173</sup> The physical description of the universe is a challenge that physicists have faced by  
<sup>174</sup> making theories that refine existing principles and proposing new ones in an attempt  
<sup>175</sup> to embrace emerging facts and phenomena.

<sup>176</sup>

<sup>177</sup> At the end of 1940s Julian Schwinger [11] and Richard P. Feynman [12], based in  
<sup>178</sup> the work of Sin-Itiro Tomonaga [13], developed an electromagnetic theory consistent  
<sup>179</sup> with special relativity and quantum mechanics that describes how matter and light  
<sup>180</sup> interact; the so-called “quantum eletrodynamics” (QED) had born.

<sup>181</sup>

<sup>182</sup> QED has become the guide in the development of theories that describe the universe.  
<sup>183</sup> It was the first example of a quantum field theory (QFT), which is the theoretical  
<sup>184</sup> framework for building quantum mechanical models that describes particles and their  
<sup>185</sup> interactions. QFT is composed of a set of mathematical tools that combines classical  
<sup>186</sup> fields, special relativity and quantum mechanics, while keeping the quantum point

187 particles and locality ideas.

188 This chapter gives an overview of the standard model of particle physics, starting  
 189 with a description of the particles and interactions that compose it, followed by a  
 190 description of the electroweak interaction, the Higgs boson and the associated pro-  
 191 duction of Higgs boson and a single top quark ( $tH$ ). The description contained in  
 192 this chapter is based on references [1–3].

## 193 2.2 Standard model of particle physics

194 Particle physics at the fundamental level is modeled in terms of a collection of in-  
 195 teracting particles and fields in a theory known as the “standard model of particle  
 196 physics (SM)”<sup>1</sup>.

197

198 The full picture of the SM is composed of three fields<sup>2</sup>, whose excitations are inter-  
 199 preted as particles called mediators or force-carriers; a set of fields, whose excitations  
 200 are interpreted as elementary particles, interacting through the exchange of those  
 201 mediators and a field that gives the mass to elementary particles. Figure 2.1 shows  
 202 an scheme of the SM particles organization. In addition to the particles in the scheme  
 203 (but not listed in it), their corresponding anti-particles, with opposite quantum num-  
 204 bers, are also part of the picture; some particles are their own anti-particles, like  
 205 photon or Higgs, or anti-particle is already listed like in the  $W^+$  and  $W^-$  case.

206

207 The mathematical formulation of the SM is based on group theory and the use of

---

<sup>1</sup> The formal and complete treatment of the SM is out of the scope of this document, however a plenty of textbooks describing it at several levels are available in the literature. The treatment in “An Introduction To Quantum Field Theory (Frontiers in Physics)” by Michael E. Peskin and Dan V. Schroeder is quite comprehensive and detailed.

<sup>2</sup> Note that gravitational field is not included in the standard model formulation

## Standard Model of Elementary Particles

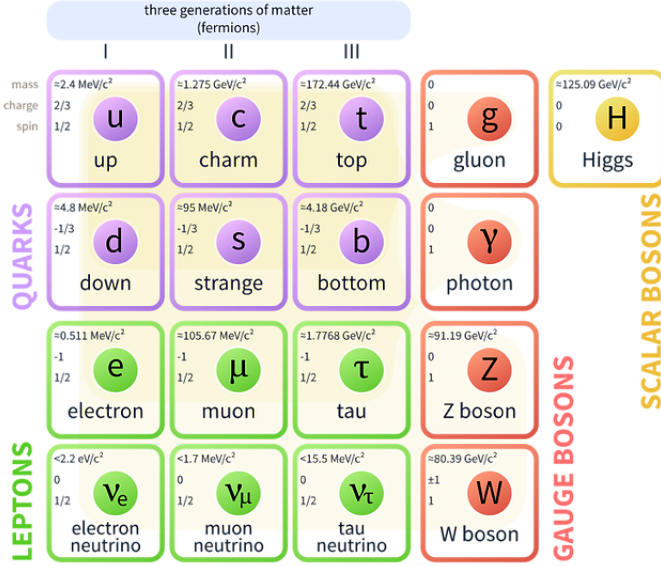


**Figure 2.1:** Schematic representation of the Standard model of particle physics. SM is a theoretical model intended to describe three of the four fundamental forces of the universe in terms of a set of particles and their interactions. [18].

208 Noether's theorem [17] which states that for a physical system modeled by a La-  
 209 grangian that is invariant under a group of transformations a conservation law is  
 210 expected. For instance, a system described by a time-independent Lagrangian is  
 211 invariant (symmetric) under time changes (transformations) with the total energy  
 212 conservation law as the expected conservation law. In QED, the charge operator  
 213 ( $Q$ ) is the generator of the  $U(1)$  symmetry which according to the Noether's theorem  
 214 means that there is a conserved quantity; this conserved quantity is the electric charge  
 215 and thus the law conservation of electric charge is established.

216

217 In the SM, the symmetry group  $SU(3)_C \otimes SU(2)_L \otimes U(1)_Y$  describes three of the  
 218 four fundamental interactions in nature(see section 2.2.2): strong interaction(SI),  
 219 weak interaction(WI) and electromagnetic interactions (EI) in terms of symmetries

220 associated to physical quantities:

221 • Strong:  $SU(3)_C$  associated to color charge

222 • Weak:  $SU(2)_L$  associated to weak isospin and chirality

223 • Electromagnetic:  $U(1)_Y$  associated to weak hypercharge and electric charge

224 It will be shown that the electromagnetic and weak interactions are combined in  
 225 the so-called electroweak interaction where chirality, hypercharge, weak isospin and  
 226 electric charge are the central concepts.

227 **2.2.1 Fermions**

228 The basic constituents of the ordinary matter at the lowest level, which form the set  
 229 of elementary particles in the SM formulation, are quarks and leptons. All of them  
 230 have spin 1/2, therefore they are classified as fermions since they obey Fermi-Dirac  
 231 statistics. There are six “flavors” of quarks and three of leptons organized in three  
 232 generations, or families, as shown in table 2.1.

233

Generation				
	Type	1st	2nd	3rd
Leptons	Charged	Electron (e)	Moun( $\mu$ )	Tau ( $\tau$ )
	Neutral	Electron neutrino ( $\nu_e$ )	Muon neutrino ( $\nu_\mu$ )	Tau neutrino ( $\nu_\tau$ )
Quarks	Up-type	Up (u)	Charm (c)	Top (t)
	Down-type	Down (d)	Strange (s)	Bottom (b)

**Table 2.1:** Fermions of the SM. There are six flavors of quarks and three of leptons, organized in three generations, or families, composed of two pairs of closely related particles. The close relationship is motivated by the fact that WI between leptons is limited to the members of the same generation; WI between quarks is not limited but greatly favoured, to same generation members.

234

235 There is a mass hierarchy between generations (see table 2.2), where the higher gener-  
 236 ation particles decays to the lower one, which can explain why the ordinary matter is  
 237 made of particles in the first generation. In the SM, neutrinos are modeled as massless  
 238 particles so they are not subject to this mass hierarchy; however, today it is known  
 239 that neutrinos are massive so the hierarchy could be restated. The reason behind this  
 240 mass hierarchy is one of the most important open questions in particle physics, and  
 241 it becomes more puzzling when noticing that the mass difference between first and  
 242 second generation fermions is small compared to the mass difference with respect to  
 243 the third generation.

Lepton	Mass (MeV/c <sup>2</sup> )	Quark	Mass (MeV/c <sup>2</sup> )
e	0.51	u	2.2
$\mu$	105.65	c	$1.28 \times 10^3$
$\tau$	1776.86	t	$173.1 \times 10^3$
$\nu_e$	Unknown	d	4.7
$\nu_\mu$	Unknown	s	96
$\tau_\mu$	Unknown	b	$4.18 \times 10^3$

**Table 2.2:** Fermion masses [21]. Generations differ by mass in a way that have been interpreted as a masss hierarchy. Approximate values with no uncertainties are used, for comparison purpose.

244

245 Usually, the second and third generation fermions are produced in high energy pro-  
 246 cesses, like the ones recreated in particle accelerators.

### 247 2.2.1.1 Leptons

248 A lepton is an elementary particle that is not subject to the SI. As seen in table 2.1,  
 249 there are two types of leptons, the charged ones (electron, muon and tau) and the  
 250 neutral ones (the three neutrinos). The electric charge (Q) is the property that gives  
 251 leptons the ability to participate in the EI. From the classical point of view, Q plays

252 a central role determining, among others, the strength of the electric field through  
253 which the electromagnetic force is exerted. It is clear that neutrinos are not affected  
254 by EI because they don't carry electric charge.

255

256 Another feature of the leptons that is fundamental in the mathematical description  
257 of the SM is the chirality, which is closely related to spin and helicity. Helicity defines  
258 the handedness of a particle by relating its spin and momentum such that if they  
259 are parallel then the particle is right-handed; if spin and momentum are antiparallel  
260 the particle is said to be left-handed. The study of parity conservation (or viola-  
261 tion) in  $\beta$ -decay has shown that only left-handed electrons/neutrinos or right-handed  
262 positrons/anti-neutrinos are created [19]; the inclusion of that feature in the theory  
263 was achieved by using projection operators for helicity, however, helicity is frame de-  
264 pendent for massive particles which makes it not Lorentz invariant and then another  
265 related attribute has to be used: *chirality*.

266

267 Chirality is a purely quantum attribute which makes it not so easy to describe in  
268 graphical terms but it defines how the wave function of a particle transforms under  
269 certain rotations. As with helicity, there are two chiral states, left-handed chiral (L)  
270 and right-handed chiral (R). In the highly relativistic limit where  $E \approx p \gg m$  helicity  
271 and chirality converge, becoming exactly the same for massless particles.

272

273 In the following, when referring to left-handed (right-handed) it will mean left-handed  
274 chiral (right-handed chiral). The fundamental fact about chirality is that while EI  
275 and SI are not sensitive to chirality, in WI left-handed and right-handed fermions are  
276 treated asymmetrically, such that only left handed fermions and right-handed anti-  
277 fermions are allowed to couple to WI mediators, which is a violation of parity. The

278 way to translate this statement in a formal mathematical formulation is based on the  
 279 isospin symmetry group  $SU(2)_L$ .

280

281 Each generation of leptons is seen as a weak isospin doublet.<sup>3</sup> The left-handed charged  
 282 lepton and its associated left-handed neutrino are arranged in doublets of weak isospin  
 283  $T=1/2$  while their right-handed partners are singlets:

$$\begin{pmatrix} \nu_l \\ l \end{pmatrix}_L, l_R := \begin{pmatrix} \nu_e \\ e \end{pmatrix}_L, \begin{pmatrix} \nu_\mu \\ \mu \end{pmatrix}_L, \begin{pmatrix} \nu_\tau \\ \tau \end{pmatrix}_L, e_R, \mu_R, \tau_R, \nu_{eR}, \nu_{\mu R}, \nu_{\tau R} \quad (2.1)$$

284 The isospin third component refers to the eigenvalues of the weak isospin operator  
 285 which for doublets is  $T_3 = \pm 1/2$ , while for singlets it is  $T_3 = 0$ . The physical meaning  
 286 of this doublet-singlet arrangement falls in that the WI couples the two particles in  
 287 the doublet by exchanging the interaction mediator while the singlet member is not  
 288 involved in WI. The main properties of the leptons are summarized in table 2.3.

289

290 Altough all three flavor neutrinos have been observed, their masses remain unknown  
 291 and only some estimations have been made [20]. The main reason is that the fla-  
 292 vor eigenstates are not the same as the mass eigenstates which implies that when  
 293 a neutrino is created its mass state is a linear combination of the three mass eigen-  
 294 states and experiments can only probe the squared difference of the masses. The  
 295 Pontecorvo-Maki-Nakagawa-Sakata (PMNS) mixing matrix encode the relationship  
 296 between flavor and mass eigenstates.

297

---

<sup>3</sup> The weak isospin is an analogy of the isospin symmetry in strong interaction where neutron and proton are affected equally by strong force but differ in their charge.

Lepton	Q(e)	$T_3$	$L_e$	$L_\mu$	$L_\tau$	Lifetime (s)
Electron (e)	-1	-1/2	1	0	0	Stable
Electron neutrino( $\nu_e$ )	0	1/2	1	0	0	Unknown
Muon ( $\mu$ )	-1	-1/2	0	1	0	$2.19 \times 10^{-6}$
Muon neutrino ( $\nu_\mu$ )	0	1/2	0	1	0	Unknown
Tau ( $\tau$ )	-1	-1/2	0	0	1	$290.3 \times 10^{-15}$
Tau neutrino ( $\tau_\mu$ )	0	1/2	0	0	1	Unknown

**Table 2.3:** Leptons properties [21]. Q: electric charge,  $T_3$ : weak isospin. Only left-handed leptons and right-handed anti-leptons participate in the WI. Anti-particles with inverted  $T_3$ , Q and lepton number complete the leptons set but are not listed. Right-handed leptons and left-handed anti-leptons, neither listed, form weak isospin singlets with  $T_3 = 0$  and do not take part in the weak interaction.

### 298 2.2.1.2 Quarks

299 Quarks are the basic constituents of protons and neutrons. The way quarks join to  
300 form bound states, called “hadrons”, is through the SI. Quarks are affected by all the  
301 fundamental interactions which means that they carry all the four types of charges:  
302 color, electric charge, weak isospin and mass.

Flavor	Q(e)	$I_3$	$T_3$	B	C	S	T	$B'$	Y	Color
Up (u)	2/3	1/2	1/2	1/3	0	0	0	0	1/3	r,b,g
Charm (c)	2/3	0	1/2	1/3	1	0	0	0	4/3	r,b,g
Top(t)	2/3	0	1/2	1/3	0	0	1	0	4/3	r,b,g
Down(d)	-1/3	-1/2	-1/2	1/3	0	0	0	0	1/3	r,b,g
Strange(s)	-1/3	0	-1/2	1/3	0	-1	0	0	-2/3	r,b,g
Bottom(b)	-1/3	0	-1/2	1/3	0	0	0	-1	-2/3	r,b,g

**Table 2.4:** Quarks properties [21]. Q: electric charge,  $I_3$ : isospin,  $T_3$ : weak isospin, B: baryon number, C: charmness, S: strangeness, T: topness,  $B'$ : bottomness, Y: hypercharge. Anti-quarks posses the same mass and spin as quarks but all charges (color, flavor numbers) have opposite sign.

303

304 Table 2.4 summarizes the features of quarks, among which the most particular is  
305 their fractional electric charge. Note that fractional charge is not a problem, given  
306 that quarks are not found isolated, but serves to explain how composed particles are

307 formed out of two or more valence quarks<sup>4</sup>.

308

309 Color charge is the responsible for the SI between quarks and is the symmetry  
 310 ( $SU(3)_C$ ) that defines the formalism to describe SI. There are three colors: red (r),  
 311 blue(b) and green(g) and their corresponding three anti-colors; thus each quark carries  
 312 one color unit while anti-quarks carries one anti-color unit. As said above, quarks are  
 313 not allowed to be isolated due to the color confinement effect, therefore their features  
 314 have been studied indirectly by observing their bound states created when:

315 • one quark with a color charge is attracted by an anti-quark with the correspond-  
 316 ing anti-color charge forming a colorless particle called a “meson.”

317 • three quarks (anti-quarks) with different color (anti-color) charges are attracted  
 318 among them forming a colorless particle called a “baryon(anti-baryon).”

319 In the first version of the quark model (1964), M. Gell-Mann [22] and G. Zweig  
 320 [23,24] developed a consistent way to classify hadrons according to their properties.  
 321 Only three quarks (u, d, s) were involved in a scheme in which all baryons have  
 322 baryon number  $B=1$  and therefore quarks have  $B=1/3$ ; non-baryons have  $B=0$ . The  
 323 scheme organizes baryons in a two-dimensional space ( $I_3 - Y$ );  $Y$  (hypercharge) and  $I_3$   
 324 (isospin) are quantum numbers related by the Gell-Mann-Nishijima formula [25, 26]:

$$Q = I_3 + \frac{Y}{2} \quad (2.2)$$

325 where  $Y = B + S + C + T + B'$  are the quantum numbers listed in table 2.4. Baryon  
 326 number is conserved in SI and EI which means that single quarks cannot be created

---

<sup>4</sup> Hadrons can contain an indefinite number of virtual quarks and gluons, known as the quark and gluon sea, but only the valence quarks determine hadrons' quantum numbers.

327 but in pairs  $q - \bar{q}$ .

328

329 There are six quark flavors organized in three generations (see table 2.1) following a  
 330 mass hierarchy which, again, implies that higher generations decay to first generation  
 331 quarks.

	Quarks			$T_3$	$Y_W$	Leptons			$T_3$	$Y_W$
Doublets	$(\frac{u}{d'})_L$	$(\frac{c}{s'})_L$	$(\frac{t}{b'})_L$	$(\frac{1/2}{-1/2})$	1/3	$(\frac{\nu_e}{e})_L$	$(\frac{\nu_\mu}{\mu})_L$	$(\frac{\nu_\tau}{\tau})_L$	$(\frac{1/2}{-1/2})$	-1
Singlets	$u_R$	$c_R$	$t_R$	0	4/3	$\nu_{eR}$	$\nu_{\mu R}$	$\nu_{\tau R}$	0	-2

**Table 2.5:** Fermion weak isospin and weak hypercharge multiplets. Weak hypercharge is calculated through the Gell-Mann-Nishijima formula 2.2 but using the weak isospin and charge for quarks.

332

333 Isospin doublets of quarks are also defined (see table 2.5) and as for neutrinos, the  
 334 mass eigenstates are not the same as the WI eigenstates which means that members of  
 335 different quark generations are connected by the WI mediator; thus, up-type quarks  
 336 are coupled not to down-type quarks directly but to a superposition of down-type  
 337 quarks ( $q'_d$ ) via WI according to:

$$338 \quad q'_d = V_{CKM} q_d$$

$$\begin{pmatrix} d' \\ s' \\ b' \end{pmatrix} = \begin{pmatrix} V_{ud} & V_{us} & V_{ub} \\ V_{cd} & V_{cs} & V_{cb} \\ V_{td} & V_{ts} & V_{tb} \end{pmatrix} \begin{pmatrix} d \\ s \\ b \end{pmatrix} \quad (2.3)$$

339 where  $V_{CKM}$  is known as Cabibbo-Kobayashi-Maskawa (CKM) mixing matrix [27,28].  
 340 The weak decays of quarks are represented in the diagram of figure 2.2; again the  
 341 CKM matrix plays a central role since it contains the probabilities for the different

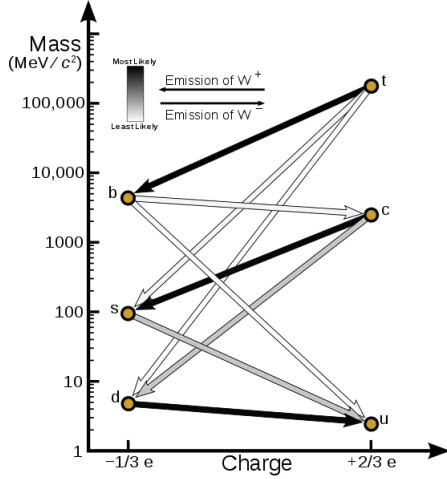


**Figure 2.2:** Transformations between quarks through WI. Higher generations quarks decay to first generation quarks by emitting a W boson. The arrow color indicates the likelihood of the transition according to the grey scale in the top left side which represent the CKM matrix parameters [29].

342 quark decay channels, in particular, note that quark decays are greatly favored be-  
343 tween generation members.

344

345 CKM matrix is a  $3 \times 3$  unitary matrix parametrized by three mixing angles and  
346 the *CP-mixing phase*; the latter is the parameter responsible for the Charge-Parity  
347 symmetry violation (CP-violation) in the SM. The fact that the b quark decays almost  
348 all the times to a top quark is exploited in this thesis when making the selection of  
349 the signal events by requiring the presence of a jet tagged as a jet coming from a  
350 b quark in the final state. The effect of the *CP-mixing phase* on the cross section of  
351 associated production of Higgs boson and a single top process is also explored in this  
352 thesis.

## Fundamental interactions.

Illustration: Typoform

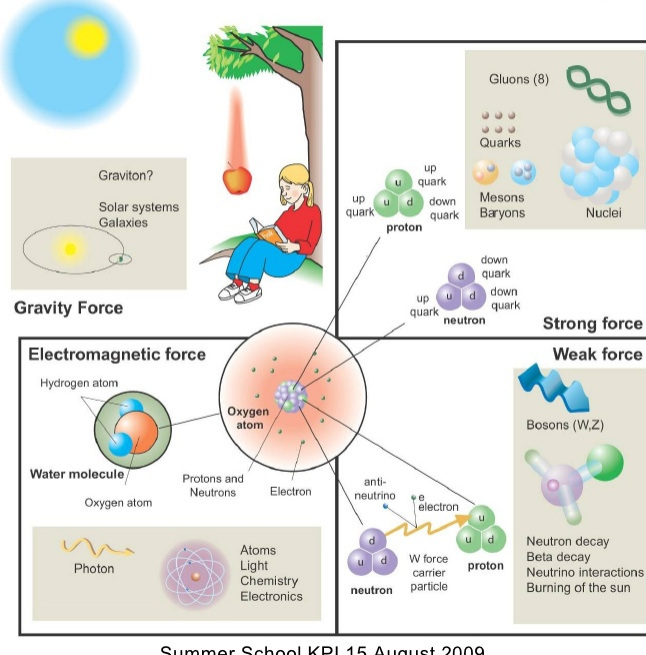


**Figure 2.3:** Fundamental interactions in nature. Despite the many manifestations of forces in nature, we can track all of them back to one of the fundamental interactions. The most common forces are gravity and electromagnetic given that all of us are subject and experience them in everyday life.

### 353 2.2.2 Fundamental interactions

354 Even though there are many manifestations of force in nature, like the ones represented in figure 2.3, we can classify all of them into one of four fundamental interactions:

- 357 • *Electromagnetic interaction (EI)* affects particles that are “electrically charged,”  
 358 like electrons and protons. It is described by QED combining quantum mechanics,  
 359 special relativity and electromagnetism in order to explain how particles  
 360 with electric charge interact through the exchange of photons, therefore, one  
 361 says that “Electromagnetic Force” is mediated by “photons”. Figure 2.4a. shows  
 362 a graphical representation, known as “feynman diagram”, of electron-electron

363 scattering.

364 • *Strong interaction (SI)* described by Quantum Chromodynamics (QCD). Hadrons  
 365 like proton and neutron have internal structure given that they are composed  
 366 of two or more valence quarks<sup>5</sup>. Quarks have fractional electric charge which  
 367 means that they are subject to electromagnetic interaction and in the case of the  
 368 proton they should break apart due to electrostatic repulsion; however, quarks  
 369 are held together inside the hadrons against their electrostatic repulsion by the  
 370 “Strong Force” through the exchange of “gluons.” The analog to the electric  
 371 charge is the “color charge”. Electrons and photons are elementary particles  
 372 as quarks but they don’t carry color charge, therefore they are not subject to  
 373 SI. The feynman diagram for gluon exchange between quarks is shown in figure  
 374 2.4b.

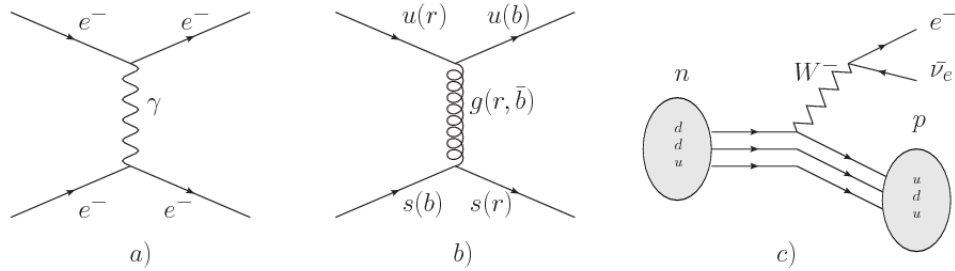


**Figure 2.4:** Feynman diagrams representing the interactions in SM; a) EI:  $e$ - $e$  scattering; b) SI: gluon exchange between quarks ; c) WI:  $\beta$ -decay

375 • *Weak interaction (WI)* described by the weak theory (WT), is responsible, for  
 376 instance, for the radioactive decay in atoms and proton-proton (pp) fusion  
 377 within the sun. Quarks and leptons are the particles affected by the weak  
 378 interaction; they possess a property called “flavor charge” (see 2.2.1) which can  
 379 be changed by emitting or absorbing one weak force mediator. There are three  
 380 mediators of the “weak force” known as “Z” boson in the case of electrically

<sup>5</sup> particles made of four and five quarks are exotic states not so common.

neutral changes and “ $W^\pm$ ” bosons in the case of electrically charged changes. The “weak isospin” is the WI analog to electric charge in EI, and color charge in SI, and defines how quarks and leptons are affected by the weak force. Figure 2.4c. shows the feynman diagram of  $\beta$ -decay where a newtron (n) is transformed in a proton (p) by emmiting a  $W^-$  particle. Since this thesis is in the frame of the electroweak interaction, a more detailed description of it will be given in section 2.3

- *Gravitational interaction (GI)* described by General Theory of Relativity (GR). It is responsible for the structure of galaxies and black holes as well as the expansion of the universe. As a classical theory, in the sense that it can be formulated without even appeal to the concept of quantization, it implies that the spacetime is a continuum and predictions can be made without limitation to the precision of the measurement tools. The latter represent a direct contradiction of the quantum mechanics principles. Gravity is deterministic while quantum mechanics is probabilistic; despite that, efforts to develop a quantum theory of gravity have predicted the “graviton” as mediator of the Gravitational force<sup>6</sup>.

Interaction	Acts on	Relative strength	Range (m)	Mediators
Electromagnetic (QED)	Electrically charged particles	$10^{-2}$	Infinite	Photon
Strong (QCD)	Quarks and gluons	1	$10^{-15}$	Gluon
Weak (WI)	Leptons and quarks	$10^{-6}$	$10^{-18}$	$W^\pm$ , Z
Gravitational (GI)	Massive particles	$10^{-39}$	Infinite	Graviton

**Table 2.6:** Fundamental interactions features [30].

397

398 Table 2.6 sumarizes the main features of the fundamental interactions. The rela-  
399 tive strength of the fundamental forces reveals the meaning of strong and weak; in

<sup>6</sup> Actually a wide variety of theories have been developed in an attempt to describe gravity; some famous examples are string theory and supergravity.

400 a context where the relative strength of the SI is 1, the EI is about hundred times  
 401 weaker and WI is about million times weaker than the SI. A good description on  
 402 how the relative strength and range of the fundamental interactions are calculated  
 403 can be found in references [30, 31]. In the everyday life, only EI and GI are explicitly  
 404 experienced due to the range of these interactions; i.e., at the human scale distances  
 405 only EI and GI have appreciable effects, in contrast to SI which at distances greater  
 406 than  $10^{-15}$ m become negligible.

407

408 QED was built successfully on the basis of the classical electrodynamics theory (CED)  
 409 of Maxwell and Lorentz, following theoretical and experimental requirements imposed  
 410 by

- 411     • lorentz invariance: independence on the reference frame.
- 412     • locallity: interacting fields are evaluated at the same space-time point to avoid  
     413       action at a distance.
- 414     • renormalizability: physical predictions are finite and well defined
- 415     • particle spectrum, symmetries and conservation laws already known must emerge  
     416       from the theory.
- 417     • gauge invariance.

418 The gauge invariance requirement reflects the fact that the fundamental fields cannot  
 419 be directly measured but associated fields which are the observables. Electric (“**E**”)  
 420 and magnetic (“**B**”) fields in CED are associated with the electric scalar potential  
 421 “**V**” and the vector potential “**A**”. In particular, **E** can be obtained by measuring  
 422 the change in the space of the scalar potential ( $\Delta V$ ); however, two scalar potentials

423 differing by a constant “f” correspond to the same electric field. The same happens in  
 424 the case of the vector potential “ $\mathbf{A}$ ”; thus, different configurations of the associated  
 425 fields result in the same set of values of the observables. The freedom in choosing  
 426 one particular configuration is known as “gauge freedom”; the transformation law con-  
 427 necting two configurations is known as “gauge transformation” and the fact that the  
 428 observables are not affected by a gauge transformation is called “gauge invariance”.

429

430 When the gauge transformation:

$$\begin{aligned} \mathbf{A} &\rightarrow \mathbf{A} - \Delta f \\ V &\rightarrow V - \frac{\partial f}{\partial t} \end{aligned} \tag{2.4}$$

431 is applied to Maxwell equations, they are still satisfied and the fields remain invariant.  
 432 Thus, CED is invariant under gauge transformations and is called a “gauge theory”.  
 433 The set of all gauge transformations form the “symmetry group” of the theory, which  
 434 according to the group theory, has a set of “group generators”. The number of group  
 435 generators determine the number of “gauge fields” of the theory.

436

437 As mentioned in the first lines of section 2.2, QED has one symmetry group ( $U(1)$ )  
 438 with one group generator (the  $Q$  operator) and one gauge field (the electromagnetic  
 439 field  $A^\mu$ ). In CED there is not a clear definition, beyond the historical convention, of  
 440 which fields are the fundamental and which are the associated, but in QED it is clear  
 441 that the fundamental field is  $A^\mu$ . When a gauge theory is quantized, the gauge field  
 442 is quantized and its quanta is called “gauge boson”. The word boson characterizes  
 443 particles with integer spin which obey Bose-Einstein statistics.

444

445 As will be detailed in section 2.3, interactions between particles in a system can be  
 446 obtained by considering first the Lagrangian density of free particles in the system,  
 447 which of course is incomplete because the interaction terms have been left out, and  
 448 demanding global phase transformation invariance. Global phase transformation in-  
 449 variance means that a gauge transformation is performed identically to every point  
 450 in the space<sup>7</sup> and the Lagrangian remains invariant. Then, the global transformation  
 451 is promoted to a local phase transformation (this time the gauge transformation de-  
 452 pends on the position in space) and again invariance is required.

453

454 Due to the space dependence of the local transformation, the Lagrangian density is  
 455 not invariant anymore. In order to restate the gauge invariance, the gauge covariant  
 456 derivative is introduced in the Lagrangian and with it the gauge field responsible for  
 457 the interaction between particles in the system. The new Lagrangian density is gauge  
 458 invariant, includes the interaction terms needed to account for the interactions and  
 459 provides a way to explain the interaction between particles through the exchange of  
 460 the gauge boson.

461 This recipe was used to build QED and the theories that aim to explain the funda-  
 462 mental interactions.

### 463 2.2.3 Gauge Bosons

464 The importance of the gauge bosons comes from the fact that they are the force  
 465 mediators or force carriers. The features of the gauge bosons reflect those of the  
 466 fields they represent and they are extracted from the Lagrangian density used to  
 467 describe the interactions. In section 2.3, it will be shown how the gauge bosons of the

---

<sup>7</sup> Here space corresponds to the 4-dimensional space i.e. space-time.

468 EI and WI emerge from the electroweak Lagrangian. The SI gauge bosons features  
469 are also extracted from the SI Lagrangian but it is not detailed in this document. The  
470 main features of the SM gauge bosons will be briefly presented below and summarized  
471 in table 2.7.

472 • **Photon.** EI occurs when the photon couples to (is exchanged between) particles  
473 carrying electric charge; however, the photon itself does not carry electric charge,  
474 therefore, there is no coupling between photons. Given that the photon is  
475 massless the EI is of infinite range, i.e., electrically charged particles interact  
476 even if they are located far away one from each other; this also implies that  
477 photons always move with the speed of light.

478 • **Gluon.** SI is mediated by gluons which, same as photons, are massless. They  
479 carry one unit of color charge and one unit of anticolor charge which means that  
480 gluons couple to other gluons. As a result, the range of the SI is not infinite  
481 but very short due to the attraction between gluons, giving rise to the “color  
482 confinement” which explains why color charged particles cannot be isolated but  
483 live within composited particles, like quarks inside protons.

484 • **W, Z.** The WI mediators,  $W^\pm$  and Z, are massive which explains their short-  
485 range. Given that the WI is the only interaction that can change the flavor  
486 of the interacting particles, the W boson is the responsible for the nuclear  
487 transmutation where a neutron is converted in a proton or vice versa with the  
488 involvement of an electron and a neutrino (see figure 2.4c). The Z boson is the  
489 responsible of the neutral weak processes like neutrino elastic scattering where  
490 no electric charge but momentum transference is involved. WI gauge bosons  
491 carry isospin charge which makes possible the interaction between them.

Interaction	Mediator	Electric charge (e)	Color charge	Weak Isospin	mass (GeV/c <sup>2</sup> )
Electromagnetic	Photon ( $\gamma$ )	0	No	0	0
Strong	Gluon (g)	0	Yes -octet	No	0
Weak	$W^\pm$	$\pm 1$	No	$\pm 1$	$80.385 \pm 0.015$
	Z	0	No	0	$91.188 \pm 0.002$

**Table 2.7:** SM gauge bosons main features [21].

492

## 493 2.3 Electroweak unification and the Higgs

### 494 mechanism

495 Physicists dream of building a theory that contains all the interactions in one single  
 496 interaction, i.e., showing that at some scale in energy all the four fundamental in-  
 497 teractions are unified and only one interaction emerges in a “Theory of everything”.  
 498 The first sign of the feasibility of such unification comes from success in the con-  
 499 struction of the CED. Einstein spent years trying to reach that dream, which by  
 500 1920 only involved electromagnetism and gravity, with no success; however, a new  
 501 partial unification was achieved in the 1960’s, when S.Glashow [14], A.Salam [15] and  
 502 S.Weinberg [16] independently proposed that electromagnetic and weak interactions  
 503 are two manifestations of a more general interaction called “electroweak interaction  
 504 (EWT)”. Both, QCD and EWT, were developed in parallel and following the useful  
 505 prescription provided by QED and the gauge invariance principles.

506

507 The theory of weak interactions was capable of explaining the  $\beta$ -decay and in general  
 508 the processes mediated by  $W^\pm$  bosons. However, there were some processes like the  
 509 “ $\nu_\mu - e$  scattering” which would require the exchange of two W bosons (see figure 2.5  
 510 top diagrams) giving rise to divergent loop integrals and then non finite predictions.

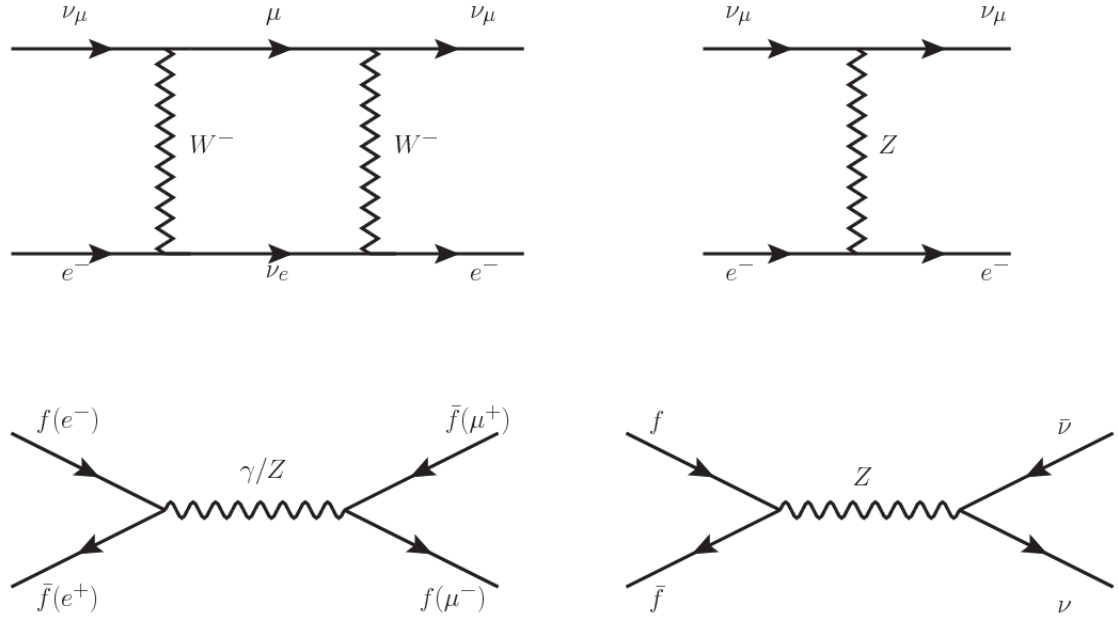


**Figure 2.5:** Top:  $\nu_\mu - e^-$  scattering going through charged currents (left) and neutral currents (right). Bottom: neutral current processes for charged fermions (left) and involving neutrinos (right). While neutral current processes involving only charged fermions can proceed through EI or WI, those involving neutrinos can only proceed via WI.

- 511 By including neutral currents involving fermions via the exchange of neutral bosons
- 512  $Z$ , those divergences are compensated and the predictions become realistic.
- 513
- 514 Neutral weak interaction vertices conserve flavor in the same way as the electromag-
- 515 netic vertices do, but additionally, the  $Z$  boson can couple to neutrinos which implies
- 516 that processes involving charged fermions can proceed through EI or WI but processes
- 517 involving neutrinos can proceed only through WI.
- 518
- 519 The prescription to build a gauge theory of the WI consists of proposing a free field
- 520 Lagrangian density that includes the particles involved; next, by requesting invari-
- 521 ance under global phase transformations first and generalizing to local phase trans-
- 522 formations invariance later, the conserved currents are identified and interactions are

523 generated by introducing gauge fields. Given that the goal is to include the EI and  
 524 WI in a single theory, the group symmetry considered should be a combination of  
 525  $SU(2)_L$  and  $U(1)_{em}$ , however the latter cannot be used directly because the EI treats  
 526 left and right-handed particles indistinctly in contrast to the former. Fortunately, the  
 527 weak hypercharge, which is a combination of the weak isospin and the electric charge  
 528 (eqn 2.2) is suitable to be used since it is conserved by the EI and WI. Thus, the  
 529 symmetry group to be considered is

$$G \equiv SU(2)_L \otimes U(1)_Y \quad (2.5)$$

530 The following treatment applies to any of the fermion generations, but for simplicity  
 531 the first generation of leptons will be considered [2, 3, 32, 33].

532

533 Given the first generation of leptons

$$\psi_1 = \begin{pmatrix} \nu_e \\ e^- \end{pmatrix}_L, \quad \psi_2 = \nu_{eR}, \quad \psi_3 = e_R^- \quad (2.6)$$

534 the charged fermionic currents are given by

$$J_\mu \equiv J_\mu^+ = \bar{\nu}_{eL} \gamma_\mu e_L, \quad J_\mu^\dagger \equiv J_\mu^- = \bar{e}_L \gamma_\mu \nu_{eL} \quad (2.7)$$

535 and the free Lagrangian is given by

$$\mathcal{L}_0 = \sum_{j=1}^3 i\bar{\psi}_j(x) \gamma^\mu \partial_\mu \psi_j(x). \quad (2.8)$$

536 Mass terms are included directly in the QED and QCD free Lagrangians since they  
 537 preserve the invariance under the symmetry transformations involved which treat  
 538 left-handed and right-handed similarly, however mass terms of the form

$$m_W^2 W_\mu^\dagger(x) W^\mu(x) + \frac{1}{2} m_Z^2 Z_\mu(x) Z^\mu(x) - m_e \bar{\psi}_e(x) \psi_e(x) \quad (2.9)$$

539 which represent the mass of  $W^\pm$ , Z and electrons, are not invariant under G trans-  
 540 formations, therefore the gauge fields described by the EWI are in principle massless.

541

542 Experiments have shown that the gauge fields are not massless; however, they have  
 543 to acquire mass through a mechanism compatible with the gauge invariance; that  
 544 mechanism is known as the “Higgs mechanism” and will be considered later in this  
 545 section. The global transformations in the combined symmetry group G can be  
 546 written as

$$\begin{aligned} \psi_1(x) &\xrightarrow{G} \psi'_1(x) \equiv U_Y U_L \psi_1(x), \\ \psi_2(x) &\xrightarrow{G} \psi'_2(x) \equiv U_Y \psi_2(x), \\ \psi_3(x) &\xrightarrow{G} \psi'_3(x) \equiv U_Y \psi_3(x) \end{aligned} \quad (2.10)$$

547 where  $U_L$  represent the  $SU(2)_L$  transformation acting only on the weak isospin dou-  
 548 blet and  $U_Y$  represent the  $U(1)_Y$  transformation acting on all the weak isospin mul-  
 549 tiplets. Explicitly

$$U_L \equiv \exp\left(i \frac{\sigma_i}{2} \alpha^i\right), \quad U_Y \equiv \exp(i y_i \beta) \quad (i = 1, 2, 3) \quad (2.11)$$

550 with  $\sigma_i$  the Pauli matrices and  $y_i$  the weak hypercharges. In order to promote the  
 551 transformations from global to local while keeping the invariance, it is required that  
 552  $\alpha^i = \alpha^i(x)$ ,  $\beta = \beta(x)$  and the replacement of the ordinary derivatives by the covariant  
 553 derivatives

$$\begin{aligned}
D_\mu \psi_1(x) &\equiv \left[ \partial_\mu + ig\sigma_i W_\mu^i(x)/2 + ig'y_1 B_\mu(x) \right] \psi_1(x) \\
D_\mu \psi_2(x) &\equiv \left[ \partial_\mu + ig'y_2 B_\mu(x) \right] \psi_2(x) \\
D_\mu \psi_3(x) &\equiv \left[ \partial_\mu + ig'y_3 B_\mu(x) \right] \psi_3(x)
\end{aligned} \tag{2.12}$$

554 introducing in this way four gauge fields,  $W_\mu^i(x)$  and  $B_\mu(x)$ , in the process. The  
555 covariant derivatives (eqn 2.12) are required to transform in the same way as fermion  
556 fields  $\psi_i(x)$  themselves, therefore, the gauge fields transform as:

$$\begin{aligned}
B_\mu(x) &\xrightarrow{G} B'_\mu(x) \equiv B_\mu(x) - \frac{1}{g'} \partial_\mu \beta(x) \\
W_\mu^i(x) &\xrightarrow{G} W_\mu^{i\prime}(x) \equiv W_\mu^i(x) - \frac{i}{g} \partial_\mu \alpha_i(x) - \varepsilon_{ijk} \alpha_i(x) W_\mu^j(x).
\end{aligned} \tag{2.13}$$

557 The G invariant version of the Lagrangian density 2.8 can be written as

$$\mathcal{L}_0 = \sum_{j=1}^3 i\bar{\psi}_j(x) \gamma^\mu D_\mu \psi_j(x) \tag{2.14}$$

558 where free massless fermion and gauge fields and fermion-gauge boson interactions  
559 are included. The EWI Lagrangian density must additionally include kinetic terms  
560 for the gauge fields ( $\mathcal{L}_G$ ) which are built from the field strengths, according to

$$B_{\mu\nu}(x) \equiv \partial_\mu B_\nu - \partial_\nu B_\mu \tag{2.15}$$

$$W_{\mu\nu}^i(x) \equiv \partial_\mu W_\nu^i(x) - \partial_\nu W_\mu^i(x) - g\varepsilon^{ijk} W_\mu^j W_\nu^k \tag{2.16}$$

561 the last term in eqn. 2.16 is added in order to hold the gauge invariance; therefore,

$$\mathcal{L}_G = -\frac{1}{4}B_{\mu\nu}(x)B^{\mu\nu}(x) - \frac{1}{4}W_{\mu\nu}^i(x)W_i^{\mu\nu}(x) \quad (2.17)$$

562 which contains not only the free gauge fields contributions, but also the gauge fields  
 563 self-interactions and interactions among them.

564

565 The three weak isospin conserved currents resulting from the  $SU(2)_L$  symmetry are  
 566 given by

$$J_\mu^i(x) = \frac{1}{2}\bar{\psi}_1(x)\gamma_\mu\sigma^i\psi_1(x) \quad (2.18)$$

567 while the weak hypercharge conserved current resulting from the  $U(1)_Y$  symmetry is  
 568 given by

$$J_\mu^Y = \sum_{j=1}^3 \bar{\psi}_j(x)\gamma_\mu y_j \psi_j(x) \quad (2.19)$$

569 In order to evaluate the electroweak interactions modeled by an isos triplet field  $W_\mu^i$   
 570 which couples to isospin currents  $J_\mu^i$  with strength  $g$  and additionally the singlet  
 571 field  $B_\mu$  which couples to the weak hypercharge current  $J_\mu^Y$  with strength  $g'/2$ . The  
 572 interaction Lagrangian density to be considered is

$$\mathcal{L}_I = -g J^{i\mu}(x) W_\mu^i(x) - \frac{g'}{2} J^{Y\mu}(x) B_\mu(x) \quad (2.20)$$

573 Note that the weak isospin currents are not the same as the charged fermionic currents  
 574 that were used to describe the WI (eqn 2.7), since the weak isospin eigenstates are  
 575 not the same as the mass eigenstates, but they are closely related

$$J_\mu = \frac{1}{2}(J_\mu^1 + iJ_\mu^2), \quad J_\mu^\dagger = \frac{1}{2}(J_\mu^1 - iJ_\mu^2). \quad (2.21)$$

576 The same happens with the gauge fields  $W_\mu^i$  which are related to the mass eigenstates  
 577  $W^\pm$  by

$$W_\mu^+ = \frac{1}{\sqrt{2}}(W_\mu^1 - iW_\mu^2), \quad W_\mu^- = \frac{1}{\sqrt{2}}(W_\mu^1 + iW_\mu^2). \quad (2.22)$$

578 The fact that there are three weak isospin conserved currents is an indication that in  
 579 addition to the charged fermionic currents, which couple charged to neutral leptons,  
 580 there should be a neutral fermionic current that does not involve electric charge  
 581 exchange; therefore, it couples neutral fermions or fermions of the same electric charge.  
 582 The third weak isospin current contains a term that is similar to the electromagnetic  
 583 current ( $j_\mu^{em}$ ), indicating that there is a relation between them and resembling the  
 584 Gell-Mann-Nishijima formula 2.2 adapted to electroweak interactions

$$Q = T_3 + \frac{Y_W}{2}. \quad (2.23)$$

585 Just as Q generates the  $U(1)_{em}$  symmetry, the weak hypercharge generates the  $U(1)_Y$   
 586 symmetry as said before. It is possible to write the relationship in terms of the currents  
 587 as

$$j_\mu^{em} = J_\mu^3 + \frac{1}{2}J_\mu^Y. \quad (2.24)$$

588 The neutral gauge fields  $W_\mu^3$  and  $B_\mu$  cannot be directly identified with the  $Z$  and the  
 589 photon fields since the photon interacts similarly with left and right-handed fermions;  
 590 however, they are related through a linear combination given by

$$A_\mu = B_\mu \cos \theta_W + W_\mu^3 \sin \theta_W \quad (2.25)$$

$$Z_\mu = -B_\mu \sin \theta_W + W_\mu^3 \cos \theta_W$$

591 where  $\theta_W$  is known as the “Weinberg angle.” The interaction Lagrangian is now given

592 by

$$\mathcal{L}_I = -\frac{g}{\sqrt{2}}(J^\mu W_\mu^+ + J^{\mu\dagger} W_\mu^-) - \left(g \sin \theta_W J_\mu^3 + g' \cos \theta_W \frac{J_\mu^Y}{2}\right) A^\mu - \left(g \cos \theta_W J_\mu^3 - g' \sin \theta_W \frac{J_\mu^Y}{2}\right) Z^\mu \quad (2.26)$$

593 the first term is the weak charged current interaction, while the second term is the

594 electromagnetic interaction under the condition

$$g \sin \theta_W = g' \cos \theta_W = e, \quad \frac{g'}{g} = \tan \theta_W \quad (2.27)$$

595 contained in the eqn.2.24; the third term is the neutral weak current.

596

597 Note that the neutral fields transformation given by the eqn. 2.25 can be written in

598 terms of the coupling constants  $g$  and  $g'$  as:

$$A_\mu = \frac{g' W_\mu^3 + g B_\mu}{\sqrt{g^2 + g'^2}}, \quad Z_\mu = \frac{g W_\mu^3 - g' B_\mu}{\sqrt{g^2 + g'^2}} \quad (2.28)$$

599 So far, the Lagrangian density describing the non-massive EWI is:

$$\mathcal{L}_{nmEWI} = \mathcal{L}_0 + \mathcal{L}_G \quad (2.29)$$

600 where fermion and gauge fields have been considered massless because their regular

601 mass terms are manifestly non invariant under G transformations; therefore, masses

602 have to be generated in a gauge invariant way. The mechanism by which this goal is  
 603 achieved is known as the “Higgs mechanism” and is closely connected to the concept  
 604 of “spontaneous symmetry breaking.”

### 605 2.3.1 Spontaneous symmetry breaking (SSB)

606 Figure 2.6 left shows a steel nail (top) which is subject to an external force; the form  
 607 of the potential energy is also shown (bottom).

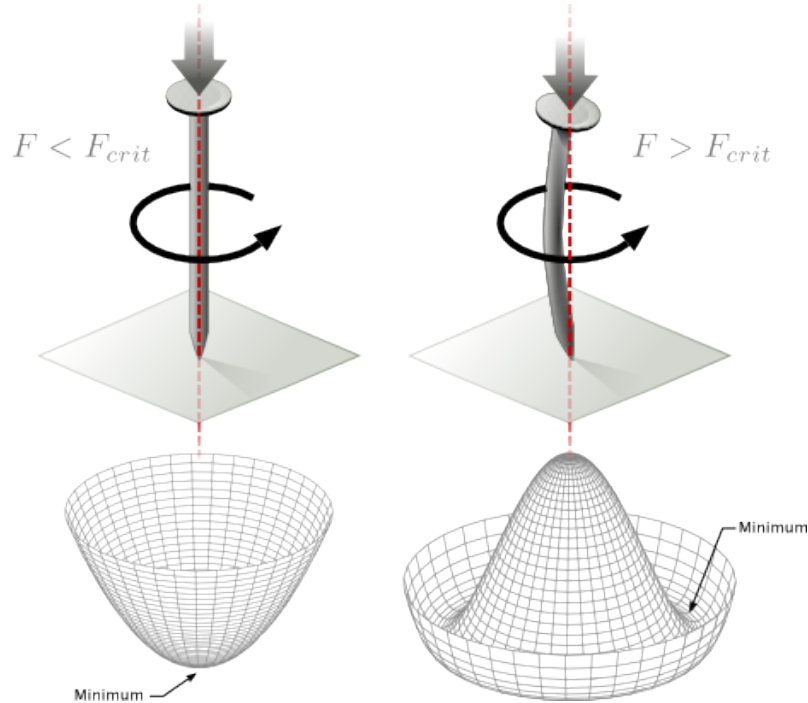


**Figure 2.6:** Spontaneous symmetry breaking mechanism. The steel nail, subject to an external force (top left), has rotational symmetry with respect to its axis. When the external force overcomes a critical value the nail buckles (top right) choosing a minimal energy state (ground state) and thus “*breaking spontaneously the rotational symmetry*”. The potential energy (bottom) changes but holds the rotational symmetry; however, an infinite number of asymmetric ground states are generated and circularly distributed in the bottom of the potential [34].

609 Before reaching the critical force value, the system has rotational symmetry with re-  
 610 spect to the nail axis; however, after the critical force value is reached the nail buckles  
 611 (top right). The form of the potential energy (bottom right) changes, preserving its  
 612 rotational symmetry although its minima does not exhibit that rotational symmetry  
 613 any longer. Right before the nail buckles there is no indication of the direction the  
 614 nail will bend because any of the directions are equivalent, but once the nail bends,  
 615 choosing a direction, an arbitrary minimal energy state (ground state) is selected and  
 616 it does not share the system's rotational symmetry. This mechanism for reaching an  
 617 asymmetric ground state is known as "*spontaneous symmetry breaking*".  
 618 The lesson from this analysis is that the way to introduce the SSB mechanism into a  
 619 system is by adding the appropriate potential to it.

620

621 Figure 2.7 shows a plot of the potential  $V(\phi)$  in the case of a scalar field  $\phi$

$$V(\phi) = \mu^2 \phi^\dagger \phi + \lambda (\phi^\dagger \phi)^2 \quad (2.30)$$

622 If  $\mu^2 > 0$  the potential has only one minimum at  $\phi = 0$  and describes a scalar field  
 623 with mass  $\mu$ . If  $\mu^2 < 0$  the potential has a local maximum at  $\phi = 0$  and two minima  
 624 at  $\phi = \pm\sqrt{-\mu^2/\lambda}$  which enables the SSB mechanism to work.

625

626 In the case of a complex scalar field  $\phi(x)$

$$\phi(x) = \frac{1}{\sqrt{2}}(\phi_1 + i\phi_2) \quad (2.31)$$

627 the Lagrangian (invariant under global  $U(1)$  transformations) is given by

$$\mathcal{L} = (\partial_\mu \phi)^\dagger (\partial^\mu \phi) - V(\phi), \quad V(\phi) = \mu^2 \phi^\dagger \phi + \lambda (\phi^\dagger \phi)^2 \quad (2.32)$$

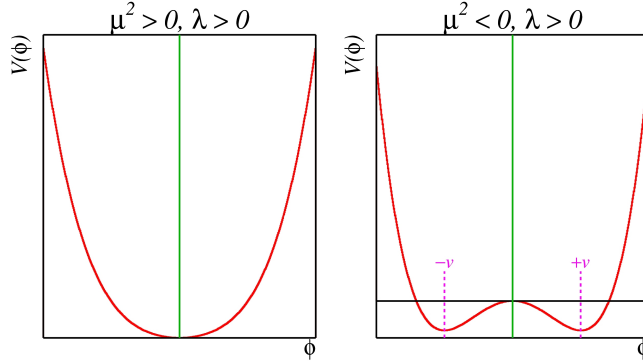


**Figure 2.7:** Shape of the potential  $V(\phi)$  for  $\lambda > 0$  and:  $\mu^2 > 0$  (left) and  $\mu^2 < 0$  (right). The case  $\mu^2 < 0$  corresponds to the potential suitable for introducing the SSB mechanism by choosing one of the two ground states which are connected via reflection symmetry. [34].

628 where an appropriate potential has been added in order to introduce the SSB.

629

630 As seen in figure 2.8, the potential has now an infinite number of minima circularly  
 631 distributed along the  $\xi$ -direction which makes possible the occurrence of the SSB by  
 632 choosing an arbitrary ground state; for instance,  $\xi = 0$ , i.e.  $\phi_1 = v, \phi_2 = 0$

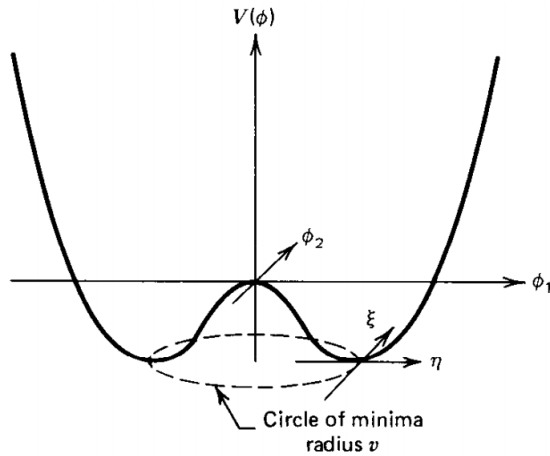


**Figure 2.8:** Potential for complex scalar field. There is a circle of minima of radius  $v$  along the  $\xi$ -direction [3].

$$\phi_0 = \frac{v}{\sqrt{2}} \exp(i\xi) \xrightarrow{\text{SSB}} \phi_0 = \frac{v}{\sqrt{2}} \quad (2.33)$$

633 As usual, excitations over the ground state are studied by making an expansion about  
 634 it; thus, the excitation can be parametrized as:

$$\phi(x) = \frac{1}{\sqrt{2}}(v + \eta(x) + i\xi(x)) \quad (2.34)$$

635 which when substituted into eqn. 2.32 produces a Lagrangian in terms of the new  
 636 fields  $\eta$  and  $\xi$

$$\mathcal{L}' = \frac{1}{2}(\partial_\mu \xi)^2 + \frac{1}{2}(\partial_\mu \eta)^2 + \mu^2 \eta^2 - V(\phi_0) - \lambda v \eta (\eta^2 + \xi^2) - \frac{\lambda}{4}(\eta^2 + \xi^2)^2 \quad (2.35)$$

637 where the last two terms represent the interactions and self-interaction between the  
 638 two fields  $\eta$  and  $\xi$ . The particular feature of the SSB mechanism is revealed when  
 639 looking to the first three terms of  $\mathcal{L}'$ . Before the SSB, only the massless  $\phi$  field is  
 640 present in the system; after the SSB there are two fields of which the  $\eta$ -field has  
 641 acquired mass  $m_\eta = \sqrt{-2\mu^2}$  while the  $\xi$ -field is still massless (see figure 2.9).

642

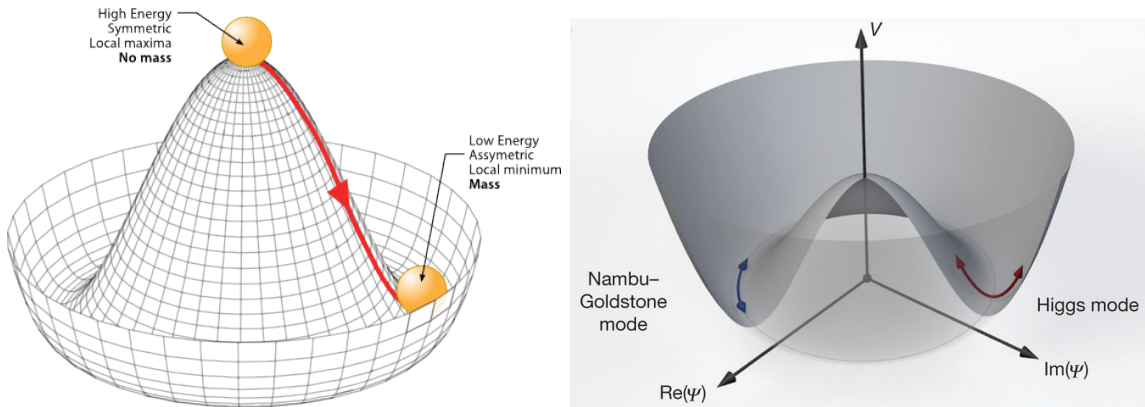


**Figure 2.9:** SSB mechanism for a complex scalar field [34, 35].

643 Thus, the SSB mechanism serves as a method to generate mass but as a side effect a

644 massless field is introduced in the system. This fact is known as the Goldstone theorem  
 645 and states that a massless scalar field appears in the system for each continuous  
 646 symmetry spontaneously broken. Another version of the Goldstone theorem states  
 647 that “*if a Lagrangian is invariant under a continuous symmetry group  $G$ , but the*  
 648 *vacuum is only invariant under a subgroup  $H \subset G$ , then there must exist as many*  
 649 *massless spin-0 particles (Nambu-Goldstone bosons) as broken generators.*” [33] The  
 650 Nambu-Goldstone boson can be understood considering that the potential in the  $\xi$ -  
 651 direction is flat so excitations in that direction are not energy consuming and thus  
 652 represent a massless state.

### 653 2.3.2 Higgs mechanism

654 When the SSB mechanism is introduced in the formulation of the EWI in an attempt  
 655 to generate the mass of the so far massless gauge bosons and fermions, an interesting  
 656 effect is revealed. In order to keep the  $G$  symmetry group invariance and generate  
 657 the mass of the EW gauge bosons, a  $G$  invariant Lagrangian density ( $\mathcal{L}_S$ ) has to be  
 658 added to the non massive EWI Lagrangian (eqn. 2.29)

$$\mathcal{L}_S = (D_\mu \phi)^\dagger (D^\mu \phi) - \mu^2 \phi^\dagger \phi - \lambda (\phi^\dagger \phi)^2, \quad \lambda > 0, \mu^2 < 0 \quad (2.36)$$

$$D_\mu \phi = \left( i\partial_\mu - g \frac{\sigma_i}{2} W_\mu^i - g' \frac{Y}{2} B_\mu \right) \phi \quad (2.37)$$

659  $\phi$  has to be an isospin doublet of complex scalar fields so it preserves the  $G$  invariance;  
 660 thus  $\phi$  can be defined as:

$$\phi = \begin{pmatrix} \phi^+ \\ \phi^0 \end{pmatrix} \equiv \frac{1}{\sqrt{2}} \begin{pmatrix} \phi_1 + i\phi_2 \\ \phi_3 + i\phi_4 \end{pmatrix}. \quad (2.38)$$

661 The minima of the potential are defined by

$$\phi^\dagger \phi = \frac{1}{2}(\phi_1^2 + \phi_2^2 + \phi_3^2 + \phi_4^2) = -\frac{\mu^2}{2\lambda}. \quad (2.39)$$

662 The choice of the ground state is critical. By choosing a ground state, invariant under  
 663  $U(1)_{em}$  gauge symmetry, the photon will remain massless and the  $W^\pm$  and  $Z$  bosons  
 664 masses will be generated which is exactly what is needed. In that sense, the best  
 665 choice corresponds to a weak isospin doublet with  $T_3 = -1/2$ ,  $Y_W = 1$  and  $Q = 0$   
 666 which defines a ground state with  $\phi_1 = \phi_2 = \phi_4$  and  $\phi_3 = v$ :

$$\phi_0 \equiv \frac{1}{\sqrt{2}} \begin{pmatrix} 0 \\ v \end{pmatrix}, \quad v^2 \equiv -\frac{\mu^2}{\lambda}. \quad (2.40)$$

667 where the vacuum expectation value  $v$  is fixed by the Fermi coupling  $G_F$  according  
 668 to  $v = (\sqrt{2}G_F)^{1/2} \approx 246$  GeV.

669

670 The G symmetry has been broken and three Nambu-Goldstone bosons will appear.

671 The next step is to expand  $\phi$  about the chosen ground state as:

$$\phi(x) = \frac{1}{\sqrt{2}} \exp\left(\frac{i}{v} \sigma_i \theta^i(x)\right) \begin{pmatrix} 0 \\ v + H(x) \end{pmatrix} \approx \frac{1}{\sqrt{2}} \begin{pmatrix} \theta_1(x) + i\theta_2(x) \\ v + H(x) - i\theta_3(x) \end{pmatrix} \quad (2.41)$$

672 to describe fluctuations from the ground state  $\phi_0$ . The fields  $\theta_i(x)$  represent the  
 673 Nambu-Goldstone bosons while  $H(x)$  is known as “higgs field.” The fundamental  
 674 feature of the parametrization used is that the dependence on the  $\theta_i(x)$  fields is  
 675 factored out in a global phase that can be eliminated by taking the physical “unitary  
 676 gauge”  $\theta_i(x) = 0$ . Therefore the expansion about the ground state is given by:

$$\phi(x) \frac{1}{\sqrt{2}} \begin{pmatrix} 0 \\ v + H(x) \end{pmatrix} \quad (2.42)$$

677 which when substituted into  $\mathcal{L}_S$  (eqn. 2.36) results in a Lagrangian containing the now  
 678 massive three gauge bosons  $W^\pm, Z$ , one massless gauge boson (photon) and the new  
 679 Higgs field ( $H$ ). The three degrees of freedom corresponding to the Nambu-Goldstone  
 680 bosons are now integrated into the massive gauge bosons as their longitudinal po-  
 681 larizations which were not available when they were massless particles. The effect  
 682 by which vector boson fields acquire mass after an spontaneous symmetry breaking,  
 683 but without an explicit gauge invariance breaking is known as the “*Higgs mechanism*”.

684

685 The mechanism was proposed by three independent groups: F.Englert and R.Brout  
 686 in August 1964 [36], P.Higgs in October 1964 [37] and G.Guralnik, C.Hagen and  
 687 T.Kibble in November 1964 [38]; however, its importance was not realized until  
 688 S.Glashow [14], A.Salam [15] and S.Weinberg [16], independently, proposed that elec-  
 689 tromagnetic and weak interactions are two manifestations of a more general interac-  
 690 tion called “electroweak interaction” in 1967.

### 691 2.3.3 Masses of the gauge bosons

692 The mass of the gauge bosons is extracted by evaluating the kinetic part of Lagrangian  
 693  $\mathcal{L}_S$  in the ground state (known also as the vacuum expectation value), i.e.,

$$\left| \left( \partial_\mu - ig \frac{\sigma_i}{2} W_\mu^i - i \frac{g'}{2} B_\mu \right) \phi_0 \right|^2 = \left( \frac{1}{2} v g \right)^2 W_\mu^+ W^{-\mu} + \frac{1}{8} v^2 (W_\mu^3, B_\mu) \begin{pmatrix} g^2 & -gg' \\ -gg' & g'^2 \end{pmatrix} \begin{pmatrix} W^{3\mu} \\ B^\mu \end{pmatrix} \quad (2.43)$$

694 comparing with the typical mass term for a charged boson  $M_W^2 W^+ W^-$

$$M_W = \frac{1}{2} v g. \quad (2.44)$$

The second term in the right side of the eqn.2.43 comprises the masses of the neutral

bosons, but it needs to be written in terms of the gauge fields  $Z_\mu$  and  $A_\mu$  in order to be compared to the typical mass terms for neutral bosons, therefore using eqn. 2.28

$$\begin{aligned} \frac{1}{8}v^2[g^2(W_\mu^3)^2 - 2gg'W_\mu^3B^\mu + g'^2B_\mu^2] &= \frac{1}{8}v^2[gW_\mu^3 - g'B_\mu]^2 + 0[g'W_\mu^3 + gB_\mu]^2 \\ &= \frac{1}{8}v^2[\sqrt{g^2 + g'^2}Z_\mu]^2 + 0[\sqrt{g^2 + g'^2}A_\mu]^2 \end{aligned} \quad (2.45)$$

695 and then

$$M_Z = \frac{1}{2}v\sqrt{g^2 + g'^2}, \quad M_A = 0 \quad (2.46)$$

### 696 2.3.4 Masses of the fermions

697 The lepton mass terms can be generated by introducing a gauge invariant Lagrangian  
698 term describing the Yukawa coupling between the lepton field and the Higgs field

$$\mathcal{L}_{Yl} = -G_l \left[ (\bar{\nu}_l, \bar{l})_L \begin{pmatrix} \phi^+ \\ \phi^0 \end{pmatrix} l_R + \bar{l}_R (\phi^-, \bar{\phi}^0) \begin{pmatrix} \nu_l \\ l \end{pmatrix}_L \right], \quad l = e, \mu, \tau. \quad (2.47)$$

699 After the SSB and replacing the usual field expansion about the ground state (eqn.2.40)  
700 into  $\mathcal{L}_{Yl}$ , the mass term arises

$$\mathcal{L}_{Yl} = -m_l(\bar{l}_L l_R + \bar{l}_R l_L) - \frac{m_l}{v}(\bar{l}_L l_R + \bar{l}_R l_L)H = -m_l \bar{l} \left( 1 + \frac{H}{v} \right) \quad (2.48)$$

701

$$m_l = \frac{G_l}{\sqrt{2}}v \quad (2.49)$$

702 where the additional term represents the lepton-Higgs interaction. The quark masses  
703 are generated in a similar way as lepton masses but for the upper member of the

704 quark doublet a different Higgs doublet is needed:

$$\phi_c = -i\sigma_2\phi^* = \begin{pmatrix} -\bar{\phi}^0 \\ \phi^- \end{pmatrix}. \quad (2.50)$$

705 Additionally, given that the quark isospin doublets are not constructed in terms of  
 706 the mass eigenstates but in terms of the flavor eigenstates, as shown in table 2.5, the  
 707 coupling parameters will be related to the CKM matrix elements; thus the quark  
 708 Lagrangian is given by:

$$\mathcal{L}_{Yq} = -G_d^{i,j}(\bar{u}_i, \bar{d}_i)_L \begin{pmatrix} \phi^+ \\ \phi^0 \end{pmatrix} d_{jR} - G_u^{i,j}(\bar{u}_i, \bar{d}_i)_L \begin{pmatrix} -\bar{\phi}^0 \\ \phi^- \end{pmatrix} u_{jR} + h.c. \quad (2.51)$$

709 with  $i,j=1,2,3$ . After SSB and expansion about the ground state, the diagonal form  
 710 of  $\mathcal{L}_{Yq}$  is:

$$\mathcal{L}_{Yq} = -m_d^i \bar{d}_i d_i \left( 1 + \frac{H}{v} \right) - m_u^i \bar{u}_i u_i \left( 1 + \frac{H}{v} \right) \quad (2.52)$$

711 Fermion masses depend on arbitrary couplings  $G_l$  and  $G_{u,d}$  and are not predicted by  
 712 the theory.

### 713 2.3.5 The Higgs field

714 After the characterization of the fermions and gauge bosons as well as their interac-  
 715 tions, it is necessary to characterize the Higgs field itself. The Lagrangian  $\mathcal{L}_S$  in eqn.  
 716 2.3.6 written in terms of the gauge bosons is given by

$$\mathcal{L}_S = \frac{1}{4}\lambda v^4 + \mathcal{L}_H + \mathcal{L}_{HV} \quad (2.53)$$

717

$$\mathcal{L}_H = \frac{1}{2}\partial_\mu H \partial^\mu H - \frac{1}{2}m_H^2 H^2 - \frac{1}{2v}m_H^2 H^3 - \frac{1}{8v^2}m_H^2 H^4 \quad (2.54)$$

718

$$\mathcal{L}_{HV} = m_H^2 W_\mu^+ W^{\mu-} \left( 1 + \frac{2}{v}H + \frac{2}{v^2}H^2 \right) + \frac{1}{2}m_Z^2 Z_\mu Z^\mu \left( 1 + \frac{2}{v}H + \frac{2}{v^2}H^2 \right) \quad (2.55)$$

719 The mass of the Higgs boson is deduced as usual from the mass term in the Lagrangian  
 720 resulting in:

$$m_H = \sqrt{-2\mu^2} = \sqrt{2\lambda}v \quad (2.56)$$

721 however, it is not predicted by the theory either. The experimental efforts to find  
 722 the Higgs boson, carried out by the “Compact Muon Solenoid (CMS)” experiment  
 723 and the “A Toroidal LHC AppartuS (ATLAS)” experiments at the “Large Hadron  
 724 Collider(LHC)”, gave great results by July of 2012 when the discovery of a new  
 725 particle compatible with the Higgs boson predicted by the electroweak theory [39, 40]  
 726 was announced. Although at the announcement time there were some reservations  
 727 about calling the new particle the “Higgs boson”, today this name is widely accepted.  
 728 The Higgs mass measurement, reported by both experiments [41], is in table 2.8.

Property	Value
Electric charge	0
Colour charge	0
Spin	0
Weak isospin	-1/2
Weak hypercharge	1
Parity	1
Mass (GeV/c <sup>2</sup> )	125.09±0.21 (stat.)±0.11 (syst.)

**Table 2.8:** Higgs boson properties. Higgs mass is not predicted by the theory and the value here corresponds to the experimental measurement.

729

### 730 2.3.6 Higgs boson production mechanisms at LHC.

731 At LHC, Higgs boson is produced as a result of the collision of two counter-rotating  
 732 protons beams. A detailed description of the LHC machine will be presented in  
 733 chapter 3. “The total cross section” is a parameter that quantifies the number of pp  
 734 collisions that happen when a number of protons are fired at each other. Different  
 735 results can be obtained after a pp collision and for each one the “cross section” is

defined as the number of pp collisions that conclude in that particular result with respect to the number of protons fired at each other.

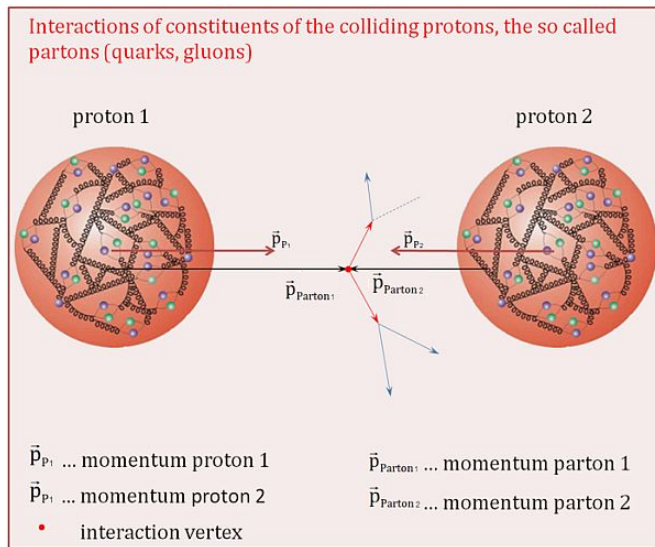


**Figure 2.10:** Proton-proton collision. Protons are composed of 3 valence quarks, a sea of quarks and gluons; therefore in a proton-proton collision, quarks and gluons are those who collide. [45].

737

738 Protons are composed of quarks and these quarks are bound by gluons; however,  
739 what is commonly called the quark content of the proton makes reference to the  
740 valence quarks. A sea of quarks and gluons is also present inside the proton as repre-  
741 sented in figure 2.10. In a proton-proton (pp) collision, the constituents (quarks and  
742 gluons) are those who collide. The pp cross section depends on the momentum of  
743 the colliding particles, reason for which it is needed to know how the momentum is  
744 distributed inside the proton. Quarks and gluons are known as partons and the func-  
745 tions that describe how the proton momentum is distributed among partons inside it  
746 are called “parton distribution functions (PDFs)”; PDFs are determined from experi-  
747 mental data obtained in experiments where the internal structure of hadrons is tested.

748

<sup>749</sup> In addition, in physics, a common approach to study complex systems consists in

750 starting with a simpler version of them, for which a well known description is avail-  
 751 able, and add an additional “perturbation” which represents a small deviation from  
 752 the known behavior. If the perturbation is small enough, the physical quantities as-  
 753 sociated with the perturbed system are expressed as a series of corrections to those  
 754 of the simpler system; therefore, the more terms are considered in the series (the  
 755 higher order in the perturbation series), the more precise is the the description of the  
 756 complex system.

757

758 This thesis explores the Higgs production at LHC; therefore the overview presented  
 759 here will be oriented specifically to the production mechanisms after pp collisions at  
 760 LHC.

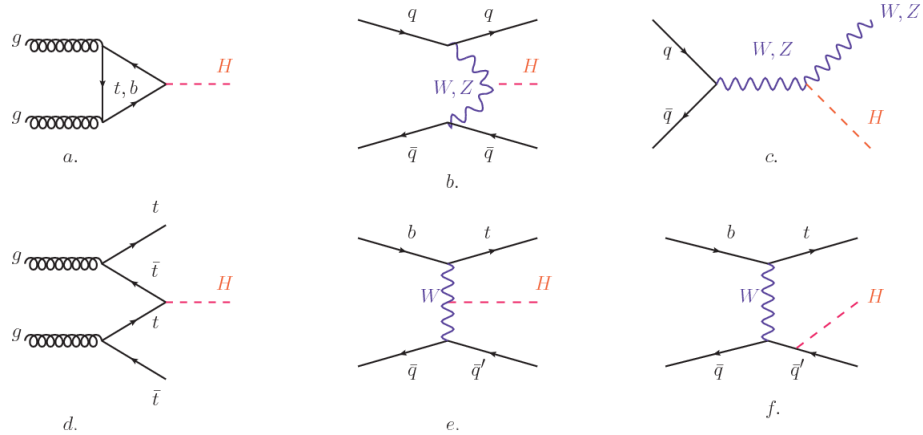


**Figure 2.11:** Main Higgs production mechanism Feynman diagrams. a. gluon-gluon fusion, b. vector boson fusion (VBF), c. Higgs-strahlung, d. Associated production with a top or bottom quark pair, e-f. associated production with a single top quark.

761 Figure 2.11 shows the Feynman diagrams for the leading order (first order) Higgs  
 762 production processes at LHC, while the cross section for Higgs production as a func-  
 763 tion of the center of mass-energy ( $\sqrt{s}$ ) for pp collisions is showed in figure 2.12 left.  
 764 The tags NLO (next to leading order), NNLO (next to next to leading order) and  
 765 N3LO (next to next to next to leading order) make reference to the order at which

766 the perturbation series have been considered.

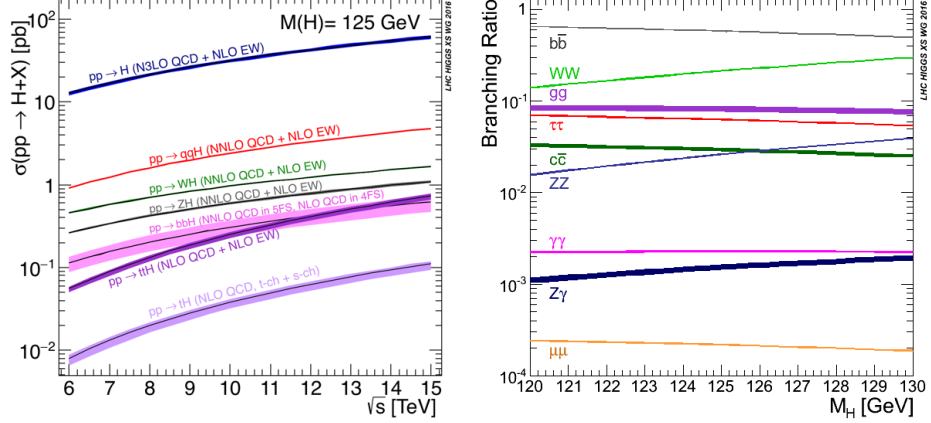


**Figure 2.12:** Higgs production cross sections (left) and decay branching ratios (right) for the main mechanisms. The VBF is indicated as  $q\bar{q}H$  [42].

767 As shown in eqns 2.47, 2.51 and 2.55, the strength of the Higgs-fermion interaction  
 768 is proportional to the fermion mass while the strength of the Higgs-gauge boson  
 769 interaction is proportional to the square of the gauge boson mass, which implies  
 770 that the Higgs production and decay mechanisms are dominated by couplings  $H -$   
 771  $(W, Z, t, b, \tau)$ .

772 The main production mechanism is the gluon fusion (figure 2.11a and  $pp \rightarrow H$  in figure  
 773 2.12) given that gluons carry the highest fraction of momentum of the protons in pp  
 774 colliders. Since the Higgs boson does not couple to gluons, the mechanism proceeds  
 775 through the exchange of a virtual top-quark loop given that for it the coupling is  
 776 the biggest. Note that in this process, the Higgs boson is produced alone, which  
 777 makes this mechanism experimentally clean when combined with the two-photon or  
 778 the four-lepton decay channels (see section 2.3.7).

779 Vector boson fusion (figure 2.11b and  $pp \rightarrow q\bar{q}H$  in figure 2.12) has the second largest  
 780 production cross section. The scattering of two fermions is mediated by a weak  
 781 gauge boson which later emits a Higgs boson. In the final state, the two fermions

782 tend to be located in a particular region of the detector which is used as a signature  
 783 when analyzing the datasets provided by the experiments. More details about how  
 784 to identify events of interest in an analysis will be given in chapter 4.

785 The next production mechanism is Higgs-strahlung (figure 2.11c and  $pp \rightarrow WH, pp \rightarrow$   
 786  $ZH$  in figure 2.12) where two fermions annihilate to form a weak gauge boson. If the  
 787 initial fermions have enough energy, the emergent boson eventually will emit a Higgs  
 788 boson.

789 The associated production with a top or bottom quark pair and the associated pro-  
 790 duction with a single top quark (figure 2.11d-f and  $pp \rightarrow bbH, pp \rightarrow t\bar{t}H, pp \rightarrow tH$   
 791 in figure 2.12) have a smaller cross section than the main three mechanisms above,  
 792 but they provide a good opportunity to test the Higgs-top coupling. The analysis  
 793 reported in this thesis is developed using these production mechanisms. A detailed  
 794 description of the  $tH$  mechanism will be given in section 2.4.

### 795 2.3.7 Higgs decay channels

796 When a particle can decay through several modes, also known as channels, the  
 797 probability of decaying through a given channel is quantified by the “branching ratio  
 798 (BR)” of the decay channel; thus, the BR is defined as the ratio of number of decays  
 799 going through that given channel to the total number of decays. In regard to the  
 800 Higgs boson decay, the BR can be predicted with accuracy once the Higgs mass is  
 801 known [43, 44]. In figure 2.12 right, a plot of the BR as a function of the Higgs mass  
 802 is presented. The largest predicted BR corresponds to the  $b\bar{b}$  pair decay channel (see  
 803 table 2.9).

Decay channel	Branching ratio	Rel. uncertainty
$H \rightarrow b\bar{b}$	$5.84 \times 10^{-1}$	$+3.2\% - 3.3\%$
$H \rightarrow W^+W^-$	$2.14 \times 10^{-1}$	$+4.3\% - 4.2\%$
$H \rightarrow \tau^+\tau^-$	$6.27 \times 10^{-2}$	$+5.7\% - 5.7\%$
$H \rightarrow ZZ$	$2.62 \times 10^{-2}$	$+4.3\% - 4.1\%$
$H \rightarrow \gamma\gamma$	$2.27 \times 10^{-3}$	$+5.0\% - 4.9\%$
$H \rightarrow Z\gamma$	$1.53 \times 10^{-3}$	$+9.0\% - 8.9\%$
$H \rightarrow \mu^+\mu^-$	$2.18 \times 10^{-4}$	$+6.0\% - 5.9\%$

**Table 2.9:** Predicted branching ratios and the relative uncertainty for a SM Higgs boson with  $m_H = 125\text{GeV}/c^2$ . [21]

Associated production of Higgs boson has been extensively studied [46–50]. While measurements of the main Higgs production mechanisms rates are sensitive to the strength of the Higgs coupling to W boson or top quark, they are not sensitive to the relative sign between the two couplings. In this thesis, the Higgs boson production mechanism explored is the associated production with a single top quark ( $t\bar{h}$ ) which offers sensitiveness to the relative sign of the Higgs couplings to W boson and to top quark. The description given here is based on the reference [48]

814

815 A process where two incoming particles interact and produce a final state with two  
816 particles can proceed in three ways also called channels (see, for instance, figure 2.13  
817 omitting the red line). The t-channel represents processes where an intermediate  
818 particle is emitted by one of the incoming particles and absorbed by the other. The  
819 s-channel represents processes where the two incoming particles merge into an inter-  
820 mediate particle which eventually will split into the particles in the final state. The  
821 third channel, u-channel, is similar to the t-channel but the two outgoing particles

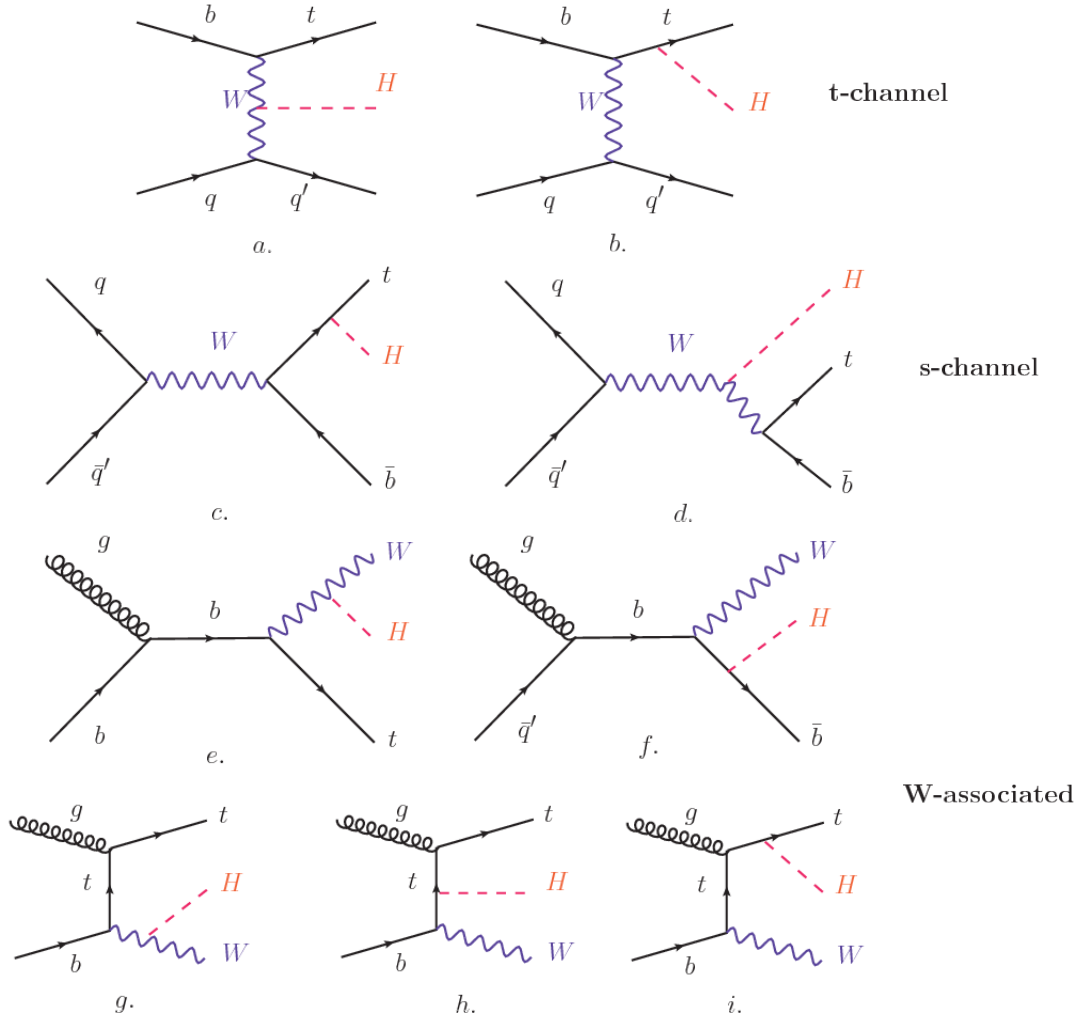


**Figure 2.13:** Associated higgs production mechanism Feynman diagrams. a.,b. t-channel ( $tHq$ ), c.,d. s-channel ( $tHb$ ), e.-i. W-associated.

822 interchange their roles.

823

824 The  $th$  production, where Higgs boson can be radiated either from the top quark or  
 825 from the  $W$  boson, is represented by the leading order Feynman diagrams in figure  
 826 2.13. The cross section for the  $th$  process is calculated, as usual, summing over  
 827 the contributions from the different feynman diagrams; therefore it depends on the  
 828 interference between the contributions. In the SM, the interference for t-channel ( $tHq$

process) and W-associated ( $tHW$  process) production is destructive [46] resulting in the small cross sections presented in table 2.10.

tH production channel	Cross section (fb)
t-channel ( $pp \rightarrow tHq$ )	$70.79^{+2.99}_{-4.80}$
W-associated ( $pp \rightarrow tHW$ )	$15.61^{+0.83}_{-1.04}$
s-channel( $pp \rightarrow tHb$ )	$2.87^{+0.09}_{-0.08}$

**Table 2.10:** Predicted SM cross sections for  $tH$  production at  $\sqrt{s} = 13$  TeV [51, 52].

831

832 While the s-channel contribution can be neglected, it will be shown that a deviation  
 833 from the SM destructive interference would result in an enhancement of the  $th$  cross  
 834 section compared to that in SM, which could be used to get information about the  
 835 sign of the Higgs-top coupling [48, 49]. In order to describe  $th$  production processes,  
 836 Feynman diagram 2.13b will be considered; there, the W boson is radiated by a  
 837 quark in the proton and eventually it will interact with the b quark. In the high  
 838 energy regime, the effective W approximation [53] allows to describe the process as  
 839 the emmision of an approximately on-shell W and its hard scattering with the b  
 840 quark; i.e.  $Wb \rightarrow th$ . The scattering amplitude for the process is given by

$$\mathcal{A} = \frac{g}{\sqrt{2}} \left[ (\kappa_t - \kappa_V) \frac{m_t \sqrt{s}}{m_W v} A \left( \frac{t}{s}, \varphi; \xi_t, \xi_b \right) + \left( \kappa_V \frac{2m_W s}{v} \frac{1}{t} + (2\kappa_t - \kappa_V) \frac{m_t^2}{m_W v} \right) B \left( \frac{t}{s}, \varphi; \xi_t, \xi_b \right) \right], \quad (2.57)$$

841 where  $\kappa_V \equiv g_{HVV}/g_{HVV}^{SM}$  and  $\kappa_t \equiv g_{Ht}/g_{Ht}^{SM} = y_t/y_t^{SM}$  are scaling factors that quan-  
 842 tify possible deviations of the couplings, Higgs-Vector boson (H-W) and Higgs-top  
 843 (H-t) respectively, from the SM couplings;  $s = (p_W + p_b)^2$ ,  $t = (p_W - p_H)^2$ ,  $\varphi$  is the  
 844 Higgs azimuthal angle around the  $z$  axis taken parallel to the direction of motion of  
 845 the incoming W; A and B are funtions describing the weak interaction in terms of

846 the chiral states of the quarks b and t. Terms that vanish in the high energy limit  
 847 have been neglected as well as the Higgs and  $b$  quark masses<sup>8</sup>.

848

849 The scattering amplitude grows with energy like  $\sqrt{s}$  for  $\kappa_V \neq \kappa_t$ , in contrast to  
 850 the SM ( $\kappa_t = \kappa_V = 1$ ), where the first term in 2.57 cancels out and the amplitude  
 851 is constant for large s; therefore, a deviation from the SM predictions represents an  
 852 enhancement in the  $tHq$  cross section. In particular, for a SM H-W coupling and a H-t  
 853 coupling of inverted sign with respect to the SM ( $\kappa_V = -\kappa_t = 1$ ) the  $tHq$  cross section  
 854 is enhanced by a factor greater 10 as seen in the figure 2.14 taken from reference [48];  
 855 reference [54] has reported similar enhancement results.

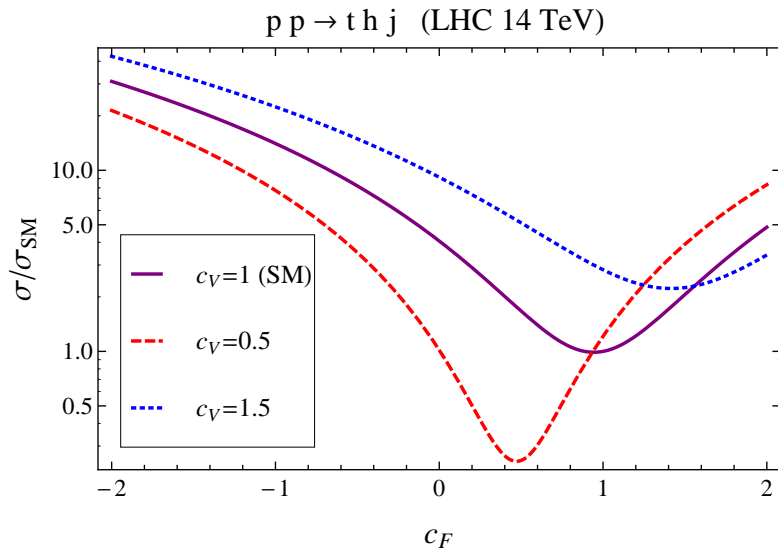


**Figure 2.14:** Cross section for  $tHq$  process as a function of  $\kappa_t$ , normalized to the SM, for three values of  $\kappa_V$ . In the plot  $c_f$  refers to the Higgs-fermion coupling which is dominated by the H-t coupling and represented here by  $\kappa_t$ . Solid, dashed and dotted lines correspond to  $c_V \rightarrow \kappa_V = 1, 0.5, 1.5$  respectively. Note that for the SM ( $\kappa_V = \kappa_t = 1$ ), the destructive effect of the interference is maximal.

856 A similar analysis is valid for the W-associated channel but, in that case, the inter-  
 857 ference is more complicated since there are more than two contributions and an ad-

---

<sup>8</sup> A detailed explanation of the structure and approximations used to derive  $\mathcal{A}$  can be found in reference [48]

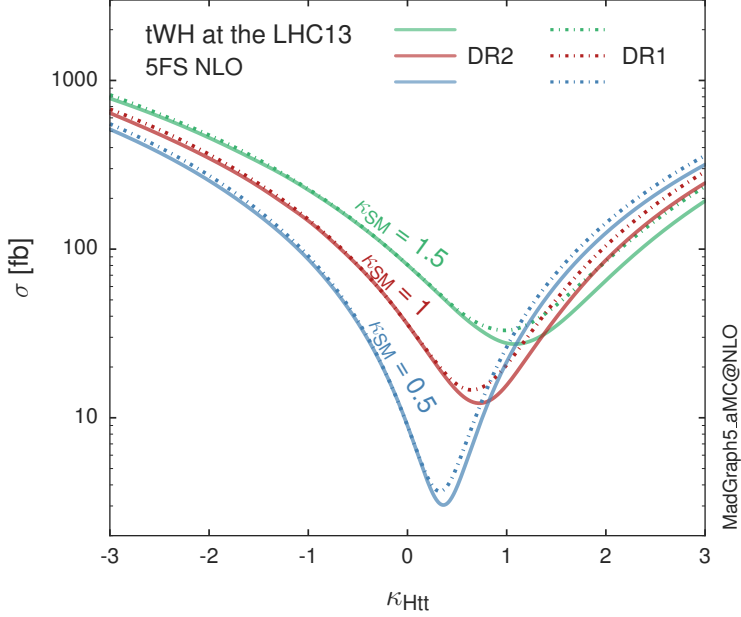


**Figure 2.15:** Cross section for  $tHW$  process as a function of  $\kappa_{Htt}$ , for three values of  $\kappa_{SM}$  at  $\sqrt{s} = 13$  TeV.  $\kappa_{Htt}^2 = \sigma_{Htt}/\sigma_{Htt}^{SM}$  is a simple rescaling of the SM Higgs interactions.

ditional interference with the production of Higgs boson and a top pair process( $t\bar{t}H$ ).  
The calculations are made using the so-called Diagram Removal (DR) technique where  
interfering diagrams are removed (or added) from the calculations in order to evaluate  
the impact of the removed contributions. DR1 was defined to neglect  $t\bar{t}H$  interference  
while DR2 was defined to take  $t\bar{t}H$  interference into account [55]. As shown in figure  
2.15, the  $tHW$  cross section is enhanced from about 15 fb (SM:  $\kappa_{Htt} = 1$ ) to about  
150 fb ( $\kappa_{Htt} = -1$ ). Differences between curves for DR1 and DR2 help to gauge the  
impact of the interference with  $t\bar{t}H$ .  
Results of the calculations of the  $tHq$  and  $tHW$  cross sections at  $\sqrt{s} = 13$  TeV can be  
found in reference [56] and a summary of the results is presented in table 2.11.

	$\sqrt{s}$ TeV	$\kappa_t = 1$	$\kappa_t = -1$
$\sigma^{LO}(tHq)(\text{fb})$ [48]	8	$\approx 17.4$	$\approx 252.7$
	14	$\approx 80.4$	$\approx 1042$
$\sigma^{NLO}(tHq)(\text{fb})$ [48]	8	$18.28^{+0.42}_{-0.38}$	$233.8^{+4.6}_{-0.0}$
	14	$88.2^{+1.7}_{-0.0}$	$982.8^{+28}_{-0.0}$
$\sigma^{LO}(tHq)(\text{fb})$ [54]	14	$\approx 71.8$	$\approx 893$
$\sigma^{LO}(tHW)(\text{fb})$ [54]	14	$\approx 16.0$	$\approx 139$
$\sigma^{NLO}(tHq)(\text{fb})$ [56]	8	$18.69^{+8.62\%}_{-17.13\%}$	-
	13	$74.25^{+7.48\%}_{-15.35\%}$	$848^{+7.37\%}_{-13.70\%}$
	14	$90.10^{+7.34\%}_{-15.13\%}$	$1011^{+7.24\%}_{-13.39\%}$
$\sigma^{LO}(tHW)(\text{fb})$ [55]	13	$15.77^{+15.91\%}_{-15.76\%}$	-
$\sigma^{NLO}DR1(tHW)(\text{fb})$ [55]	13	$21.72^{+6.52\%}_{-5.24\%}$	$\approx 150$
$\sigma^{NLO}DR2(tHW)(\text{fb})$ [55]	13	$16.28^{+7.34\%}_{-15.13\%}$	$\approx 150$

**Table 2.11:** Predicted enhancement of the  $tHq$  and  $tHW$  cross sections at LHC for  $\kappa_V = 1$  and  $\kappa_t = \pm 1$  at LO and NLO; the cross section enhancement of more than a factor of 10 is due to the flippling in the sign of the H-t coupling with respect to the SM one.

## 869 2.5 The CP-mixing in tH processes

870 In addition to the sensitivity to sign of the H-t coupling,  $tHq$  and  $tHW$  processes have  
 871 been proposed as a tool to investigate the possibility of a H-t coupling that does not  
 872 conserve CP [50, 55, 57]. Current experimental results are consistent with SM H-V  
 873 and H-t couplings; however, negative H-t coupling is not excluded completely [59].

874

875 In this thesis, the sensitivity of  $th$  processes to CP-mixing is also studied in the  
 876 effective field theory framework and based in references [50, 55]; a generic particle  
 877 ( $X_0$ ) of spin-0 and a general CP violating interaction with the top quark, can couple  
 878 to scalar and pseudoscalar fermionic densities. The H-W interaction is assumed to  
 879 be SM-like. The Lagrangian modeling the H-t interaction is given by

$$877 \quad \mathcal{L}_0^t = -\bar{\psi}_t (c_\alpha \kappa_{Htt} g_{Htt} + i s_\alpha \kappa_{Att} g_{Att} \gamma_5) \psi_t X_0, \quad (2.58)$$

880 where  $\alpha$  is the CP-mixing phase,  $c_\alpha \equiv \cos \alpha$  and  $s_\alpha \equiv \sin \alpha$ ,  $\kappa_{Htt}$  and  $\kappa_{Att}$  are real  
 881 dimensionless rescaling parameters<sup>9</sup>,  $g_{Htt} = g_{Att} = m_t/v = y_t/\sqrt{2}$  and  $v \sim 246$  GeV is  
 882 the Higgs vacuum expectation value. In this parametrization, it is easy to recover  
 883 three special cases

- 884     • CP-even coupling  $\rightarrow \alpha = 0^\circ$
- 885     • CP-odd coupling  $\rightarrow \alpha = 90^\circ$
- 886     • SM coupling  $\rightarrow \alpha = 0^\circ$  and  $\kappa_{Htt} = 1$

887 The loop induced  $X_0$  coupling to gluons can also be described in terms of the  
 888 parametrization above, according to

$$\mathcal{L}_0^g = -\frac{1}{4} \left( c_\alpha \kappa_{Hgg} g_{Hgg} G_{\mu\nu}^a G^{a,\mu\nu} + s_\alpha \kappa_{Agg} g_{Agg} G_{\mu\nu}^a \tilde{G}^{a,\mu\nu} \right) X_0. \quad (2.59)$$

889 where  $g_{Hgg} = -\alpha_s/3\pi v$  and  $g_{Agg} = \alpha_s/2\pi v$ . Under the assumption that the top quark  
 890 dominates the gluon-fusion process at LHC energies,  $\kappa_{Hgg} \rightarrow \kappa_{Htt}$  and  $\kappa_{Agg} \rightarrow \kappa_{Att}$ ,  
 891 so that the ratio between the gluon-gluon fusion cross section for  $X_0$  and for the SM  
 892 Higgs prediction can be written as

$$\frac{\sigma_{NLO}^{gg \rightarrow X_0}}{\sigma_{NLO,SM}^{gg \rightarrow H}} = c_\alpha^2 \kappa_{Htt}^2 + s_\alpha^2 \left( \kappa_{Att} \frac{g_{Agg}}{g_{Hgg}} \right)^2. \quad (2.60)$$

893 If the rescaling parameters are set to

$$\kappa_{Htt} = 1, \quad \kappa_{Att} = \left| \frac{g_{Hgg}}{g_{Agg}} \right| = \frac{2}{3}. \quad (2.61)$$

894 the gluon-fusion SM cross section is reproduced for every value of the CP-mixing  
 895 angle  $\alpha$ ; therefore, by imposing that condition to the Lagrangian density 2.58, the

---

<sup>9</sup> analog to  $\kappa_t$  and  $\kappa_V$

CP-mixing angle is not constrained by current data. Figure 2.16 shows the NLO cross sections for t-channel  $tX_0$ (blue) and  $t\bar{t}X_0$  (red) associated production processes as a function of the CP-mixing angle  $\alpha$ .  $X_0$  is a generic spin-0 particle with top quark CP-violating coupling. Rescaling factors  $\kappa_{Htt}$  and  $\kappa_{Att}$  have been set to reproduce the SM gluon-fusion cross sections.

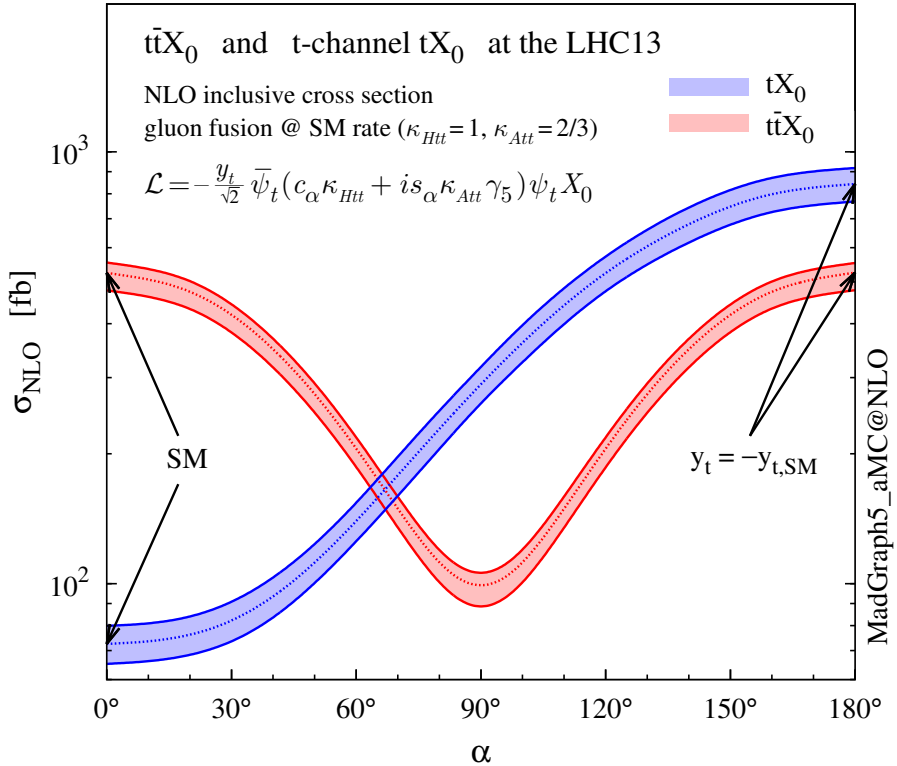


**Figure 2.16:** NLO cross sections for t-channel  $tX_0$ (blue) and  $t\bar{t}X_0$  (red) associated production processes as a function of the CP-mixing angle  $\alpha$ .  $X_0$  is a generic spin-0 particle with top quark CP-violating coupling [50].

It is interesting to notice that the  $tX_0$  cross section is enhanced, by a factor of about 10, when a continuous rotation in the scalar-pseudoscalar plane is applied; this enhancement is similar to the enhancement produced when the H-t coupling is flipped in sign with respect to the SM ( $y_t = -y_{t,SM}$  in the plot), as showed in section 2.4. In contrast, the degeneracy in the  $t\bar{t}X_0$  cross section is still present given that it depends

quadratically on the H-t coupling, but more interesting is to notice that  $t\bar{t}X_0$  cross section is exceeded by  $tX_0$  cross section after  $\alpha \sim 60^\circ$ .

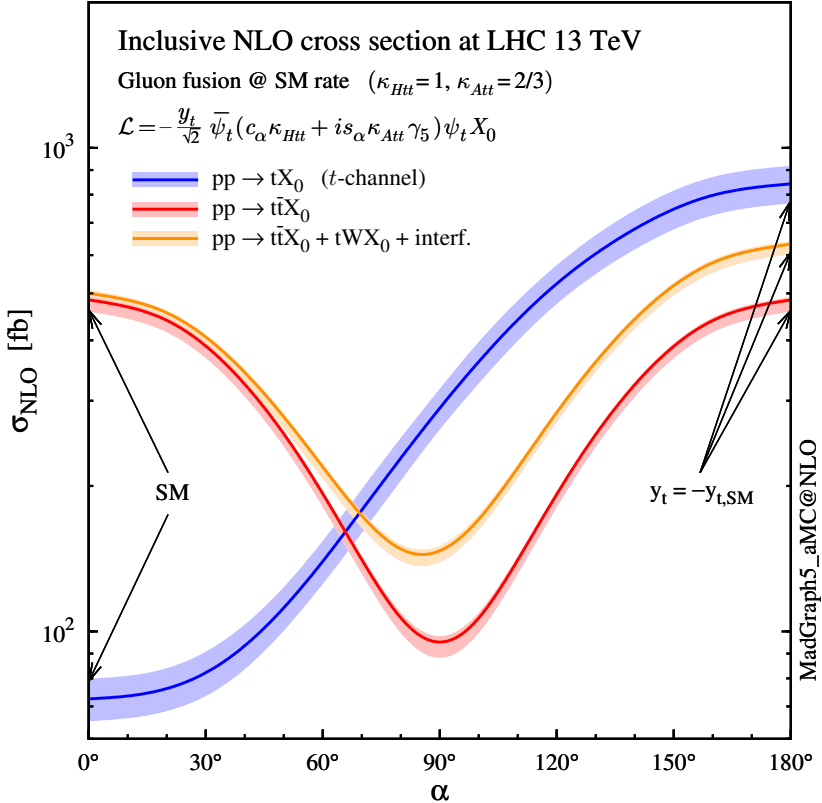


**Figure 2.17:** NLO cross sections for t-channel  $tX_0$ (blue),  $t\bar{t}X_0$  (red) associated production processes and combined  $tWX_0 + t\bar{t}X_0$  (including interference) production as a function of the CP-mixing angle  $\alpha$  [50].

907

908 A similar parametrization can be used to investigate the  $tHW$  process sensitivity to  
909 CP-violating H-t coupling. As said in 2.4, the interference in the W-associated chan-  
910 nel is more complicated because there are more than two contributions and also there  
911 is interference with the  $t\bar{t}H$  production process.

912

913 Figure 2.17 shows the NLO cross sections for t-channel  $tX_0$ (blue),  $t\bar{t}X_0$  (red) asso-  
914 ciated production and for the combined  $tWX_0 + t\bar{t}X_0 +$  interference (orange) as a  
915 function of the CP-mixing angle. It is clear that the effect of the interference in the

916 combined case is the lifting of the degeneracy present in the  $t\bar{t}X_0$  production. The  
 917 constructive interference enhances the cross section from about 500 fb at SM ( $\alpha = 0$ )  
 918 to about 600 fb ( $\alpha = 180^\circ \rightarrow y_t = -y_{t,SM}$ ).

919 An analysis combining  $tHq$  and  $tHW$  processes will be made in this thesis taking  
 920 advantage of the sensitivity improvement.

921 **2.6 Experimantal status of anomalous**  
 922 **Higg-fermion coupling.**

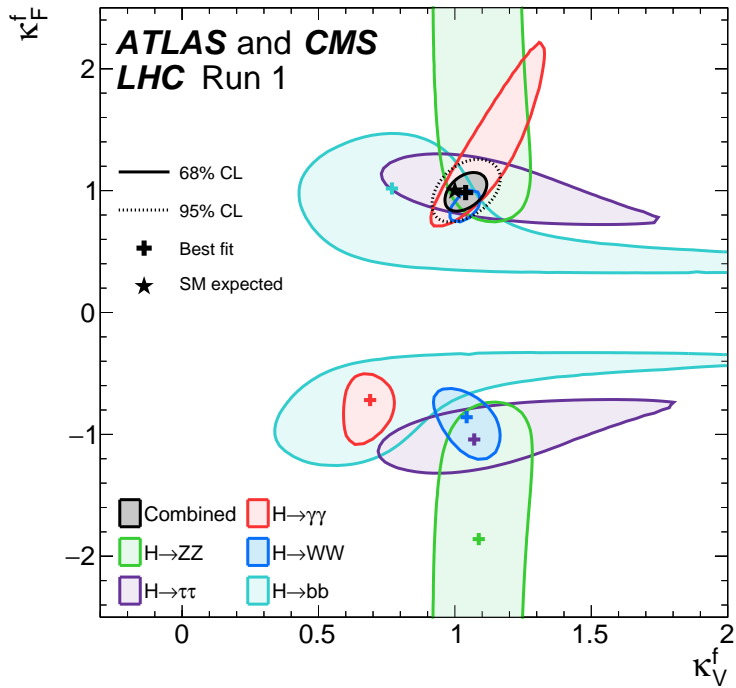


**Figure 2.18:** Combination of coupling modifiers  $\kappa_t$ - $\kappa_V$  fits of ATLAS and CMS; also shown the individual decay channels combination and their global combination. No assumptions have been made on the sign of the coupling modifiers [59].

923 ATLAS and CMS have performed analysis of the anomalous H-f coupling by making  
 924 likelihood scans for the two coupling modifiers,  $\kappa_t$  and  $\kappa_V$ , under the assumption that

925  $\kappa_Z = \kappa_W = \kappa_V$  and  $\kappa_t = \kappa_\tau = \kappa_b = \kappa_f$ . Figure 2.18 shows the result of the combination  
926 of ATLAS and CMS fits; also the individual decay channels combination and the  
927 global combination result are shown.

928 While all the channels are compatible for positive values of the modifiers, for negative  
929 values of  $\kappa_t$  there is no compatibility. The best fit for individual channels is compatible  
930 with negative values of  $\kappa_t$  except for the  $H \rightarrow bb$  channel which is expected to be the  
931 most sensitive channel; therefore, the best fit for the global fit yields  $\kappa_t \geq 0$ . Thus,  
932 the anomalous H-t coupling cannot be excluded completely.

<sub>933</sub> **Chapter 3**

<sub>934</sub> **The CMS experiment at the LHC**

<sub>935</sub> **3.1 Introduction**

<sub>936</sub> Located in the Swiss-French border, the European Council for Nuclear Research  
<sub>937</sub> (CERN) is the largest scientific organization leading the particle physics research.  
<sub>938</sub> About 13000 people in a broad range of fields including users, students, scientists,  
<sub>939</sub> engineers among others, contribute to the data taking and analysis, with the goal  
<sub>940</sub> of unveiling the secrets of the nature and revealing the fundamental structure of the  
<sub>941</sub> universe. CERN is also the home of the Large Hadron Collider (LHC), the largest  
<sub>942</sub> circular particle accelerator around the world, where protons (or heavy ions) travel-  
<sub>943</sub> ing close to the speed of light, are made to collide. These collisions open a window  
<sub>944</sub> to investigate how particles (and their constituents if they are composite) interact  
<sub>945</sub> with each other, providing clues about the laws of the nature. This chapter present  
<sub>946</sub> an overview of the LHC structure and operation. A detailed description of the CMS  
<sub>947</sub> detector is offered, given that the data used in this thesis have been taken with this  
<sub>948</sub> detector.

## 949 3.2 The LHC

950 With 27 km of circumference, the LHC is currently the largest and most powerful  
 951 accelerator in the world. It is installed in the same tunnel where the large Electron-  
 952 Positron (LEP) collider was located, taking advantage of the existing infraestructure.  
 953 The LHC is also the larger accelerator in the CERN's accelerator complex and is  
 954 assisted by several successive accelerating stages before the particles are injected into  
 955 the LHC ring where they reach their maximum eneregy (see figure 3.1).

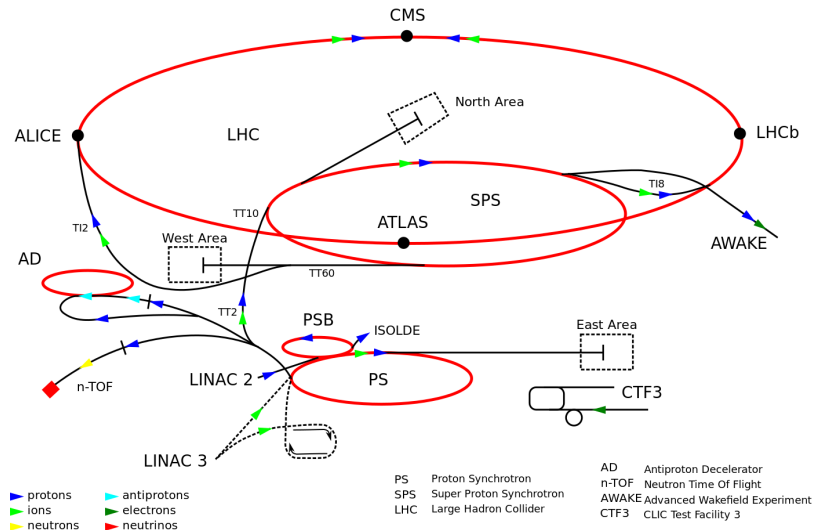


**Figure 3.1:** CERN accelerator complex. Blue arrows show the path followed by protons along the acceleration process [60].

956 LHC run in three modes depending on the particles being accelerated

- 957     ● Proton-Proton collisions (pp) for multiple physics experiments.
- 958     ● Lead-Lead collisions (Pb-Pb) for heavy ion experiments.
- 959     ● Proton-Lead collisions (p-Pb) for quark-gluon plasma experiments.

960 In this thesis pp collisions will be considered.

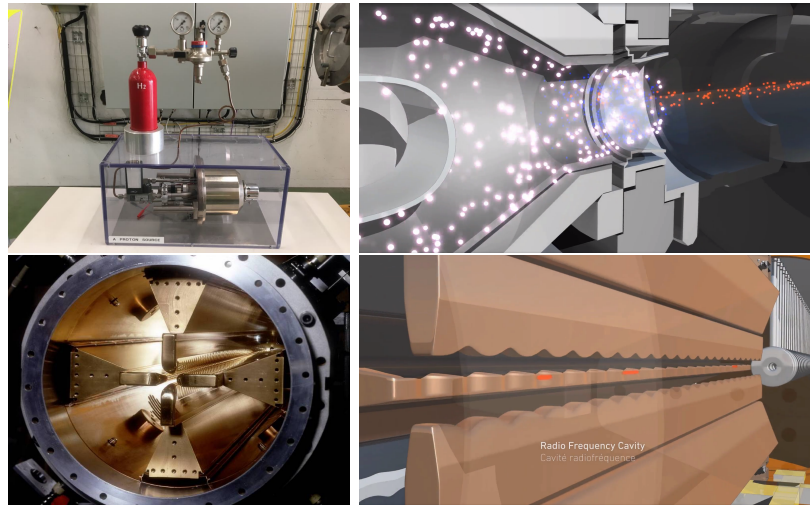


**Figure 3.2:** LHC protons source and first acceleration stage. Top: the bottle contains hydrogen gas (white dots) which is injected into the metal cylinder to be broken down into electrons(blue dots) and protons(red dots); Bottom: the obtained protons are directed towards the radio frequency quadrupole which perform the first acceleration, focus the beam and create the bunches of protons. [64, 65]

962 Collection of protons starts with hydrogen atoms taken from a bottle, containing hy-  
 963 drogen gas, and injecting them in a metal cillinder; hydrogen atoms are broken down  
 964 into electrons and protons by an intense electric field (see figure3.2 top). The result-  
 965 ing protons leave the metal cylinder towards a radio frecuency quadrupole (RFQ)  
 966 that focus the beam, accelerate the protons and create the packets of protons called  
 967 bunches. In the RFQ, an electric field is generated by a RF wave at a frecuency that  
 968 matches the resonance frecuency of the cavity where the electrodes are contained.  
 969 The beam of protons traveling on the RFQ axis experience an alternating electric  
 970 field gradient that generates the focusing forces.

971

972 In order to accelerate the protons, a longitudinal time-varying electric field compo-  
 973 nent is added to the system; it is done by giving the electrodes a sinus-like profile as  
 974 shown in figure 3.2 bottom. By matching the speed and phase of the protons with the  
 975 longitudinal electric field the bunching is performed; protons synchronized with the

976 RFQ (synchronous proton) does not feel an accelerating force, but those protons in  
 977 the beam that have more (or less) energy than the synchronous proton (asynchronous  
 978 protons) will feel a decelerating (accelerating) force; therefore, asynchronous protons  
 979 will oscillate around the synchronous ones forming bunches of protons [62]. From  
 980 the RFQ emerges protons with energy 750 keV in bunches of about  $1.15 \times 10^{11}$  pro-  
 981 tons [63].

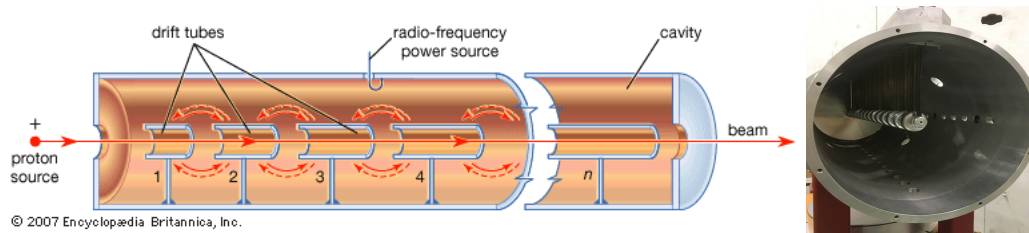


**Figure 3.3:** The LINAC2 accelerating system at CERN. Radio frequency (RF) generated electric fields create acceleration and deceleration zones inside the cavity; deceleration zones are blocked by drift tubes where quadrupole magnets focus the proton beam. [66]

982 Proton bunches coming from the RFQ goes to the linear accelerator 2 (LINAC2)  
 983 where they are accelerated to reach 50 MeV energy. In the LINAC2 stage, acceler-  
 984 ation is performed using radio frequency generated electric fields which create zones  
 985 of acceleration and deceleration as shown in figure 3.3. In the decelerations zones  
 986 the electric field is blocked using drift tubes where protons are free to drift while  
 987 quadrupole magnets focus the beam.

988

989 The beam coming from LINAC2 is injected into the proton synchrotron booster  
 990 (PSB) to reach 1.4 GeV in energy. The next acceleration is provided at the pro-  
 991 ton synchrotron (PS) up to 26 GeV, followed by the injection into the super proton  
 992 synchrotron (SPS) where protons are accelerated to 450 GeV. Finally, protons are  
 993 injected into the LHC where they are accelerated to the target energy of 6.5 TeV.  
 994 PSB, PS, SPS and LHC accelerate protons using the same RF acceleration technic

described before.

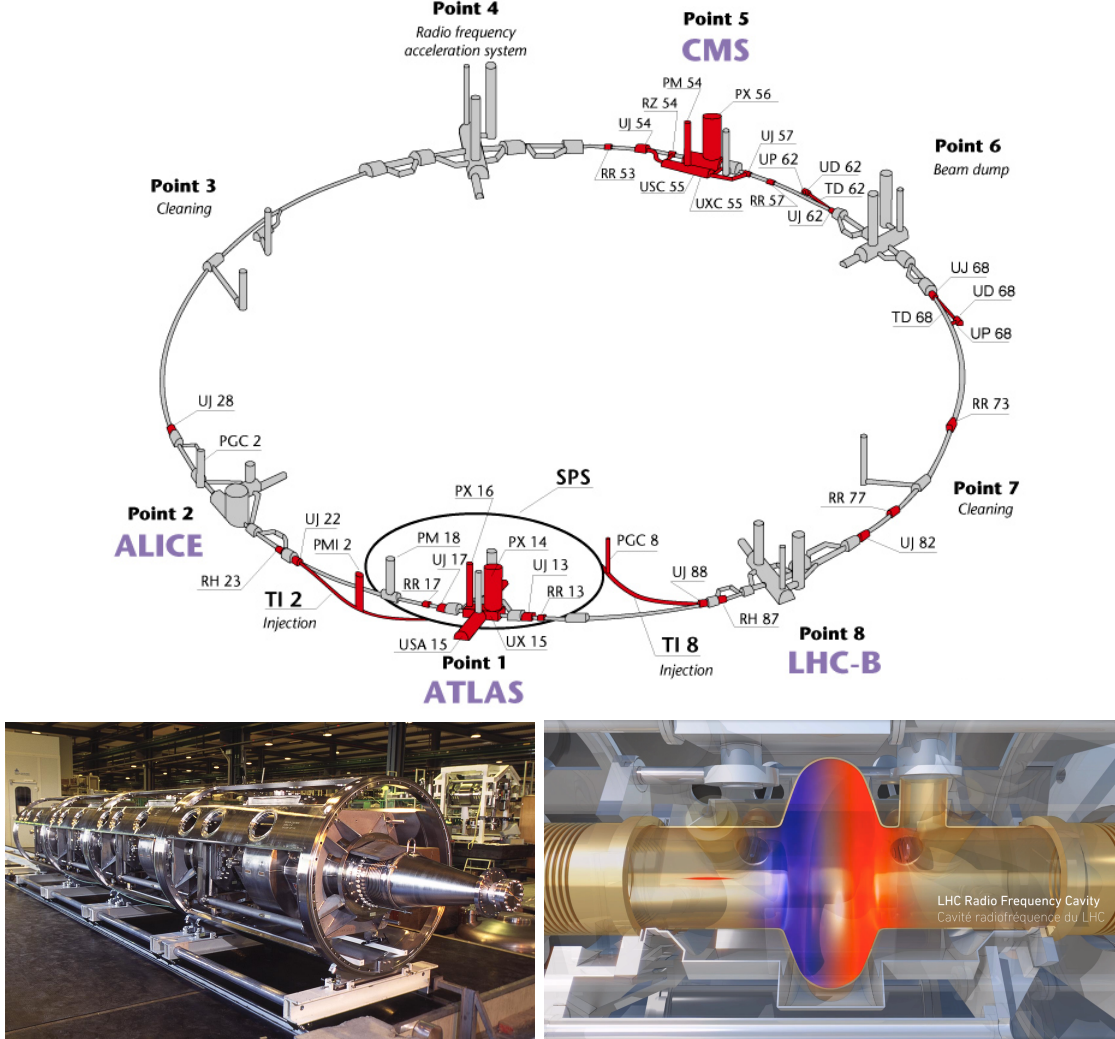


**Figure 3.4:** Top: LHC layout. The red zones indicate the infrastructure additions to the LEP installations, built to accomodate the ATLAS and CMS experiments which exceed the size of the former experiments located there [61]. Bottom: LHC RF cavities. A module accomodates 4 cavities that accelerate protons and preserve the bunch structure of the beam. [65, 67]

LHC have a system of 16 RF cavities located in the so-called point 4, as shown in figure 3.4 top, tunned at a freqency of 400 MHz and the protons are carefully timed so additionally to the acceleration effect the bunch structure of the beam is preserved. Bottom side of figure 3.4 shows a picture of a Rf module composed of 4 RF cavities

1000 working in a superconducting state at 4.5 K; also is showed a representation of the  
 1001 accelerating electric field that accelerates the protons in the bunch.

1002

1003 While protons are accelerated in one section of the LHC ring, where the RF cavities  
 1004 are located, in the rest of their path they have to be kept in the curved trajectory  
 1005 defined by the LHC ring. Technically, LHC is not a perfect circle; RF, injection, beam  
 1006 dumping, beam cleaning and sections before and after the experimental points where  
 1007 protons collide are all straight sections. In total, there are 8 arcs 2.45 Km long each  
 1008 and 8 straight sections 545 m long each. In order to curve the proton's trajectory in  
 1009 the the arc sections, superconducting dipole magnets are used.

1010

1011 Inside the LHC ring, there are two proton beams traveling in opposite directions in  
 1012 two separated beam pipes; the beam pipes are kept at ultra high vacuum ( $\sim 10^{-9}$   
 1013 Pa) to ensure that there are no particles that interact with the proton beams. The  
 1014 superconducting dipole magnets used in LHC are made of a NbTi alloy, capable of  
 1015 transporting currents of about 12000 A when cooled at a temperature below 2K using  
 1016 liquid helium (see figure 3.5).

1017 Protons in the arc sections of LHC feel a centripetal force exerted by the dipole  
 1018 magnets which is perpendicular to the beam trajectory; The magnitude of magnetic  
 1019 field needed can be found assuming that protons travel at  $v \approx c$ , using the standard  
 1020 values for proton mass and charge and the LHC radius, as

$$F_m = \frac{mv^2}{r} = qBv \quad \rightarrow B = 8.33T \quad (3.1)$$

1021 wich is about 100000 times the Earth's magnetic field. A representation of the mag-  
 1022 netic field generated by the dipole magnets is shown in the bottom left side of figure

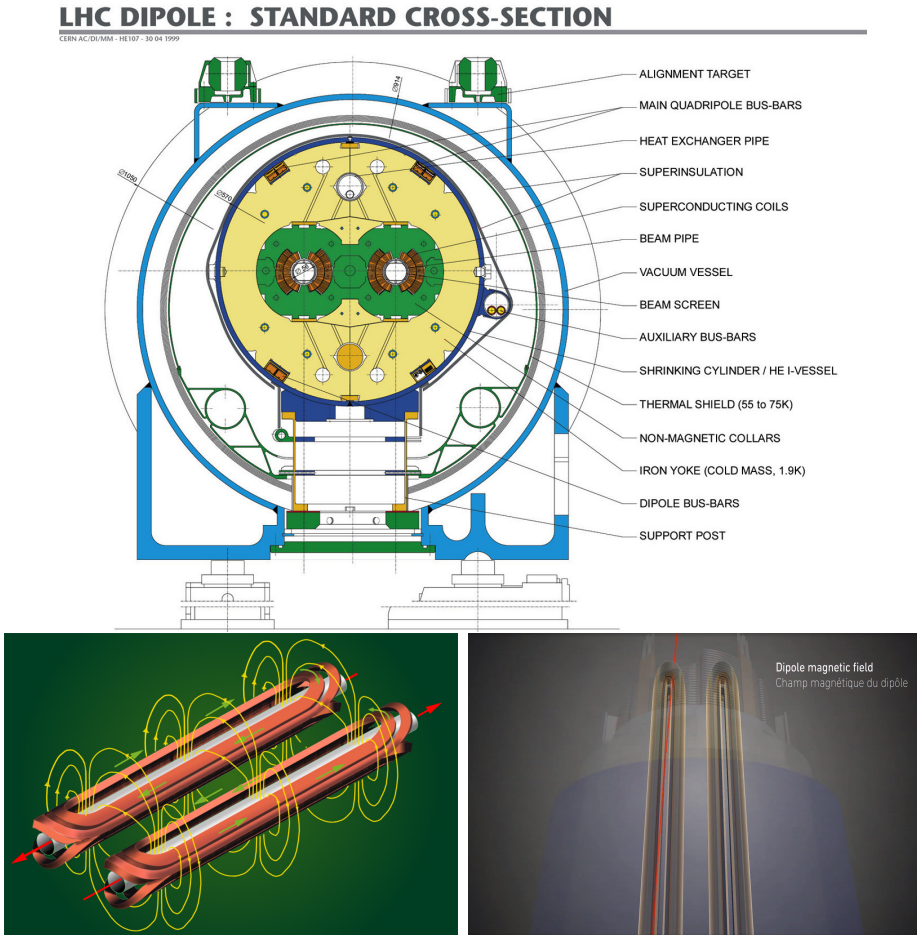


**Figure 3.5:** Top: LHC dipole magnet transversal view; cooling, shielding and mechanical support are indicated. Bottom left: Magnetic field generated by the dipole magnets; note that the direction of the field inside one beam pipe is opposite with respect to the other beam pipe which guarantee that both proton beams are curved in the same direction towards the center of the ring. The effect of the dipole magnetic field on the proton beam is represented in the bottom right side [65, 68, 69].

1023 3.5. The bending effect of the magnetic field on the proton beam is shown in the  
 1024 bottom right side of figure 3.5. Note that the dipole magnets are not curved; the arc  
 1025 section of the LHC ring is composed of straight dipole magnets of about 15 m. In  
 1026 total there are 1232 dipole magnets along the LHC ring.  
 1027 In addition to bending the beam trajectory, the beam has to be focused so it stays in  
 1028 side the beam pipe. The focusing is performed by quadrupole magnets installed in

1029 another straight section; in total 858 quadrupole magnets are installed along the LHC  
 1030 ring. Other effects like electromagnetic interaction among bunches, interaction with  
 1031 electron clouds from the beam pipe, gravitational force on the protons, differences in  
 1032 energy among protons in the same bunch, among others, are corrected using sextupole  
 1033 and other magnetic multipoles.

1034 The two proton beams inside the LHC ring are made of bunches with a cylindrical  
 1035 shape of about 7.5 cm long and about 1 mm in diameter; when bunches are close  
 1036 to the collision point (CP), the beam is focused up to a diameter of about 16  $\mu\text{m}$   
 1037 in order to maximize the luminosity ( $L$ ) defined as the number of collisions per unit  
 1038 area and per second. Luminosity can be calculated using

$$L = fn \frac{N_1 N_2}{4\pi\sigma_x\sigma_y} \quad (3.2)$$

1039 where  $f$  is the revolution frequency,  $n$  is the number of bunches per beam,  $N_1$  and  $N_2$   
 1040 are the number of protons per bunch,  $\sigma_x$  and  $\sigma_y$  are the gaussian transverse sizes of  
 1041 the bunches. Using

$$f = \frac{v}{2\pi r_{LHC}} \approx \frac{3 \times 10^8 \text{ m/s}}{27 \text{ km}} \approx 11.1 \text{ kHz},$$

$$n = 2808$$

$$N_1 = N_2 = 1.5 \times 10^{11}$$

$$\sigma_x = \sigma_y = 16 \mu\text{m}$$

1042  
 1043 Luminosity is a fundamental aspect for LHC given that the bigger luminosity, the  
 1044 bigger number of collisions, which means that for processes with a very small cross

$$L = 1.28 \times 10^{34} \text{ cm}^{-2} \text{ s}^{-1} \quad (3.3)$$

section the number of expected occurrences is increased and so the chances of being detected. The integrated luminosity collected by the CMS experiment during 2016 is shown in figure 3.6; the data analyzed in this thesis corresponds to an integrated luminosity of  $35.9 \text{ fb}^{-1}$  at  $\sqrt{s} = 13 \text{ TeV}$ .

A way to increase L is increasing the number of bunches in the beam. Currently, the separation between two consecutive bunches in the beam is 7.5 m which corresponds to a time separation of 25 ns. In the full LHC ring the allowed number of bunches is  $n = 27\text{km}/7.5\text{m} = 3600$ ; however, there are some gaps in the bunch pattern intended for preparing the dumping and injection of the beam, thus, the proton beams are composed of 2808 bunches.

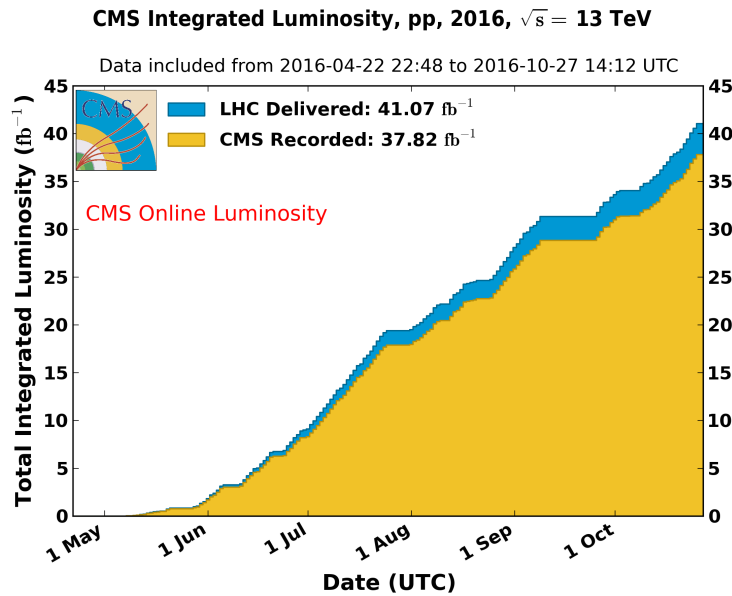


**Figure 3.6:** Integrated luminosity delivered by LHC and recorded by CMS during 2016. The difference between the delivered and the recorded luminosities is due to fails and issues occurred during the data taking in the CMS experiment [70].

Once the proton beams reach the desired energy, they are brought to cross each other producing proton-proton collisions. The bunch crossing happens in precise places where the four LHC experiments are located, as seen in figure 3.7 left. In 2008, the

1058 first set of collisions involved protons with  $\sqrt{s} = 7$  TeV; the energy was increased to  
 1059 8 TeV in 2012 and to 13 TeV in 2015.

1060 CMS and ATLAS experiments, which are multi-purpose experiments, are enabled  
 1061 to explore physics in any of the collision modes. LHCb experiment is optimized  
 1062 to explore bottom quark physics, while ALICE is optimized for heavy ion collisions  
 1063 searches; TOTEM and LHCf are dedicated to forward physics studies; MoEDAL (not  
 1064 indicated in the figure) is intended for monopoles or massive pseudo stable particles  
 1065 searches.

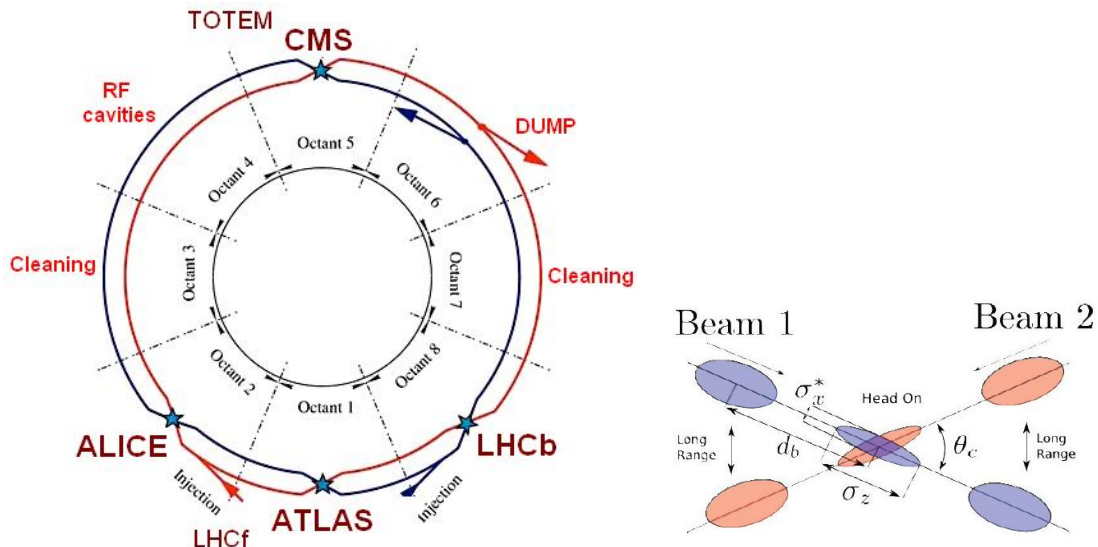


**Figure 3.7:** Left: LHC interaction points. Bunch crossing occurs where the LHC experiments are located [71]. Sections indicated as cleaning are dedicated to collimate the beam in order to protect the LHC ring from collisions with protons in very spreaded bunches. Right: bunch crossing scheme. Since the bunch crossing is not perfectly head-on, the luminosity is reduced in a factor of 17%.

1066 At the CP there are two interesting details that need to be addressed. The first  
 1067 one is that the bunch crossing does not occur head-on but at a small crossing angle  
 1068 (280  $\mu$ rad in CMS and ATLAS) as shown in the right side of figure 3.7, affecting the  
 1069 overlapping between bunches; the consequence is a reduction of about 17% in the  
 1070 luminosity. The second one is occurrence of multiple pp collisions in the same bunch

1071 crossing; this effect is called pile-up (PU). A fairly simple estimation of the PU follows  
 1072 from estimating the probability of collision between two protons, one from each of  
 1073 the bunches in course of collision; it depends roughly on the ratio of proton size and  
 1074 the cross section of the bunch in the interaction point, i.e.,

$$P(pp\text{-}collision) \sim \frac{d_{proton}^2}{\sigma_x \sigma_y} = \frac{(1fm)^2}{(16\mu m)^2} \sim 4 \times 10^{-21} \quad (3.4)$$

1075 however, there are  $N = 1.15 \times 10^{11}$  protons in a bunch, thus the estimated number of  
 1076 collisions in a bunch crossing is

$$PU = N^2 * P(pp\text{-}collision) \sim 50 \text{ pp-collision per bunch crossing}, \quad (3.5)$$

1077 about 20 of those pp collisions are inelastic. Each collision generates a vertex, but  
 1078 only the most energetic is considered as a primary vertex; the rest are considered  
 1079 as PU vertices. A simulation of a multiple pp collision event in a bunch crossing at  
 1080 CMS is showed in figure3.8. Unstable particles outgoing from the primary vertex will  
 1081 eventually decay; this decay vertex is known as a secondary vertex.

1082 When the beams are exhausted, i.e. the number of protons in the bunches is reduced  
 1083 beyond a limit, or in case of emergency, the beams have to be extracted from the  
 1084 beam pipes; the dumping system, in the dump section, perform the extraction safely  
 1085 by directing the beams towards graphite blocks that absorb the beam energy.

1086

1087 Next section present a description of the CMS detector, since it is the detector used  
 1088 to collect the data used in this thesis.

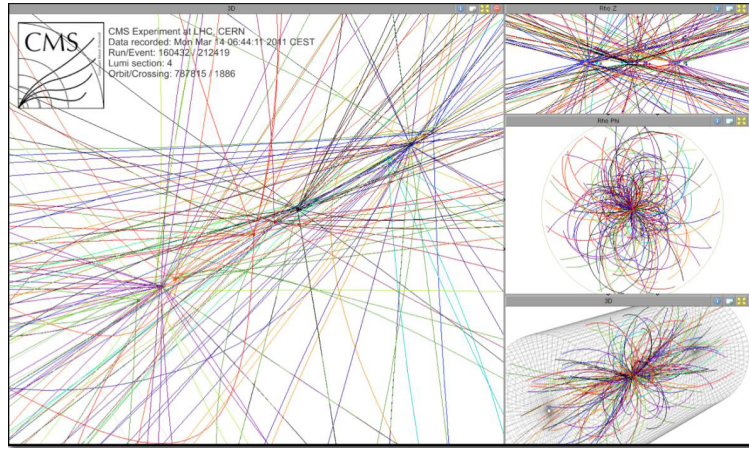


**Figure 3.8:** Multiple pp collision bunch crossing at CMS. Only the most energetic vertex is considered and the rets are cataloged as PU vertices [].

### 1089    3.3 The CMS experiment

1090 CMS is a general purpose detector designed to conduct research in a wide range of  
 1091 physics from standard model to new physics like extra dimensions and dark matter.  
 1092 Located at the point 5 in the LHC layout as shown in figure 3.4, CMS is composed  
 1093 of several detection systems distributed in a cylindrical structure,. In total, CMS  
 1094 weights about 12500 tons in a very compact 21.6 m long and 14.6 m diameter cylin-  
 1095 der. It was built in 15 separate sections at the ground level and lowered to the  
 1096 cavern individually to be assembled. A complete and detailed description of the CMS  
 1097 detector and its components is given in reference [72] on which this section is based in.  
 1098

1099 Figure 3.9 shows the layout of the CMS detector. The design is driven by the require-  
 1100 ments on the identification, momentum resolution and unambiguous charge determi-  
 1101 nation of the muons; therefore, a large bending power is provided by the solenoid  
 1102 magnet made of superconducting cable capable to generate a 3.8 T magnetic field.  
 1103 The detection system is composed of (from the innermost to the outermost)

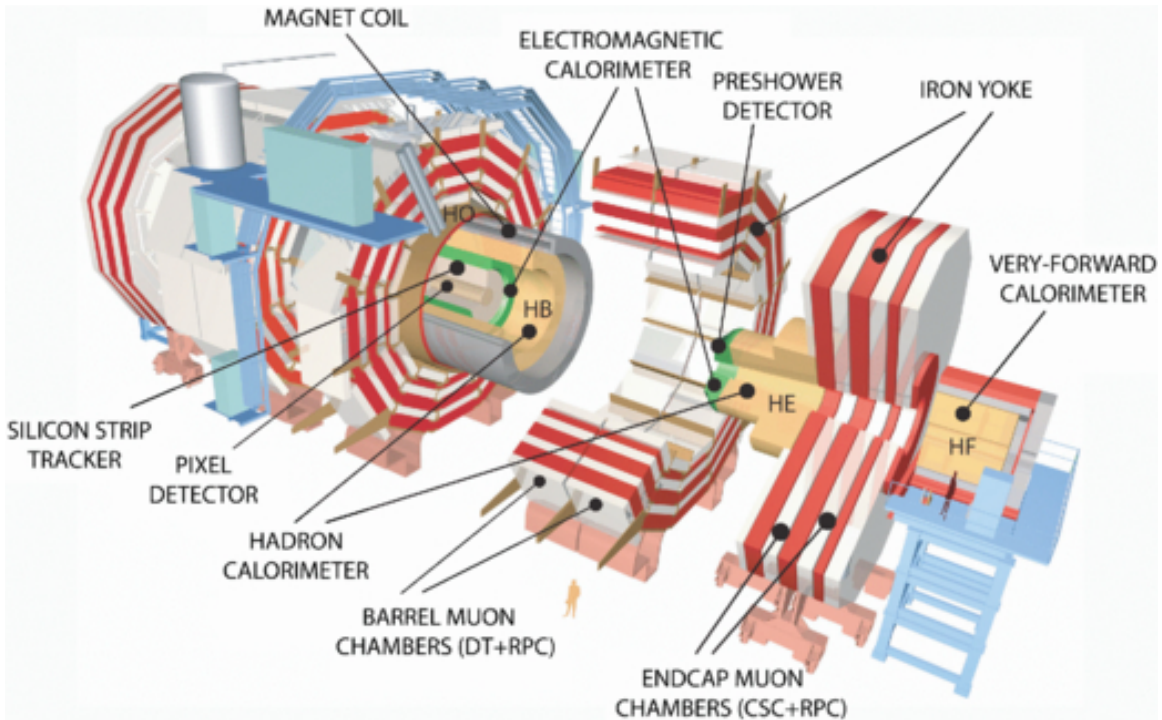


**Figure 3.9:** CMS detector drawing. The several subdetectors are indicated. The central region of the detector is referred as the Barrel section while the endcaps are referred as the forward sections. [73].

- 1104      • Pixel detector.
- 1105      • Silicon strip tracker.
- 1106      • Preshwoer detector.
- 1107      • Electromagnetic calorimeter.
- 1108      • Hadronic calorimeter.
- 1109      • Muon chambers (Barrel and endcap)
  
- 1110     The central region of the detector is commonly referred as the barrel section while the
- 1111     endcaps are referred as the forward sections of the detector; thus, each subdetector
- 1112     is composed of a barrel section and a forward section.

### 1113 3.3.1 Coordinate system

1114 The coordinate system used by CMS is centered in the geometrical center of the  
 1115 detector which is the same as the CP as shown in figure3.10. The  $z$ -axis is parallel  
 1116 to the beam direction, while the  $Y$ -axis pointing vertically upward, and the  $X$ -axis  
 1117 pointing radially inward toward the center of the LHC.

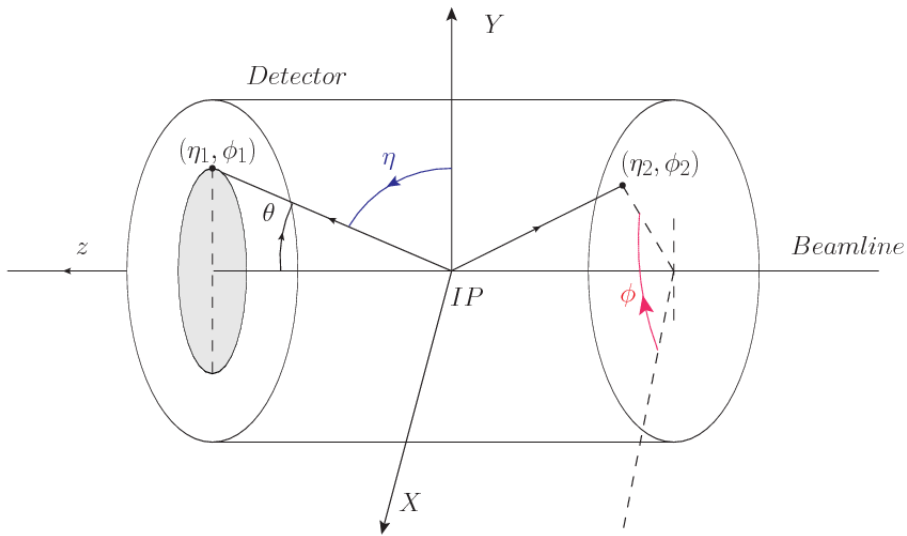


**Figure 3.10:** CMS coordinate system.

1118 In addition to the common cartesian and cylindrical coordinate systems, two coordi-  
 1119 nates are of particular utility in particle physics: rapidity( $y$ ) and pseudorapidity( $\eta$ ),  
 1120 defined in connection to the polar angle  $\theta$ , energy and longitudinal momentum com-  
 1121 ponent (momentum along the  $z$ -axis) according to

$$y = \frac{1}{2} \ln \frac{E + p_z}{E - p_z} \quad \eta = -\ln \left( \tan \frac{\theta}{2} \right) \quad (3.6)$$

1122 Rapidity is related to the angle between the  $XY$ -plane and the direction in which  
 1123 the products of a collision are emitted; it has the nice property that the difference  
 1124 between the rapidities of two particles is invariant with respect to Lorentz boosts  
 1125 along the  $z$ -axis. Thus, data analysis becomes more simple when based in rapidity;

however, it is not simple to measure the rapidity of highly relativistic particles, as those produced after pp collisions. Under the highly relativistic motion approximation  $y$  can be rewritten in terms of the polar angle, arriving to the conclusion that rapidity is approximately equal to the pseudorapidity defined above, i.e.  $y \approx \eta$ . Note that  $\eta$  is easier to measure than  $y$  given the direct relationship between the former and the polar angle. Angular distance between two objects in the detector ( $\Delta R$ ) is defined in terms of their coordinates  $(\eta_1, \phi_1), (\eta_2, \phi_2)$  as

$$\Delta R = \sqrt{(\Delta\eta)^2 - (\Delta\phi)^2} \quad (3.7)$$

### 3.3.2 Pixels detector

The CMS tracking system is designed to provide a precise measurement of the trajectory followed by the charged particles created after the pp collisions as; also, the precise reconstruction of the primary and secondary vertices is expected in an environment where, each 25 ns, the bunch crossing produce about 20 inelastic collisions and about 1000 particles. An increment in the luminosity is ongoing which implies that the PU will increase accordingly.

1140

The pixel detector was replaced during the 2016-2017 year end shut down, due to the increasingly challenging operation conditions like the higher particle flow and more radiation harsh environment among others. The new one is responding as expected, reinforcing its crucial role in the successful way to fulfil the new LHC physics objectives after the discovery of the Higgs boson. The last chapter of this thesis is dedicated to describe my contribution to the “Forward Pixel Phase 1 upgrade”.

1147

1148 The current pixel detector is composed of 1856 silicon pixel detector modules orga-  
 1149 nized in four barrel layers in the central region and three disks in the forward region;  
 1150 it is designed to record efficiently and with high precision, up to  $10\mu\text{m}$  in the  $XY$ -  
 1151 plane and  $20\mu\text{m}$  in the  $z$ -direction, the first four space-points near to the CP region  
 1152 (see figure 3.11 left side) in the range  $|\eta| \leq 2.5$ . The first barrel layer is located at a  
 1153 radius of 30 mm from the beamline, while the fourth layer is located at a radius of  
 1154 160 mm closer to the strip tracker inner barrel layer (see section 3.3.3) in order to  
 1155 reduce the rate of fake tracks. The high granularity of the detector is represented in  
 1156 its about 123 Mpixels, each of size  $100 \times 150\mu\text{m}^2$ , which is almost twice the channels  
 1157 of the old detector. The transverse momentum resolution of tracks can be measured  
 1158 with a resolution of 1-2% for muons of  $p_T = 100$  GeV.

1159

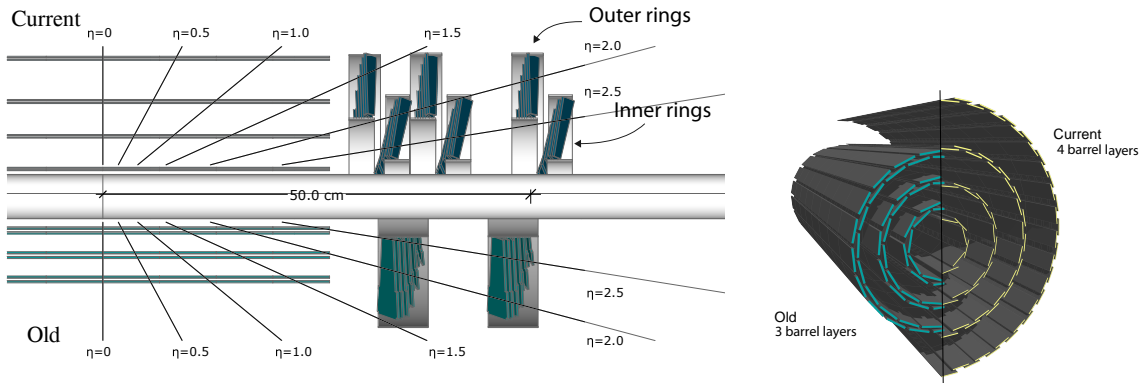


**Figure 3.11:** CMS pixel detector schematic view. Left: layout comparing the layers and disks in the old and current pixel detectors. Right: Transverse-oblique view comparing the pixel barrel layers in the two [75].

1160 Some of the improvements with respect to the previous pixel detector include a higher  
 1161 average tracking efficiency and lower average fake rate as well as higher track impact  
 1162 parameter resolution which is fundamental in order to increase the efficiency in the  
 1163 identification of jets originating from b quarks (b-tagging). A significant source of

improvement comes from the overall reduction in the material budget of the detector which results in less photon conversions and less multiple scattering from charged particles.

### 3.3.3 Silicon strip tracker

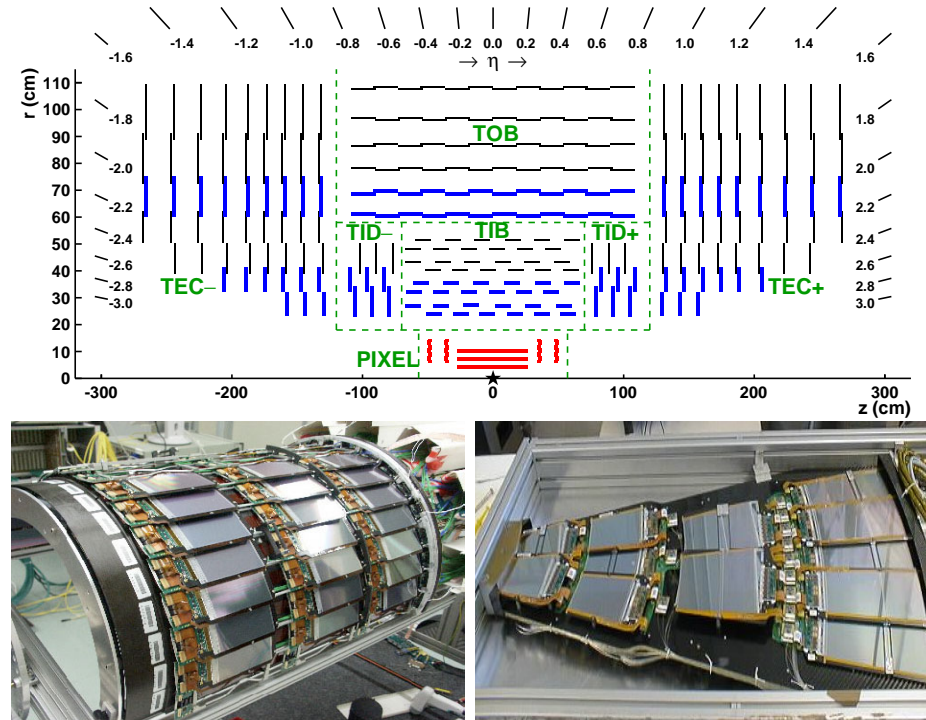


**Figure 3.12:** Top: CMS Silicon Strip Tracker (SST) schematic view. The SST is composed of the tracker inner barrel (TIB), the tracker inner disks (TID), the tracker outer barrel (TOB) and the tracker endcaps (TEC). Each part is made of silicon strip modules; the modules in blue represent two modules mounted back-to-back and rotated in the plane of the module by a stereo angle of 120 mrad in order to provide a 3-D reconstruction of the hit positions. Bottom: pictures of the TIB (left) and TEC (right) modules [76–78].

The silicon strip tracker (SST) is the second stage in the CMS tracking system . The top side of figure 3.12 shows a schematic of the SST. The inner tracker region is composed of the tracker inner barrel (TIB) and the tracker inner disks (TID) covering the region  $r < 55$  cm and  $|z| < 118$  cm. The TIB is composed of 4 layers while the TID

1172 is composed of 3 disks at each end. The silicon sensors in the inner tracker are 320  
1173  $\mu\text{m}$  thick, providing a resolution of about 13-38  $\mu\text{m}$  in the  $r\phi$  position measurement.

1174

1175 The modules indicated in blue in the schematic view of figure 3.12 are two modules  
1176 mounted back-to-back and rotated in the plane of the module by a “stereo” angle of  
1177 100 mrad; the hits from these two modules, known as “stereo hits”, are combined to  
1178 provide a measurement of the second coordinate ( $z$  in the barrel and  $r$  on the disks)  
1179 allowing the reconstruction of hit positions in 3-D.

1180

1181 The outer tracker region is composed of the tracker outer barrel (TOB) and the  
1182 tracker endcaps (TEC). The 6 layers of the TOB offers coverage in the region  $r > 55$   
1183 cm and  $|z| < 118$  cm, while the 9 disks of the TEC cover the region  $124 < |z| < 282$   
1184 cm. The resolution offered by the outer tracker is about 13-38  $\mu\text{m}$  in the  $r\phi$  position  
1185 measurement. The inner four TEC disks use silicon sensors 320  $\mu\text{m}$  thick; those in  
1186 the TOB and the outer three TEC disks use silicon sensors of 500  $\mu\text{m}$  thickness. The  
1187 silicon strips run parallel to the  $z$ -axis and the distance between strips varies from 80  
1188  $\mu\text{m}$  in the inner TIB layers to 183  $\mu\text{m}$  in the inner TOB layers; in the endcaps the  
1189 wedge-shaped sensors with radial strips, whose pitch range between 81  $\mu\text{m}$  at small  
1190 radii and 205  $\mu\text{m}$  at large radii.

1191

1192 The whole SST has 15148 silicon modules, 9.3 million silicon strips and cover a total  
1193 active area of about 198  $\text{m}^2$

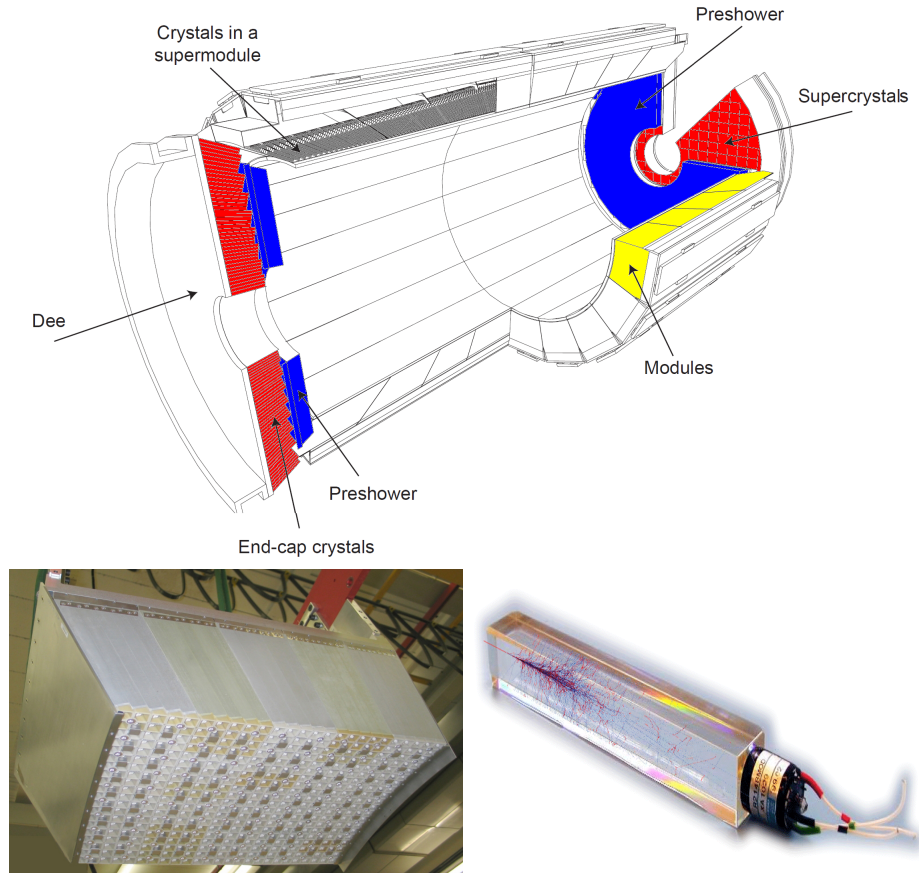


**Figure 3.13:** Top: CMS ECAL schematic view. Bottom: Module equipped with the crystals (left); ECAL crystal(right).

### 1194 3.3.4 Electromagnetic calorimeter

1195 The CMS electromagnetic calorimeter (ECAL) is designed to measure the energy of  
 1196 electrons and photons. It is composed of 75848 lead tungstate crystals which has a  
 1197 short radiation length (0.89 cm) and fast response given that 80% of the light is em-  
 1198 mited within 25 ns; however, they are combined with Avalanche photodiodes (APDs)  
 1199 as photodetectors given that crytals themself have a low light yield ( $30\gamma/\text{MeV}$ ). An  
 1200 schematic view of the ECAL is shown in figure 3.13.

1201

1202 Energy is measured by absorbing electrons and photons which generates an elec-

1203 electromagnetic “shower”, as seen in bottom right picture of the figure3.13. The ECAL  
 1204 barrel (EB) cover the region  $|\eta| < 1.479$ , using crystals of depth of 23 cm and  $2.2 \times 2.2$   
 1205  $\text{cm}^2$  transverse section.

1206 The ECAL endcap (EE) cover the region  $1.479 < |\eta| < 3.0$  using crystals of depth  
 1207 22 cm and transverse section of  $2.86 \times 2.86 \text{ cm}^2$ ; the photodetectors used are vacuum  
 1208 phototriodes (VPTs). Each EE is divided in two structures called “Dees”.

1209

1210 In front of the EE, it is installed the preshower detector (ES) which covers the region  
 1211  $1.653 < |\eta| < 2.6$ . The ES provides a precise measurement of the position of electro-  
 1212 magnetic showers, which allows to distinguish electrons and photons signals from  $\pi^0$   
 1213 decay signals. The ES is composed of a layer of lead absorber followed by a layer of  
 1214 plastic scintillators

### 1215 3.3.5 Hadronic calorimeter

1216 Hadrons are not absorbed by the ECAL but by the hadron calorimeter (HCAL),  
 1217 which is made of a combination of alternating brass absorber and silicon photo-  
 1218 multiplier(SiPM) layers; therefore, particles passing through the scintillator material  
 1219 produce showers, as in the ECAL, as a result of the inelastic scattering of the hadrons  
 1220 with the detector material. Since the particles are not absorbed in the scintillator,  
 1221 their energy is sampled; therefore the total energy is not measured but stimated,  
 1222 which reduce the resolution of the detector. Brass was choosen as the absorber mate-  
 1223 rial due to its short interaction lenght ( $\lambda_I = 16.42\text{cm}$ ) and its non-magnetivity. Figure  
 1224 3.14 shows an schematic view of the CMS HCAL.

1225

1226 The HCAL is divided in four sections; the Hadron Barrel (HB), the Hadron Outer

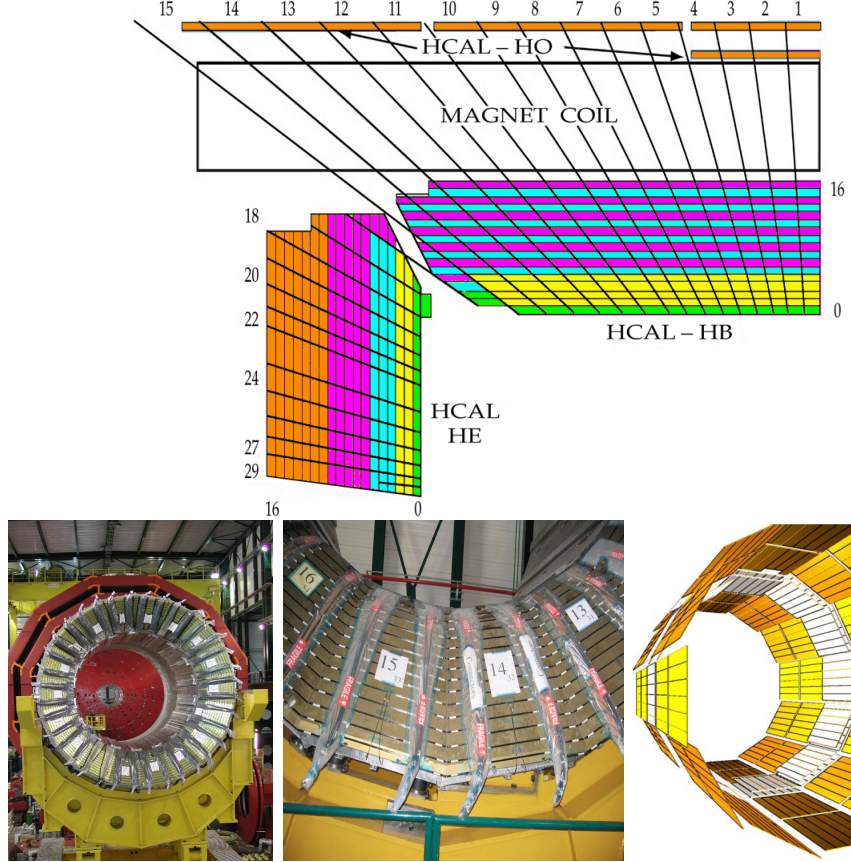


**Figure 3.14:** Top: CMS HCAL schematic view, the colors indicate the layers that are grouped into the same readout channels. Bottom: picture of a section of the HB; the absorber material is the golden region and scintillators are placed in between the absorber material (left and center). Schematic view of the HO (right). [79, 80]

1227 (HO), the Hadron Endcap (HE) and the Hadron Forward (HF) sections. The HB  
 1228 cover the region  $0 < |\eta| < 1.4$ , while the HE covers the region  $1.3 < |\eta| < 3.0$ . The HF,  
 1229 made of quartz fiber scintillator and steel as absorption material, covers the forward  
 1230 region  $3.0 < |\eta| < 5.2$ . Both the HB and HF are located inside the solenoid. The HO  
 1231 is placed outside the magnet as an additional layer of scintillators with the purpose  
 1232 of measure the energy tails of particles passing through the HB and the magnet  
 1233 (see figure 3.14 top and bottom right) . The upgrades made to the HCAL during  
 1234 the technical stop 2016-2017 consisted in the replacement of the phototransducers,

1235 improving the efficiency.

### 1236 3.3.6 Superconducting solenoid magnet

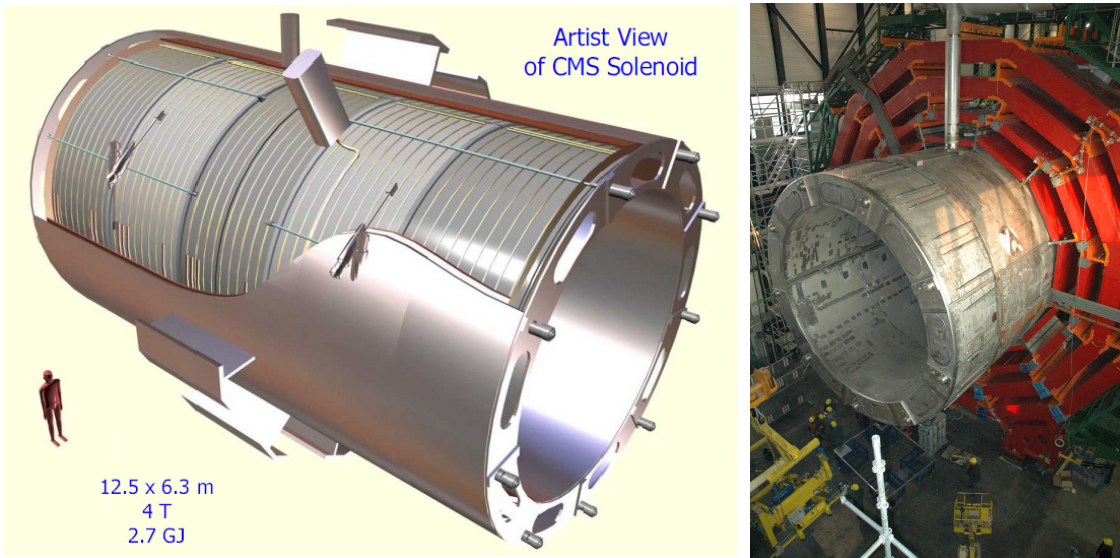


**Figure 3.15:** Artistic representation of the CMS solenoid magnet(left). The magnet is supported on an iron yoke (right) which also serves as the house of the muon detector and as mechanical support for the whole CMS detector [74].

1237 The superconducting magnet installed is the CMS detector is designed to provide an  
 1238 intense and highly uniform magnetic field in the central part of the detector. In fact,  
 1239 the tracking system takes advantage of the bending power of the magnetic field to  
 1240 measure with precision the momentum of the particles that traverse it; the unam-  
 1241 biguous determination of the sign for high momentum muons was a driven principle  
 1242 during the design of the magnet. The magnet has a diameter of 6.3 m, a length of  
 1243 12.5 m in a cold mass of 220 t; the generated magnetic field reach a strength of 3.8T.  
 1244 Since it is made of Ni-Tb superconducting cable it has to operate at a temperature  
 1245 of 4.7 K by using a helium cryogenic system; the current circulating in the cables  
 1246 reach 18800 A under normal running conditions. The left side of figure 3.15 shows  
 1247 an artistic view of the CMS magnet, while the right side shows a transverse view of

1248 the cold mass where the winding structure is visible.

1249

1250 The yoke (see figure 3.15), composed of 5 barrel wheels and 6 endcap disks made  
 1251 of iron, serves not only as the media for magnetic flux return, but also provides the  
 1252 house for the muon detector system and structural stability to the full detector.

1253 **3.3.7 Muon system**

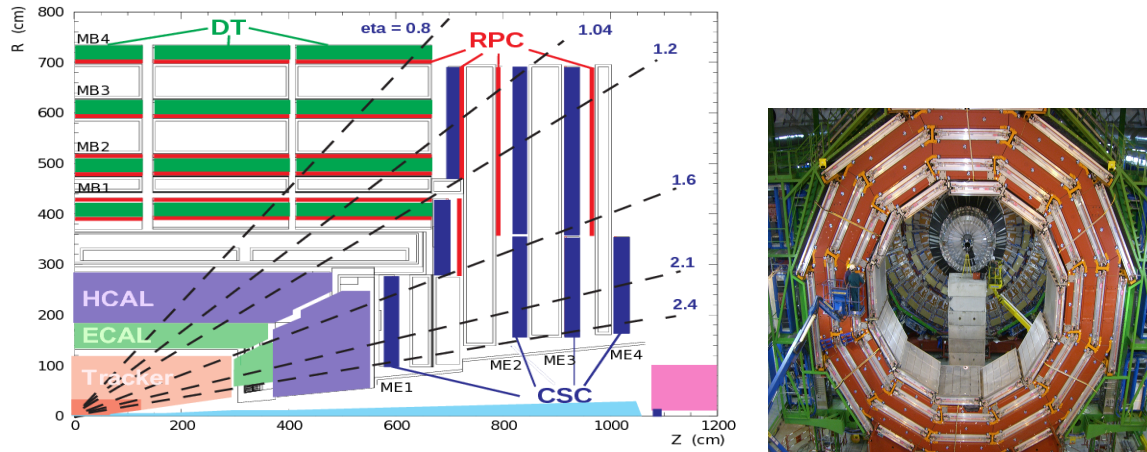


**Figure 3.16:** Left: CMS muon system schematic view; Right: one of the yoke rings with the muon DTs and RPCs installed; in the back it is possible to see the muon endcap [81].

1254 Muons are the only charged particles able pass through all the CMS detector due to  
 1255 their low ionization energy loss; thus, muons can be separated easily from the high  
 1256 amount of particles produced in a pp collision. Also, muons are expected to be pro-  
 1257 duced in the decay of several new particles; therefore, a good detection of muons was  
 1258 on the leading principles when designing the CMS detector.

1259

1260 The CMS muon detection system is embedded in the return yoke as seen in figure  
 1261 3.16. It is composed of three different detector types; the drift tube chambers (DT)  
 1262 are located in the central region  $\eta < 1.2$  arranged in four layers of drift chambers filled

1263 with an Ar/CO<sub>2</sub> gas mixture.

1264

1265 The muon endcaps are made of Cathode strip chambers (CSC) covering the region  
1266  $\eta < 2.4$  and filled with a mixture of Ar/CO<sub>2</sub>/CF<sub>4</sub>. The reason behind using a different  
1267 detector type lies on the different conditions in the forward region like the high muon  
1268 rate and high residual magnetic field.

1269

1270 The third type of detector used in the muon system is a set four disks of resistive  
1271 plate chambers (RPC) working in avalanche mode. The RPCs provide good spatial  
1272 and time resolutions. The track of  $high - p_T$  muon candidate is build combining  
1273 information from the tracking system and the signal from up to 6 RPCs and 4 DT  
1274 chambers.

### 1275 **3.3.8 trigger system - HLT- L1**

1276 The online event selection process (trigger) must reduce the huge rate to about 100  
1277 events/s for storage and subsequent analysis. The short time between bunch crossings,  
1278 25 ns, has major implications for the design of the read-out and trigger systems.

1279 Due to its high segmentation, the pixel detector not only forms high quality seeds  
1280 for the track reconstruction algorithm offline, but is also used to do fast tracking online  
1281 in the high level trigger (HLT) for primary vertex reconstruction, electron/photon  
1282 identification, muon reconstruction, tau identification and b-tagging.



1283 **3.3.9 computing model**

1284 **3.4 Event generation simulation and**  
1285 **reconstruction**

1286 **3.4.1 event generation**

1287 **3.4.2 Hard scattering**

1288 **3.4.3 parton shower**

1289 **3.4.4 hadronization and decays**

1290 **3.4.5 underlying events and pileup**

1291 **3.4.6 MC - MadEvent, MadGraph and madgraphNLO,**  
1292 **powheg, pythia, tauola**

1293 **3.4.7 detector simulation**

1294 **3.4.8 event reconstruction- particle flow algorithm,**  
1295 **vertexing , muon reco, electron reco, photon and**  
1296 **hadron reco, jets reco, anti-kt algoritm, jet energy**  
1297 **corrections, btagging, MET**

1298 **3.4.9 MVA methods, NN, BDT, boosting, overtraining,**  
1299 **variable ranking**

1300 **3.4.10 statistical inference, likelihood parametrization**

1301 **3.4.11 nuisance paraeters**

1302 **3.4.12 selection criteria**

<sup>1304</sup> **Chapter 4**

<sup>1305</sup> **Search for production of a Higgs**

<sup>1306</sup> **boson and a single top quark in**

<sup>1307</sup> **multilepton final states in pp**

<sup>1308</sup> **collisions at  $\sqrt{s} = 13$  TeV**

<sup>1309</sup> **4.1 Introduction**

<sup>1310</sup> Dont forget to mention previous constrains to ct check reference ?? and references

<sup>1311</sup> <https://link.springer.com/content/pdf/10.1007%2FJHEP01>

<sup>1312</sup> A. Azatov, R. Contino and J. Galloway,  $\rightarrow$  Model-Independent Bounds on a

<sup>1313</sup> Light Higgs, $\rightarrow$  JHEP 1204 (2012) 127 [arXiv:1202.3415 [hep-ph]].

<sup>1314</sup> J. R. Espinosa, C. Grojean, M. Muhlleitner and M. Trott,  $\rightarrow$  Fingerprinting

<sup>1315</sup> Higgs Suspects at the LHC, $\rightarrow$  JHEP 1205 (2012) 097 [arXiv:1202.3697 [hep-ph]].

<sup>1316</sup> This chapter present the search for the associated production of a Higgs boson and

<sup>1317</sup> a single top quark events with three leptons in the final state, targeting Higgs decay

1318 modes to  $WW$ ,  $ZZ$ , and  $\tau\tau$ . The analysis uses the 13 TeV dataset produced in 2016,  
 1319 corresponding to an integrated luminosity of  $35.9\text{fb}^{-1}$ . It is based on and expands  
 1320 previous analyses at 8 TeV [82, 83] and searches for associated production of  $t\bar{t}$  and  
 1321 Higgs in the same channel [84], and complements searches in other decay channels  
 1322 targeting  $H \rightarrow b\bar{b}$  [85].

1323 As showed in section 2.4, the cross section of the associated production of a Higgs  
 1324 boson and a single top quark ( $tHq$ ) process is driven by a destructive interference of  
 1325 two contributions (see Figure 4.1), where the Higgs couples to either the W boson or  
 1326 the top quark. Any deviation from the standard model (SM) in the Higgs coupling  
 1327 structure could therefore lead to a large enhancement of the cross section, making  
 1328 this analysis sensitive to such deviations. A second process, where the Higgs and  
 1329 top quark are accompanied by a W boson ( $tHW$ ) has similar behavior, albeit with a  
 1330 weaker interference pattern.

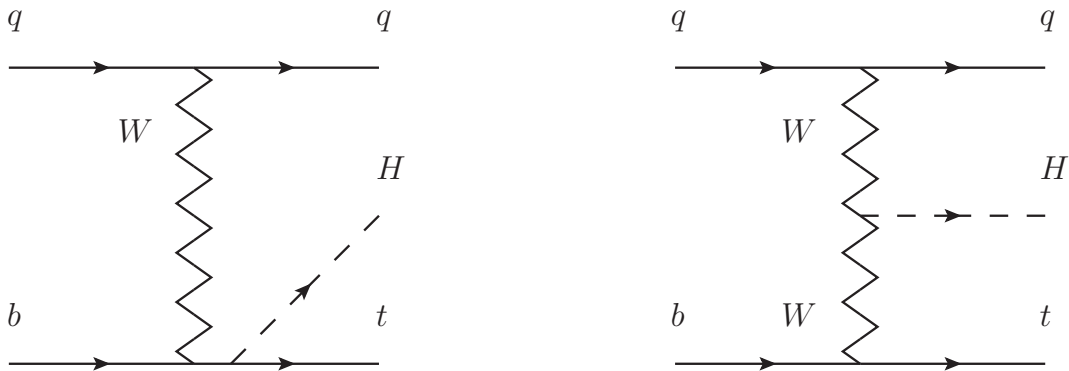


**Figure 4.1:** The two leading-order diagrams of  $tHq$  production.

1331 We selects events with three leptons and a  $b$  tagged jet in the final state. The  $tHq$   
 1332 signal contribution is then determined in a fit of the observed data to two multivariate  
 1333 classifier outputs, each trained to discriminate against one of the two dominant back-  
 1334 grounds of events with non-prompt leptons from  $t\bar{t}$  and of associated production of  $t\bar{t}$

1335 and vector bosons ( $t\bar{t}W$ ,  $t\bar{t}Z$ ). The fit result is then used to set an upper limit on the  
 1336 combined  $t\bar{t}H$ ,  $tHq$  and  $tHW$  production cross section, as a function of the relative  
 1337 coupling strengths of Higgs and top quark and Higgs and W boson, respectively.

## 1338 4.2 Data and MC Samples

1339 The data considered in this analysis were collected by the CMS experiment dur-  
 1340 ing 2016 and correspond to a total integrated luminosity of  $35.9\text{fb}^{-1}$ . Only periods  
 1341 when the CMS magnet was on were considered when selecting the data samples, that  
 1342 corresponds to the 23 Sep 2016 (Run B to G) and PromptReco (Run H) versions  
 1343 of the datasets. The MC samples used in this analysis correspond to the RunI-  
 1344 ISummer16MiniAODv2 campaign produced with CMSSW 80X. The two signal sam-  
 1345 ples (for  $tHq$  and  $tHW$ ) were produced with MG5\_aMC@NLO (version 5.222), in  
 1346 leading-order mode, and are normalized to next-to-leading-order cross sections,  
 1347 see Tab. 4.1. Each sample is generated with a set of event weights corresponding to  
 1348 different values of  $\kappa_t$  and  $\kappa_V$  couplings as shown in Tab. 4.2.

### 1349 4.2.1 Full 2016 dataset and MC samples

Sample	$\sigma$ [pb]	BF
/THQ_Hincl_13TeV-madgraph-pythia8_TuneCUETP8M1/	0.7927	0.324
/THW_Hincl_13TeV-madgraph-pythia8_TuneCUETP8M1/	0.1472	1.0

**Table 4.1:** Signal samples and their cross section and branching fraction used in this analysis. See Ref. [86] for more details.

1350 Different MC generators were used to generate the background processes. The  
 1351 dominant sources ( $t\bar{t}$ ,  $t\bar{t}W$ ,  $t\bar{t}Z$ ,  $t\bar{t}H$ ) were produced using AMC@NLO interfaced  
 1352 to PYTHIA8, and are scaled to NLO cross sections. Other processes are simulated

		<i>tHq</i>		<i>tHW</i>		
$\kappa_V$	$\kappa_t$	sum of weights	cross section [pb]	sum of weights	cross section [pb]	LHE weights
1.0	-3.0	35.700022	2.991	11.030445	0.6409	LHEweight_wgt[446]
1.0	-2.0	20.124298	1.706	5.967205	0.3458	LHEweight_wgt[447]
1.0	-1.5	14.043198	1.205	4.029093	0.2353	LHEweight_wgt[448]
1.0	-1.25	11.429338	0.9869	3.208415	0.1876	LHEweight_wgt[449]
1.0	-1.0		0.7927		0.1472	
1.0	-0.75	7.054998	0.6212	1.863811	0.1102	LHEweight_wgt[450]
1.0	-0.5	5.294518	0.4723	1.339886	0.07979	LHEweight_wgt[451]
1.0	-0.25	3.818499	0.3505	0.914880	0.05518	LHEweight_wgt[452]
1.0	0.0	2.627360	0.2482	0.588902	0.03881	LHEweight_wgt[453]
1.0	0.25	1.719841	0.1694	0.361621	0.02226	LHEweight_wgt[454]
1.0	0.5	1.097202	0.1133	0.233368	0.01444	LHEweight_wgt[455]
1.0	0.75	0.759024	0.08059	0.204034	0.01222	LHEweight_wgt[456]
1.0	1.0	0.705305	0.07096	0.273617	0.01561	LHEweight_wgt[457]
1.0	1.25	0.936047	0.0839	0.442119	0.02481	LHEweight_wgt[458]
1.0	1.5	1.451249	0.1199	0.709538	0.03935	LHEweight_wgt[459]
1.0	2.0	3.335034	0.2602	1.541132	0.08605	LHEweight_wgt[460]
1.0	3.0	10.516125	0.8210	4.391335	0.2465	LHEweight_wgt[461]
1.5	-3.0	45.281492	3.845	13.426212	0.7825	LHEweight_wgt[462]
1.5	-2.0	27.606715	2.371	7.809713	0.4574	LHEweight_wgt[463]
1.5	-1.5	20.476088	1.784	5.594971	0.3290	LHEweight_wgt[464]
1.5	-1.25	17.337465	1.518	4.635978	0.2749	LHEweight_wgt[465]
1.5	-1.0	14.483302	1.287	3.775902	0.2244	LHEweight_wgt[466]
1.5	-0.75	11.913599	1.067	3.014744	0.1799	LHEweight_wgt[467]
1.5	-0.5	9.628357	0.874	2.352505	0.1410	LHEweight_wgt[468]
1.5	-0.25	7.627574	0.702	1.789184	0.1081	LHEweight_wgt[469]
1.5	0.0	5.911882	0.5577	1.324946	0.08056	LHEweight_wgt[470]
1.5	0.25	4.479390	0.4365	0.959295	0.05893	LHEweight_wgt[471]
1.5	0.5	3.331988	0.3343	0.692727	0.04277	LHEweight_wgt[472]
1.5	0.75	2.469046	0.2558	0.525078	0.03263	LHEweight_wgt[473]
1.5	1.0	1.890565	0.2003	0.456347	0.02768	LHEweight_wgt[474]
1.5	1.25	1.596544	0.1689	0.486534	0.02864	LHEweight_wgt[475]
1.5	1.5	1.586983	0.1594	0.615638	0.03509	LHEweight_wgt[476]
1.5	2.0	2.421241	0.2105	1.170602	0.06515	LHEweight_wgt[477]
1.5	3.0	7.503280	0.5889	3.467546	0.1930	LHEweight_wgt[478]
0.5	-3.0	27.432685	2.260	8.929074	0.5136	LHEweight_wgt[479]
0.5	-2.0	13.956013	1.160	4.419093	0.2547	LHEweight_wgt[480]
0.5	-1.5	8.924438	0.7478	2.757611	0.1591	LHEweight_wgt[481]
0.5	-1.25	6.835341	0.5726	2.075247	0.1204	LHEweight_wgt[482]
0.5	-1.0	5.030704	0.4273	1.491801	0.08696	LHEweight_wgt[483]
0.5	-0.75	3.510528	0.2999	1.007273	0.05885	LHEweight_wgt[484]
0.5	-0.5	2.274811	0.1982	0.621663	0.03658	LHEweight_wgt[485]
0.5	-0.25	1.323555	0.1189	0.334972	0.01996	LHEweight_wgt[486]
0.5	0.0	0.656969	0.06223	0.147253	0.008986	LHEweight_wgt[487]
0.5	0.25	0.274423	0.02830	0.058342	0.003608	LHEweight_wgt[488]
0.5	0.5	0.176548	0.01778	0.068404	0.003902	LHEweight_wgt[489]
0.5	0.75	0.363132	0.03008	0.177385	0.009854	LHEweight_wgt[490]
0.5	1.0	0.834177	0.06550	0.385283	0.02145	LHEweight_wgt[491]
0.5	1.25	1.589682	0.1241	0.692099	0.03848	LHEweight_wgt[492]
0.5	1.5	2.629647	0.2047	1.097834	0.06136	LHEweight_wgt[493]
0.5	2.0	5.562958	0.4358	2.206057	0.1246	LHEweight_wgt[494]
0.5	3.0	14.843102	1.177	5.609519	0.3172	LHEweight_wgt[495]

**Table 4.2:**  $\kappa_V$  and  $\kappa_t$  combinations generated for the two signal samples and their NLO cross sections. The *tHq* cross section is multiplied by the branching fraction of the enforced leptonic decay of the top quark (0.324). See also Ref. [86].

Sample	$\sigma$ [pb]
TTWJetsToLNu_TuneCUETP8M1_13TeV-amcatnloFXFX-madspin-pythia8	0.2043
TTZToLLNuNu_M-10_TuneCUETP8M1_13TeV-amcatnlo-pythia8	0.2529
tthJetToNonbb_M125_13TeV_amcatnloFXFX_madspin_pythia8_mWCutfix /store/cmst3/group/susy/gpetrucc/13TeV/u/TTLL_m1to10_L0_NoMS_for76X/	0.2151 0.0283
WGToLNuG_TuneCUETP8M1_13TeV-madgraphMLM-pythia8	585.8
ZGTo2LG_TuneCUETP8M1_13TeV-amcatnloFXFX-pythia8	131.3
TGJets_TuneCUETP8M1_13TeV_amcatnlo_madspin_pythia8	2.967
TGJets_TuneCUETP8M1_13TeV_amcatnlo_madspin_pythia8	2.967
TTGJets_TuneCUETP8M1_13TeV-amcatnloFXFX-madspin-pythia8	3.697
WpWpJJ_EWK_QCD_TuneCUETP8M1_13TeV-madgraph-pythia8	0.03711
ZZZ_TuneCUETP8M1_13TeV-amcatnlo-pythia8	0.01398
WWZ_TuneCUETP8M1_13TeV-amcatnlo-pythia8	0.1651
WZZ_TuneCUETP8M1_13TeV-amcatnlo-pythia8	0.05565
WW_DoubleScattering_13TeV-pythia8	1.64
tZq_ll_4f_13TeV-amcatnlo-pythia8_TuneCUETP8M1	0.0758
ST_tWll_5f_LO_13TeV-MadGraph-pythia8	0.01123
TTTT_TuneCUETP8M1_13TeV-amcatnlo-pythia8	0.009103
WZTo3LNu_TuneCUETP8M1_13TeV-powheg-pythia8	4.4296
ZZTo4L_13TeV_powheg_pythia8	1.256
TTJets_SingleLeptFromTbar_TuneCUETP8M1_13TeV-madgraphMLM-pythia8	182.1754
TTJets_SingleLeptFromT_TuneCUETP8M1_13TeV-madgraphMLM-pythia8	182.1754
TTJets_DiLept_TuneCUETP8M1_13TeV-madgraphMLM-pythia8	87.3
DYJetsToLL_M-10to50_TuneCUETP8M1_13TeV-amcatnloFXFX-pythia8	18610
DYJetsToLL_M-50_TuneCUETP8M1_13TeV-madgraphMLM-pythia8	6024
WJetsToLNu_TuneCUETP8M1_13TeV-amcatnloFXFX-pythia8	61526.7
ST_tW_top_5f_inclusiveDecays_13TeV-powheg-pythia8_TuneCUETP8M1	35.6
ST_tW_antitop_5f_inclusiveDecays_13TeV-powheg-pythia8_TuneCUETP8M1	35.6
ST_t-channel_4f_leptonDecays_13TeV-amcatnlo-pythia8_TuneCUETP8M1	70.3144
ST_t-channel_antitop_4f_leptonDecays_13TeV-powheg-pythia8_TuneCUETP8M1	26.2278
ST_s-channel_4f_leptonDecays_13TeV-amcatnlo-pythia8_TuneCUETP8M1	3.68064
WWTo2L2Nu_13TeV-powheg	10.481

**Table 4.3:** List of background samples used in this analysis (CMSSW 80X). In the first section of the table are listed the samples of the processes for which we use the simulation to extract the final yields and shapes, in the second section the samples of the processes we will estimate from data. The MC simulation is used to design the data driven methods and derive the associated systematics.

Sample	$\sigma$ [pb]
ttWJets_13TeV_madgraphMLM	0.6105
ttZJets_13TeV_madgraphMLM	0.5297/0.692

**Table 4.4:** Leading-order  $t\bar{t}W$  and  $t\bar{t}Z$  samples used in the signal BDT training.

1353 using POWHEG interfaced to PYTHIA, or bare PYTHIA (see table 4.3 and [84]  
1354 for more details).

Three lepton and Four lepton
HLT_DiMu9_Ele9_CaloIdL_TrackIdL_v*
HLT_Mu8_DiEle12_CaloIdL_TrackIdL_v*
HLT_TripleMu_12_10_5_v*
HLT_Ele16_Ele12_Ele8_CaloIdL_TrackIdL_v*
HLT_Mu23_TrkIsoVVL_Ele8_CaloIdL_TrackIdL_IsoVL_v*
HLT_Mu23_TrkIsoVVL_Ele8_CaloIdL_TrackIdL_IsoVL_DZ_v*
HLT_Mu8_TrkIsoVVL_Ele23_CaloIdL_TrackIdL_IsoVL_v*
HLT_Mu8_TrkIsoVVL_Ele23_CaloIdL_TrackIdL_IsoVL_DZ_v*
HLT_Ele23_Ele12_CaloIdL_TrackIdL_IsoVL_DZ_v*
HLT_Mu17_TrkIsoVVL_Mu8_TrkIsoVVL_DZ_v*
HLT_Mu17_TrkIsoVVL_TkMu8_TrkIsoVVL_DZ_v*
HLT_IsoMu22_v*
HLT_IsoTkMu22_v*
HLT_IsoMu22_eta2p1_v*
HLT_IsoTkMu22_eta2p1_v*
HLT_IsoMu24_v*
HLT_IsoTkMu24_v*
HLT_Ele27_WPTight_Gsf_v*
HLT_Ele25_eta2p1_WPTight_Gsf_v*
HLT_Ele27_eta2p1_WPLoose_Gsf_v*

**Table 4.5:** Table of high-level triggers that we consider in the analysis.

### 1355 4.2.2 Triggers

1356 We consider online-reconstructed events triggered by one, two, or three leptons.  
 1357 Single-lepton triggers are included to boost the acceptance of events where the  $p_T$  of  
 1358 the sub-leading lepton falls below the threshold of the double-lepton triggers. Ad-  
 1359 ditionally, by including double-lepton triggers in the  $\geq 3$  lepton category, as well  
 1360 as single-lepton triggers in all categories, we increase the efficiency, considering the  
 1361 logical “or” of the trigger decisions of all the individual triggers in a given category.  
 1362 Tab. 4.5 shows the lowest-threshold non-prescaled triggers present in the High-Level  
 1363 Trigger (HLT) menus for both Monte-Carlo and data in 2016.

#### 1364 4.2.2.1 Trigger efficiency scale factors

1365 The efficiency of events to pass the trigger is measured in simulation (trivially using  
 1366 generator information) and in the data (using event collected by an uncorrelated

Category	Scale Factor
ee	$1.01 \pm 0.02$
e $\mu$	$1.01 \pm 0.01$
$\mu\mu$	$1.00 \pm 0.01$
3l	$1.00 \pm 0.03$

**Table 4.6:** Trigger efficiency scale factors and associated uncertainties, shown here rounded to the nearest percent.

1367 MET trigger). Small differences between the data and MC efficiencies are corrected  
 1368 by applying scale factors as shown in Tab. 4.6. The exact procedure and control plots  
 1369 are documented in [87] for the current analysis.

## 1370 4.3 Object Identification and event selection

### 1371 4.3.1 Jets and $b$ tagging

1372 The analysis uses anti- $k_t$  (0.4) particle-flow (PF) jets, corrected for charged hadrons  
 1373 not coming from the primary vertex (charged hadron subtraction), and having jet  
 1374 energy corrections (`Summer16_23Sep2016V3`) applied as a function of the jet  $E_T$  and  
 1375  $\eta$ . Jets are only considered if they have a transverse energy above 25GeV.

1376 In addition, they are required to be separated from any lepton candidates passing  
 1377 the fakeable object selections (see Tables 4.7 and 4.8) by  $\Delta R > 0.4$ .

1378 The loose and medium working points of the CSV b-tagging algorithm are used to  
 1379 identify  $b$  jets. Data/simulation differences in the  $b$  tagging performance are corrected  
 1380 by applying per-jet weights to the simulation, dependent on the jet  $p_T$ , eta,  $b$  tagging  
 1381 discriminator, and flavor (from simulation truth) [88]. The per-event weight is taken  
 1382 as the product of the per-jet weights, including those of the jets associated to the  
 1383 leptons. More details can be found in the corresponding  $t\bar{t}H$  documentation [84, 87].

1384 **4.3.2 Lepton selection**

Cut	Loose	Fakeable object	Tight
$ \eta  < 2.4$	✓	✓	✓
$p_T$	$> 5\text{GeV}$	$> 15\text{GeV}$	$> 15\text{GeV}$
$ d_{xy}  < 0.05 \text{ (cm)}$	✓	✓	✓
$ d_z  < 0.1 \text{ (cm)}$	✓	✓	✓
$\text{SIP}_{3D} < 8$	✓	✓	✓
$I_{\text{mini}} < 0.4$	✓	✓	✓
is Loose Muon	✓	✓	✓
jet CSV	—	$< 0.8484$	$< 0.8484$
is Medium Muon	—	—	✓
tight-charge	—	—	✓
lepMVA $> 0.90$	—	—	✓

**Table 4.7:** Requirements on each of the three muon selections. In the cases where the cut values change between the selections, those values are listed in the table. Otherwise, whether the cut is applied is indicated. For the two  $p_T^{\text{ratio}}$  and CSV rows, the cuts marked with a † are applied to leptons that fail the lepton MVA cut, while the loose cut value is applied to those that pass the lepton MVA cut.

1385 The lepton reconstruction and selection is identical to that used in the  $t\bar{t}H$  mul-  
 1386 tilepton analysis, as documented in Refs. [84, 87]. For details on the reconstruction  
 1387 algorithms, isolation, pileup mitigation, and a description of the lepton MVA discrim-  
 1388 inator and validation plots thereof, we refer to that document since they are out of  
 1389 the scope of this thesis. Three different selections are defined both for the electron  
 1390 and muon object identification: the *Loose*, *Fakeable Object*, and *Tight* selection. As  
 1391 described in more detail later, these are used for event level vetoes, the fake rate  
 1392 estimation application region, and the final signal selection, respectively. The  $p_T$  of  
 1393 fakeable objects is defined as  $0.85 \times p_T(\text{jet})$ , where the jet is the one associated to the  
 1394 lepton object. This mitigates the dependence of the fake rate on the momentum of  
 1395 the fakeable object and thereby improves the precision of the method.

1396 Tables 4.7 and 4.8 list the full criteria for the different selections of muons and  
 1397 electrons.

Cut	Loose	Fakeable Object	Tight
$ \eta  < 2.5$	✓	✓	✓
$p_T$	$> 7\text{GeV}$	$> 15\text{GeV}$	$> 15\text{GeV}$
$ d_{xy}  < 0.05 \text{ (cm)}$	✓	✓	✓
$ d_z  < 0.1 \text{ (cm)}$	✓	✓	✓
$\text{SIP}_{3D} < 8$	✓	✓	✓
$I_{\text{mini}} < 0.4$	✓	✓	✓
MVA ID $> (0.0, 0.0, 0.7)$	✓	✓	✓
$\sigma_{in\eta} < (0.011, 0.011, 0.030)$	—	✓	✓
$\text{H/E} < (0.10, 0.10, 0.07)$	—	✓	✓
$\Delta\eta_{in} < (0.01, 0.01, 0.008)$	—	✓	✓
$\Delta\phi_{in} < (0.04, 0.04, 0.07)$	—	✓	✓
$-0.05 < 1/E - 1/p < (0.010, 0.010, 0.005)$	—	✓	✓
$p_T^{\text{ratio}}$	—	$> 0.5^\dagger / -$	—
jet CSV	—	$< 0.3^\dagger / < 0.8484$	$< 0.8484$
tight-charge	—	—	✓
conversion rejection	—	—	✓
Number of missing hits	$< 2$	$== 0$	$== 0$
lepMVA $> 0.90$	—	—	✓

**Table 4.8:** Criteria for each of the three electron selections. In cases where the cut values change between selections, those values are listed in the table. Otherwise, whether the cut is applied is indicated. In some cases, the cut values change for different  $\eta$  ranges. These ranges are  $0 < |\eta| < 0.8$ ,  $0.8 < |\eta| < 1.479$ , and  $1.479 < |\eta| < 2.5$  and the respective cut values are given in the form (value<sub>1</sub>, value<sub>2</sub>, value<sub>3</sub>).

### 1398 4.3.3 Lepton selection efficiency

1399 Efficiencies of reconstruction and selecting loose leptons are measured both for muons  
 1400 and electrons using a tag and probe method on both data and MC, using  $Z \rightarrow \ell^+ \ell^-$ .  
 1401 Corresponding scale factors are derived from the ratio of efficiencies and applied to the  
 1402 selected These. Events are produced for the leptonic SUSY analyses using equivalent  
 1403 lepton selections and recycled for the  $t\bar{t}H$  analysis as well as for this analysis. The  
 1404 efficiencies of applying the tight selection as defined in Tables 4.7 and 4.8, on the  
 1405 loose leptons are determined again by using a tag and probe method on a sample of  
 1406 DY-enriched events. They are documented for the  $t\bar{t}H$  analysis in Ref. [87] and are  
 1407 exactly equivalent for this analysis.

## 1408 4.4 Background predictions

1409 The modeling of reducible and irreducible backgrounds in this analysis uses the exact  
 1410 methods, analysis code, and ROOT trees used for the  $t\bar{t}H$  multilepton analysis. We  
 1411 give a brief description of the methods and refer to the documentation of that analysis  
 1412 in Refs. [84, 87] for any details.

1413 The backgrounds in three-lepton final states can be split in two broad categories:  
 1414 irreducible backgrounds with genuine prompt leptons (i.e. from on-shell W and Z  
 1415 boson decays); and reducible backgrounds where at least one of the leptons is “non-  
 1416 prompt”, i.e. produced within a hadronic jet, either a genuine lepton from heavy  
 1417 flavor decays, or simply mis-reconstructed jets.

1418 Irreducible backgrounds can be reliably estimated directly from Monte-Carlo sim-  
 1419 ulated events, using higher-order cross sections or data control regions for the overall  
 1420 normalization. This is done in this analysis for all backgrounds involving prompt lep-  
 1421 tons:  $t\bar{t}W$ ,  $t\bar{t}Z$ ,  $t\bar{t}H$ ,  $WZ$ ,  $ZZ$ ,  $W^\pm W^\pm qq$ ,  $t\bar{t}t\bar{t}$ ,  $tZq$ ,  $tZW$ ,  $WWW$ ,  $WWZ$ ,  $WZZ$ ,  
 1422  $ZZZ$ .

1423 Reducible backgrounds, on the other hand, are not well predicted by simulation,  
 1424 and are estimated using data-driven methods. In the case of non-prompt leptons, a  
 1425 fake rate method is used, where the contribution to the final selection is estimated by  
 1426 extrapolating from a sideband (or “application region”) with a looser lepton definition  
 1427 (the fakeable object definitions in Tabs. 4.7 and 4.8) to the signal selection. The tight-  
 1428 to-loose ratios (or “fake rates”) are measured in several background dominated data  
 1429 events with dedicated triggers, subtracting the residual prompt lepton contribution  
 1430 using MC. Non-prompt leptons in our signal regions are predominantly produced in  $t\bar{t}$   
 1431 events, with a much smaller contribution, from Drell–Yan production. The systematic  
 1432 uncertainty on the normalization of the non-prompt background estimation is on the

order of 50%, and thereby one of the dominant limitations on the performance of multilepton analyses in general and this analysis in particular. It consists of several individual sources, such as the result of closure tests of the method using simulated events, limited statistics in the data control regions due to necessary prescaling of lepton triggers, and the uncertainty in the subtraction of residual prompt leptons from the control region.

The fake background where the leptons pass the looser selection are weighted according to how many of them fail the tight criteria. Events with a single failing lepton are weighted with the factor  $f/(1-f)$  for the estimate to the tight selection region, where  $f$  is the fake rate. Events with two failing leptons are given the negative weight  $-f_i f_j / (1-f_i)(1-f_j)$ , and for three leptons the weight is positive and equal to the product of  $f/(1-f)$  factor evaluated for each failing lepton.

Figures 4.2 show the distributions of some relevant kinematic variables, normalized to the cross section of the respective processes and to the integrated luminosity.

## 4.5 Signal discrimination

The  $tHq$  signal is separated from the main backgrounds using a boosted decision tree (BDT) classifier, trained on simulated signal and background events. A set of discriminating variables are given as input to the BDT which produces a output distribution maximizing the discrimination power. Table 4.9 lists the input variables used while Figures 4.3 show their distributions for the relevant signal and background samples, for the three lepton channel. Two BDT classifiers are trained for the two main backgrounds expected in the analysis: events with prompt leptons from  $t\bar{t}W$  and  $t\bar{t}Z$ (also referred to as  $t\bar{t}V$ ), and events with non-prompt leptons from  $t\bar{t}$ . The datasets used in the training are the  $tHq$  signal (see Tab. 4.1), and LO MADGRAPH samples

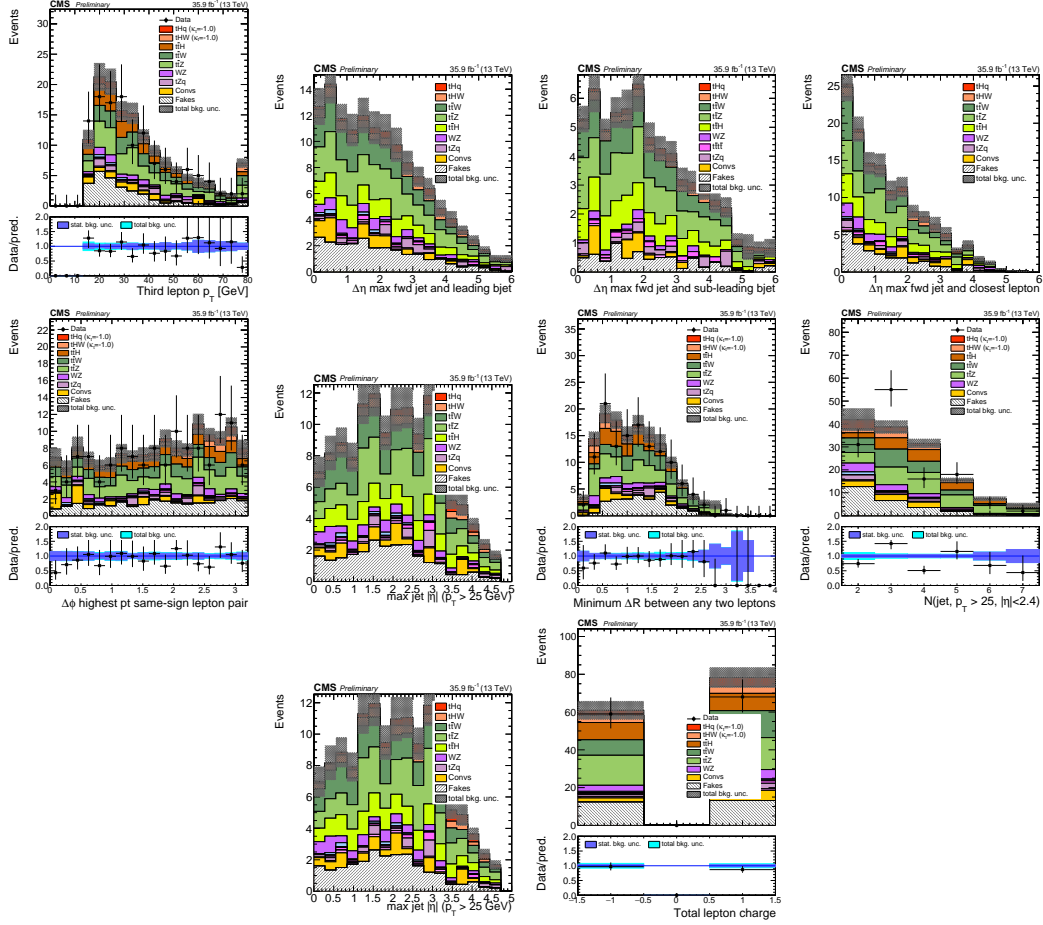


**Figure 4.2:** Distributions of input variables to the BDT for signal discrimination, three lepton channel, normalized to their cross section and to  $35.9\text{fb}^{-1}$ .

of  $t\bar{t}W$  and  $t\bar{t}Z$ , in an admixture proportional to their respective cross sections (see Tab. 4.4).

The MVA analysis consist of two stages: first a “training” where the MVA method is trained to discriminate between simulated signal and background events, then a “test” stage where the trained algorithm is used to classify different events from the samples. The sample is obtained from a pre-selection (see Tab. ?? with pre-selection cuts). Figures 4.4 show the input variables distributions as seen by the MVA algorithm. Note that in contrast to the distributions in Fig. 4.3 only the main backgrounds ( $t\bar{t}$  from simulation,  $t\bar{t}V$ ) are included.

Variable name	Description
nJet25	Number of jets with $p_T > 25$ GeV, $ \eta  < 2.4$
MaxEtaJet25	Maximum $ \eta $ of any (non-CSV-loose) jet with $p_T > 25$ GeV
totCharge	Sum of lepton charges
nJetEta1	Number of jets with $ \eta  > 1.0$ , non-CSV-loose
detaFwdJetBJet	$\Delta\eta$ between forward light jet and hardest CSV loose jet
detaFwdJet2BJet	$\Delta\eta$ between forward light jet and second hardest CSV loose jet (defaults to -1 in events with only one CSV loose jet)
detaFwdJetClosestLep	$\Delta\eta$ between forward light jet and closest lepton
dphiHighestPtSSPair	$\Delta\phi$ of highest $p_T$ same-sign lepton pair
minDRll	minimum $\Delta R$ between any two leptons
Lep3Pt/Lep2Pt	$p_T$ of the 3 <sup>rd</sup> lepton (2 <sup>nd</sup> for ss2l)

**Table 4.9:** MVA input discriminating variables

1466 Note that splitting the training in two groups reveals that some variables show  
 1467 opposite behavior for the two background sources; potentially screening the discrimi-  
 1468 nation power if they were to be used in a single discriminant. For some other variables  
 1469 the distributions are similar in both background cases.

1470 From table 4.9, it is clear that the input variables are correlated to some extend.  
 1471 These correlations play an important role for some MVA methods like the Fisher  
 1472 discriminant method in which the first step consist of performing a linear transfor-  
 1473 mation to an phase space where the correlations between variables are removed. In  
 1474 case a boosted decision tree (BDT) method however, correlations do not affect the  
 1475 performance. Figure 4.6 show the linear correlation coefficients for signal and back-  
 1476 ground for the two training cases (the signal values are identical by construction). As  
 1477 expected, strong correlations appears for variables related to the forward jet activity.  
 1478 Same trend is seen in case of the same sign dilepton channel in Figure ??.

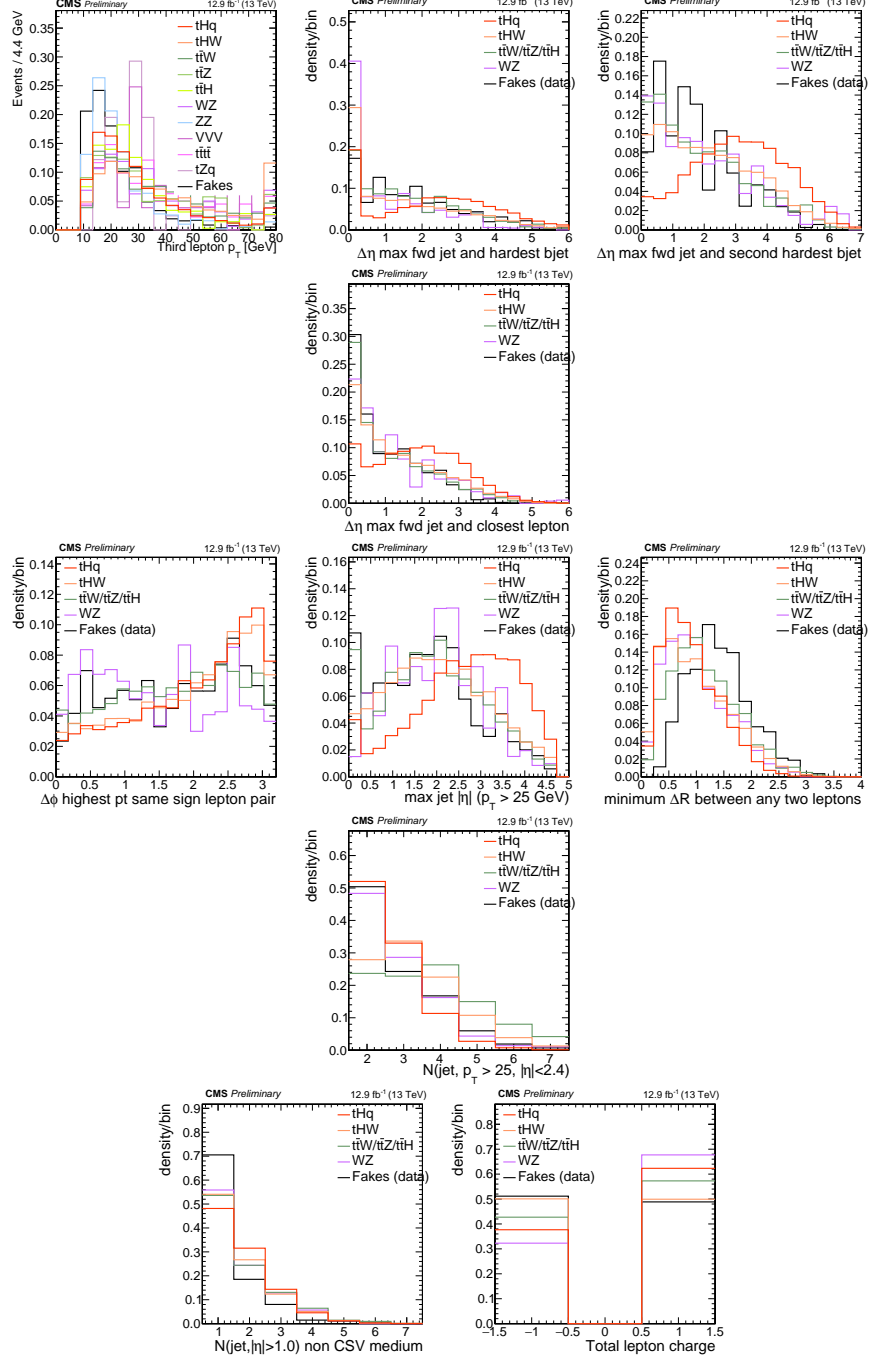


**Figure 4.3:** Distributions of input variables to the BDT for signal discrimination, three lepton channel.

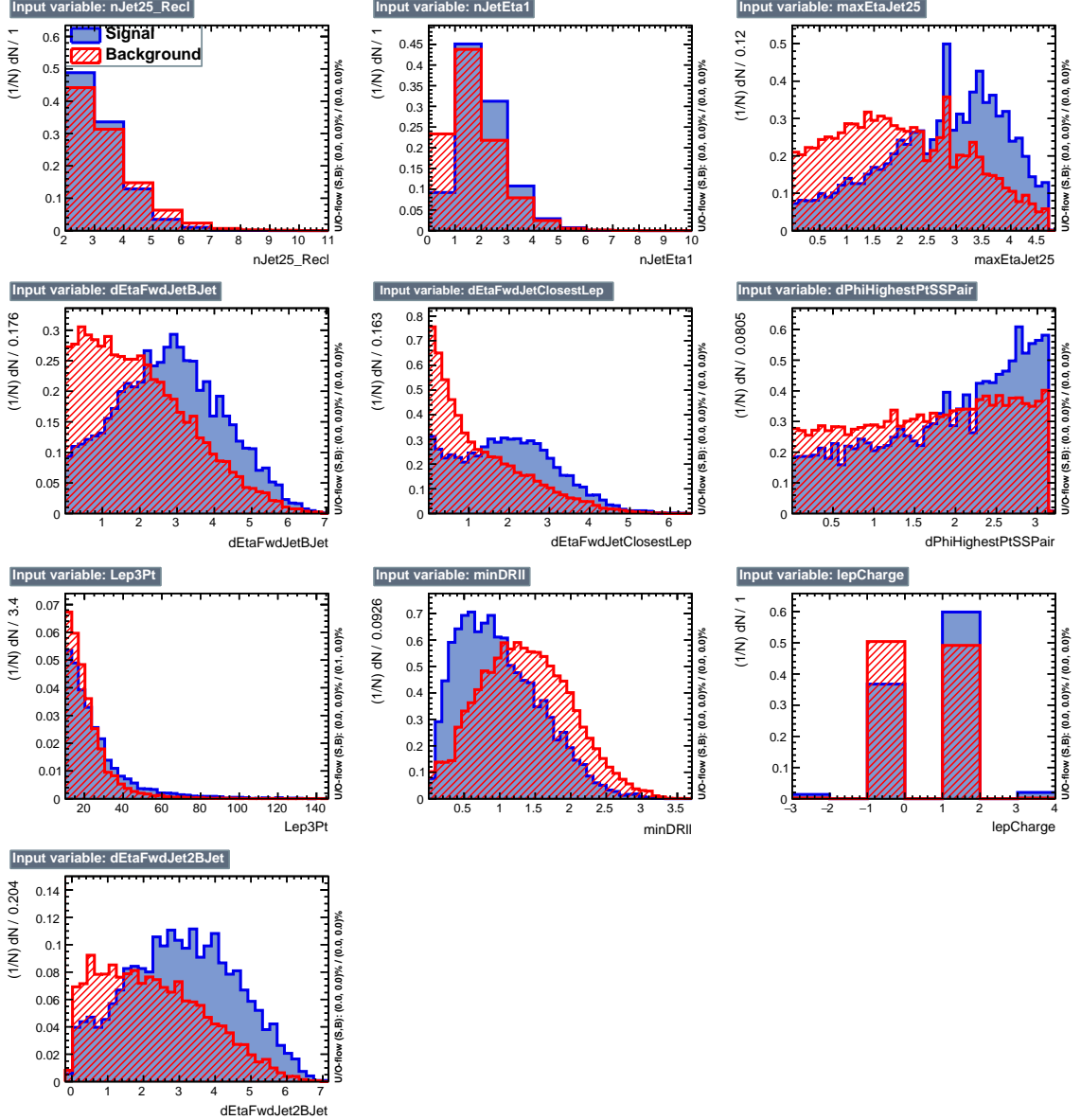


**Figure 4.4:** BDT inputs as seen by TMVA (signal, in blue, is  $tHq$ , background, in red, is  $t\bar{t}$ ) for the three lepton channel, discriminated against  $t\bar{t}$  (fakes) background.

### 1479 4.5.1 Classifiers response

1480 Several MVA algorithms were evaluated to determine the most appropriate method  
 1481 for this analysis. The plots in Fig. 4.7 (top) show the background rejection as a  
 1482 function of the signal efficiency for  $t\bar{t}$  and  $t\bar{t}V$  trainings (ROC curves) for the different

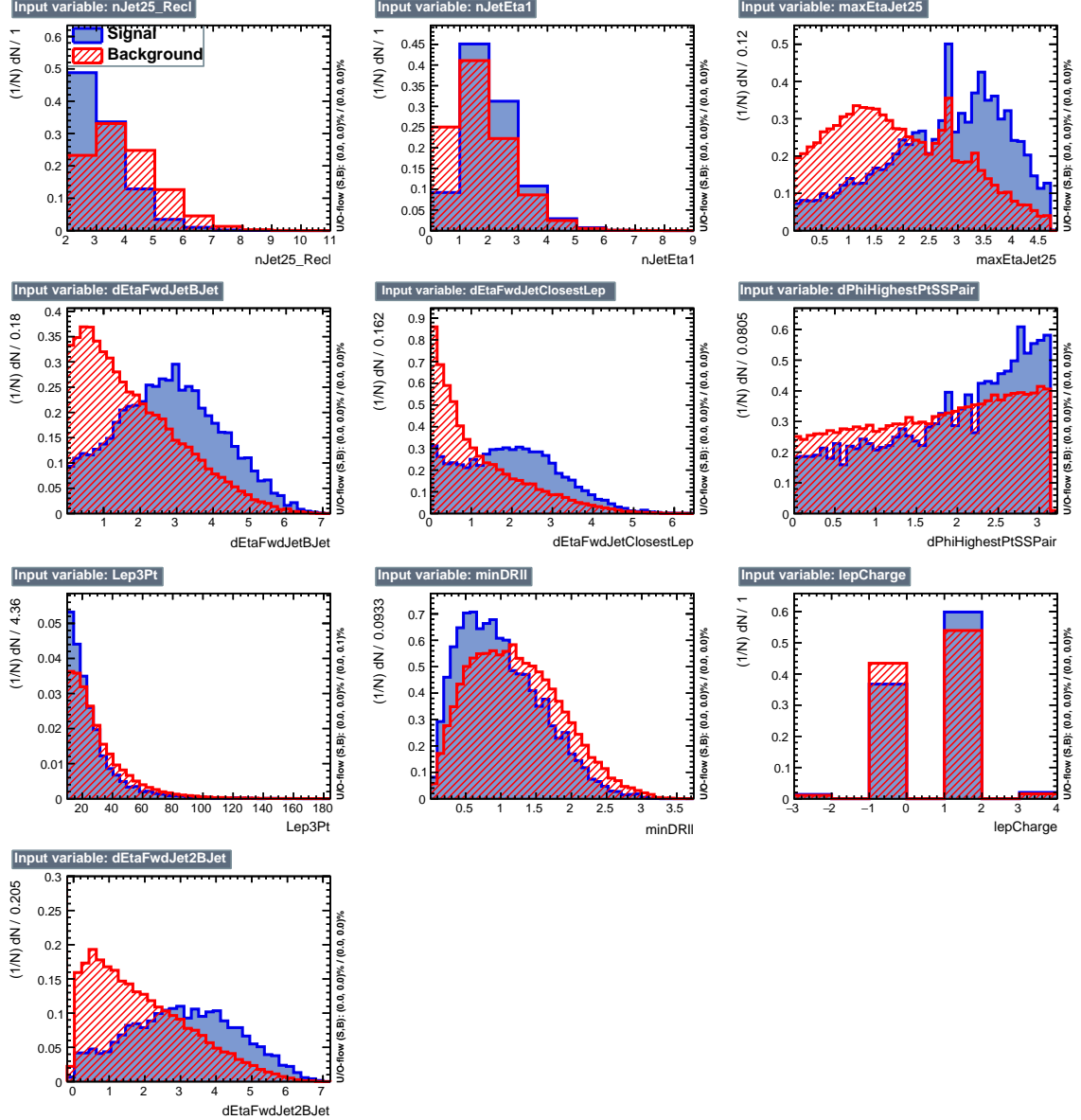


**Figure 4.5:** BDT inputs as seen by TMVA (signal, in blue, is  $tHq$ , background, in red, is  $t\bar{t}W+t\bar{t}Z$ ) for the three lepton channel, discriminated against  $t\bar{t}V$  background.

algorithms that were evaluated.

In both cases the gradient boosted decision tree (“BDTA\_GRAD”) classifier offers the best results, followed by an adaptive BDT classifier (“BDTA”). The BDTA\_GRAD classifier output distributions for signal and backgrounds are shown on the bottom of Fig. 4.7. As expected, a good discrimination power is obtained using default discrim-

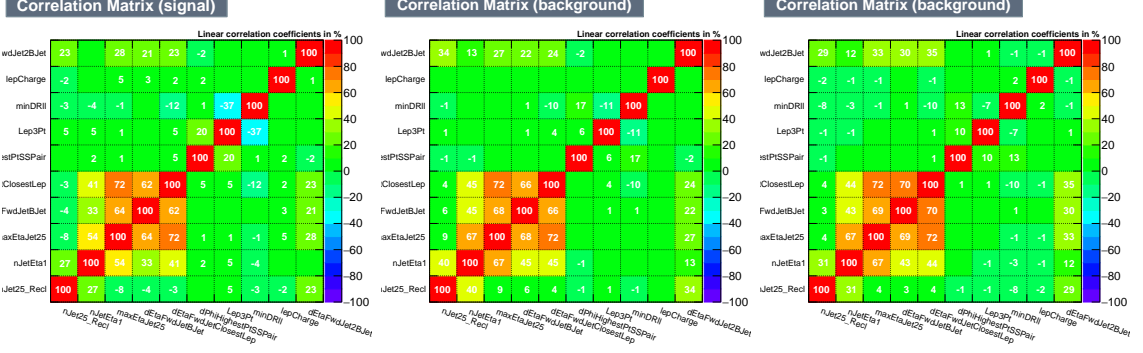


**Figure 4.6:** Signal (left),  $t\bar{t}$  background (middle), and  $t\bar{t}V$  background (right.) correlation matrices for the input variables in the TMVA analysis for the three lepton channel.

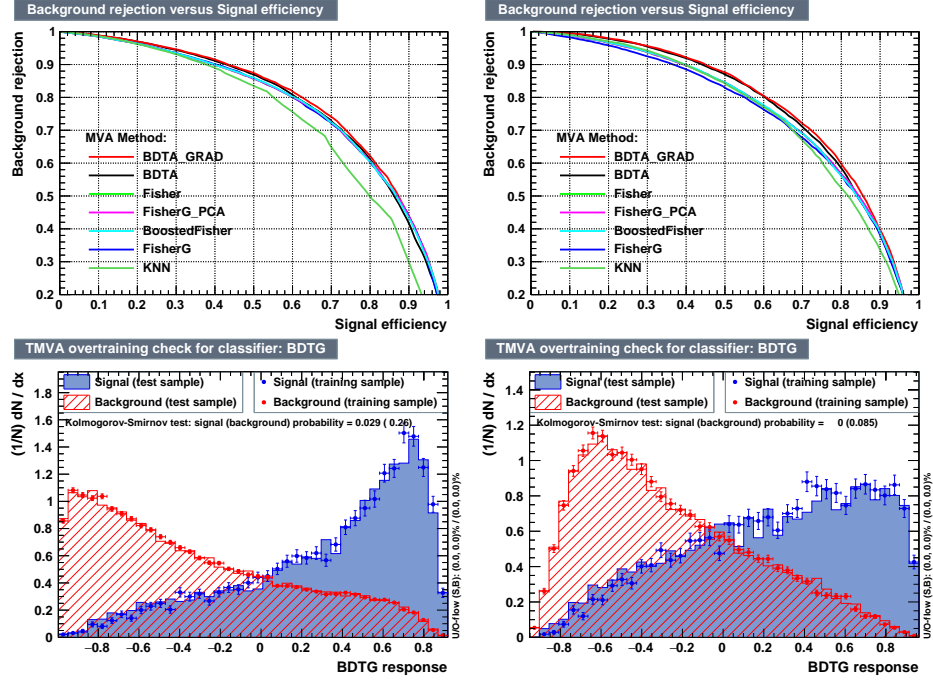


**Figure 4.7:** Top: background rejection vs signal efficiency (ROC curves) for various MVA classifiers (top) in the three lepton channel against  $t\bar{t}V$  (left) and  $t\bar{t}$  (right). Bottom: classifier output distributions for the gradient boosted decision trees, for training against  $t\bar{t}V$  (left) and against  $t\bar{t}$  (right).

inatory parameter values, with minimal overtraining. TMVA provides a ranking of the  
1488 input variables by their importance in the classification process, shown in Tab. 4.10.  
1489  
1490 The TMVA settings used in the BDT training are shown in Tab. 4.11.

ttbar training			ttV training		
Rank	Variable	Importance	Variable	Importance	
1	minDRll	1.329e-01	dEtaFwdJetBJet	1.264e-01	
2	dEtaFwdJetClosestLep	1.294e-01	Lep3Pt	1.224e-01	
3	dEtaFwdJetBJet	1.209e-01	maxEtaJet25	1.221e-01	
4	dPhiHighestPtSSPair	1.192e-01	dEtaFwdJet2BJet	1.204e-01	
5	Lep3Pt	1.158e-01	dEtaFwdJetClosestLep	1.177e-01	
6	maxEtaJet25	1.121e-01	minDRll	1.143e-01	
7	dEtaFwdJet2BJet	9.363e-02	dPhiHighestPtSSPair	9.777e-02	
8	nJetEta1	6.730e-02	nJet25_Recl	9.034e-02	
9	nJet25_Recl	6.178e-02	nJetEta1	4.749e-02	
10	lepCharge	4.701e-02	lepCharge	4.116e-02	

**Table 4.10:** TMVA input variables ranking for BDTA\_GRAD method for the trainings in the three lepton channel. For both trainings the rankings show almost the same 5 variables in the first places.

---

```

TMVA.Types.kBDT
NTrees=800
BoostType=Grad
Shrinkage=0.10
!UseBaggedGrad
nCuts=50
MaxDepth=3
NegWeightTreatment=PairNegWeightsGlobal
CreateMVAPdfs

```

---

**Table 4.11:** TMVA configuration used in the BDT training.

## 1491 4.6 Additional discriminating variables

1492 Two additional discriminating variables were tested considering the fact that the  
 1493 forward jet in the background could come from the pileup; since we have a real  
 1494 forward jet in the signal, it could give some improvement in the discriminating power.  
 1495 The additional variables describe the forward jet momentum (fwdJetPt25) and the  
 1496 forward jet identification(fwdJetPUID). Distributions for these variables in the three  
 1497 lepton channel are shown in the figure 4.8. The forward jet identification distribution  
 1498 show that for both, signal and background, jets are mostly real jets.

1499 The testing was made including in the MVA input one variable at a time, so we

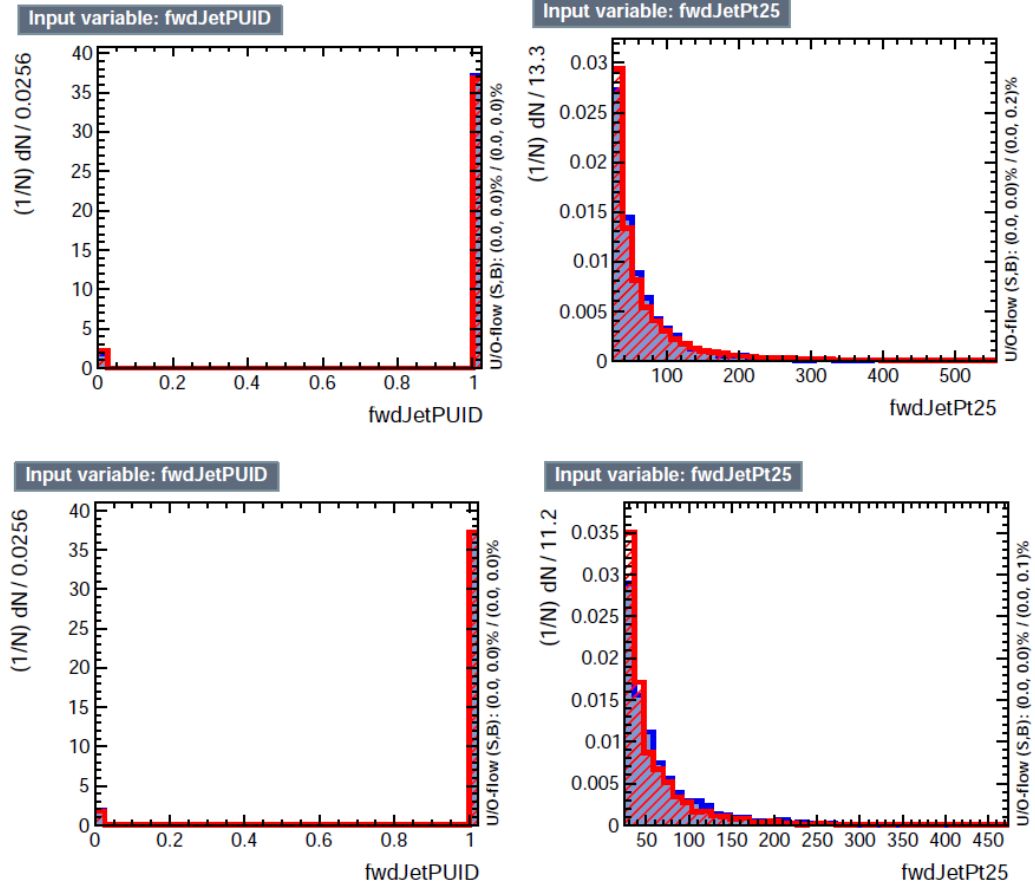


**Figure 4.8:** Additional discriminating variables distributions for ttV training (Top row) and tt training (bottom row) in the three lepton channel. The origin of the jets in the forward jet identification distribution is tagged as 0 for “pileup jets” while “real jets” are tagged as 1.

1500 can evaluate the discrimination power of each variable, and then both simultaneously.  
 1501 fwdJetPUID was ranked in the last place in importance (11) in both training (ttV  
 1502 and tt) while fwdJetPt25 was ranked 3 in the ttV training and 7 in the tt training.  
 1503 When training using 12 variables, fwdJetPt25 was ranked 5 and 7 in the ttV and tt  
 1504 trainings respectively, while fwdJetPUID was ranked 12 in both cases.

1505 The improvement in the discrimination performance provided by the additional  
 1506 variables is about 1%, so it was decided not to include them in the procedure. Table  
 1507 4.12 show the ROC-integral for all the testing cases we made.

ROC-integral	
base 10 var ttv	0.848
+ fwdJetPUID ttv	0.849
+ fwdJetPt25 ttv	0.856
12 var ttv	0.856
<hr/>	
base 10 var tt	0.777
+ fwdJetPUID tt	0.777
+ fwdJetPt25 tt	0.787
12 var	0.787

**Table 4.12:** ROC-integral for all the testing cases we made in the evaluation of the additional variables discriminating power. The improvement in the discrimination performance provided by the additional variables is about 1%

<sub>1508</sub> **Chapter 5**

<sub>1509</sub> **The CMS forward pixel detector**

<sub>1510</sub> **5.0.1 The phase 1 FPix upgrade**

<sub>1511</sub> **5.0.2 FPix module production line**

<sub>1512</sub> **5.0.3 The Gluing stage**

<sub>1513</sub> **5.0.4 The Encapsulation stage**

<sub>1514</sub> **5.0.5 The FPix module production yields**

1515 **References**

- 1516 [1] D.J. Griffiths, “Introduction to electrodynamics”. 4th ed. Pearson, (2013).
- 1517 [2] F. Mandl, G. Shaw. “Quantum field theory.” Chichester: Wiley (2009).
- 1518 [3] F. Halzen, and A.D. Martin, “Quarks and leptons: An introductory course in  
1519 modern particle physics”. New York: Wiley, (1984) .
- 1520 [4] J.C. Maxwell. “A dynamical theory of the electromagnetic field”. Philosophical  
1521 Transactions of the Royal Society of London. 155: 459–512.(1865)  
1522 doi:10.1098/rstl.1865.0008
- 1523 [5] M. Planck. “Über das Gesetz der Energieverteilung im Normalspektrum”.  
1524 Annalen der Physik. 4 (3): 553.(1901).
- 1525 [6] A. Einstein “Über einen die Erzeugung und Verwandlung des Lichtes betref-  
1526 fenden heuristischen Gesichtspunkt”. Annalen der Physik. 17 (6): 132–148,  
1527 (1905).
- 1528 [7] A. Einstein. “Über die von der molekularkinetischen Theorie der Wärme  
1529 geforderte Bewegung von in ruhenden Flüssigkeiten suspendierten Teilchen”.  
1530 Annalen der Physik. 17 (8): 549–560, (1905).
- 1531 [8] A. Einstein. “Zur Elektrodynamik bewegter Körper”. Annalen der Physik. 17  
1532 (10): 891–921, (1905).

- 1533 [9] A. Einstein, "Ist die TrÄdgheit eines KÃürpers von seinem Energieinhalt ab-  
 1534 hÃdngig?". Annalen der Physik. 18 (13): 639â€¢641, (1905).
- 1535 [10] B. P. Abbott et al. "Observation of Gravitational Waves from a Binary Black  
 1536 Hole Merger". PRL 116, 061102 (2016).
- 1537 [11] J. Schwinger. "Quantum Electrodynamics. I. A Covariant Formulation". Phys-  
 1538 ical Review. 74 (10): 1439â€¢61, (1948).
- 1539 [12] R. P. Feynman. "Spaceâ€¢Time Approach to Quantum Electrodynamics".  
 1540 Physical Review. 76 (6): 769â€¢89, (1949).
- 1541 [13] S. Tomonaga. "On a Relativistically Invariant Formulation of the Quantum  
 1542 Theory of Wave Fields". Progress of Theoretical Physics. 1 (2): 27â€¢42, (1946).
- 1543 [14] S.L. Glashow. "Partial symmetries of weak interactions", Nucl. Phys. 22 579-  
 1544 588, (1961).
- 1545 [15] A. Salam, J.C. Ward. "Electromagnetic and weak interactions", Physics Letters  
 1546 13 168-171, (1964).
- 1547 [16] S. Weinberg, "A model of leptons", Physical Review Letters, vol. 19, no. 21, p.  
 1548 1264, (1967).
- 1549 [17] E. Noether, "Invariante Variationsprobleme", Nachrichten von der Gesellschaft  
 1550 der Wissenschaften zu GÃüttingen, mathematisch-physikalische Klasse, vol.  
 1551 1918, pp. 235â€¢257, (1918).
- 1552 [18] File:Standard\_Model\_of\_Elementary\_Particle\_dark.svg. (2017, June 12)  
 1553 Wikimedia Commons, the free media repository. Retrieved November 27,  
 1554 2017 from <https://www.collegiate-advanced-electricity.com/single-post/2017/04/10/The-Standard-Model-of-Particle-Physics>.

- 1556 [19] M. Goldhaber, L. Grodzins, A.W. Sunyar “Helicity of Neutrinos”, Phys. Rev.  
 1557 109, 1015 (1958).
- 1558 [20] Palanque-Delabrouille N et al. “Neutrino masses and cosmology with Lyman-  
 1559 alpha forest power spectrum”, JCAP 11 011 (2015).
- 1560 [21] C. Patrignani et al. (Particle Data Group), Chin. Phys. C, 40, 100001 (2016)  
 1561 and 2017 update.
- 1562 [22] M. Gell-Mann. “A Schematic Model of Baryons and Mesons”. Physics Letters.  
 1563 8 (3): 214–215 (1964).
- 1564 [23] G. Zweig. “An SU(3) Model for Strong Interaction Symmetry and its Breaking”  
 1565 (PDF). CERN Report No.8182/TH.401 (1964).
- 1566 [24] G. Zweig. “An SU(3) Model for Strong Interaction Symmetry and its Breaking:  
 1567 II” (PDF). CERN Report No.8419/TH.412(1964).
- 1568 [25] M. Gell-Mann. “The Interpretation of the New Particles as Displaced Charged  
 1569 Multiplets”. Il Nuovo Cimento 4: 848. (1956).
- 1570 [26] T. Nakano, K. Nishijima. “Charge Independence for V-particles”. Progress of  
 1571 Theoretical Physics 10 (5): 581-582. (1953).
- 1572 [27] N. Cabibbo, “Unitary symmetry and leptonic decays” Physical Review Letters,  
 1573 vol. 10, no. 12, p. 531, (1963).
- 1574 [28] M.Kobayashi, T.Maskawa, “CP-violation in the renormalizable theory of weak  
 1575 interaction,” Progress of Theoretical Physics, vol. 49, no. 2, pp. 652-657, (1973).
- 1576 [29] File:Weak Decay (flipped).svg. (2017, June 12). Wikimedia Com-  
 1577 mons, the free media repository. Retrieved November 27, 2017

- 1578       from     `https : //commons.wikimedia.org/w/index.php?title = File :`  
 1579       `Weak_Decay_(flipped).svg&oldid = 247498592.`
- 1580 [30] Georgia Tech University. Coupling Constants for the Fundamental  
 1581 Forces(2005). Retrieved January 10, 2018, from `http://hyperphysics.phy –`  
 1582 `astr.gsu.edu/hbase/Forces/couple.html#c2`
- 1583 [31] M. Strassler. (May 31, 2013).The Strengths of the Known Forces. Retrieved  
 1584 January 10, 2018, from `https://profmattstrassler.com/articles – and –`  
 1585 `posts/particle – physics – basics/the – known – forces – of – nature/the –`  
 1586 `strength – of – the – known – forces/`
- 1587 [32] M. Peskin, D. Schroeder, “An introduction to quantum field theory”. Perseus  
 1588 Books Publishing L.L.C., (1995).
- 1589 [33] A. Pich. “The Standard Model of Electroweak Interactions”  
 1590 `https://arxiv.org/abs/1201.0537`
- 1591 [34] F.Bellaiche. (2012, 2 September). “What’s this Higgs boson anyway?”. Retrieved  
 1592 from: `https://www.quantum-bits.org/?p=233`
- 1593 [35] M. Endres et al. Nature 487, 454-458 (2012) doi:10.1038/nature11255
- 1594 [36] F. Englert, R. Brout. “Broken Symmetry and the Mass of Gauge  
 1595 Vector Mesons”. Physical Review Letters. 13 (9): 321-23.(1964)  
 1596 doi:10.1103/PhysRevLett.13.321
- 1597 [37] P.Higgs. “Broken Symmetries and the Masses of Gauge Bosons”. Physical Re-  
 1598 view Letters. 13 (16): 508-509,(1964). doi:10.1103/PhysRevLett.13.508.

- 1599 [38] G.Guralnik, C.R. Hagen and T.W.B. Kibble. “Global Conservation Laws  
 1600 and Massless Particles”. Physical Review Letters. 13 (20): 585-587, (1964).  
 1601 doi:10.1103/PhysRevLett.13.585.
- 1602 [39] CMS collaboration. “Observation of a new boson at a mass of 125 GeV with  
 1603 the CMS experiment at the LHC”. Physics Letters B. 716 (1): 30-61 (2012).  
 1604 arXiv:1207.7235. doi:10.1016/j.physletb.2012.08.021
- 1605 [40] ATLAS collaboration. “Observation of a New Particle in the Search for the Stan-  
 1606 dard Model Higgs Boson with the ATLAS Detector at the LHC”. Physics Letters  
 1607 B. 716 (1): 1-29 (2012). arXiv:1207.7214. doi:10.1016/j.physletb.2012.08.020.
- 1608 [41] ATLAS collaboration; CMS collaboration (26 March 2015). “Combined Mea-  
 1609 surement of the Higgs Boson Mass in pp Collisions at  $\sqrt{s}=7$  and 8 TeV with  
 1610 the ATLAS and CMS Experiments”. Physical Review Letters. 114 (19): 191803.  
 1611 arXiv:1503.07589. doi:10.1103/PhysRevLett.114.191803.
- 1612 [42] CMS Collaboration, “SM Higgs Branching Ratios and To-  
 1613 tal Decay Widths (up-date in CERN Report4 2016)”.  
 1614 <https://twiki.cern.ch/twiki/bin/view/LHCPhysics/CERNYellowReportPageBR>  
 1615 , last accessed on 17.12.2017.
- 1616 [43] R.Grant V. “Determination of Higgs branching ratios in  $H \rightarrow W^+W^- \rightarrow l^+l^- jj$  and  $H \rightarrow ZZ \rightarrow l^+l^- jj$  channels”. Physics Department, Uni-  
 1617 versity of Tennessee (Dated: October 31, 2012). Retrieved from  
 1618 <http://aesop.phys.utk.edu/ph611/2012/projects/Riley.pdf>
- 1620 [44] LHC Higgs Cross Section Working Group, Denner, A., Heinemeyer, S. et al.  
 1621 “Standard model Higgs-boson branching ratios with uncertainties”. Eur. Phys.  
 1622 J. C (2011) 71: 1753. <https://doi.org/10.1140/epjc/s10052-011-1753-8>

- 1623 [45] LHC InternationalMasterclasses“When protons collide”. Retrieved from  
 1624 [http://atlas.physicsmasterclasses.org/en/zpath\\_protoncollisions.htm](http://atlas.physicsmasterclasses.org/en/zpath_protoncollisions.htm)
- 1625 [46] F. Maltoni, K. Paul, T. Stelzer, and S. Willenbrock, “Associated production  
 1626 of Higgs and single top at hadron colliders”, Phys.Rev. D64 (2001) 094023,  
 1627 [hep-ph/0106293].
- 1628 [47] S. Biswas, E. Gabrielli, F. Margaroli, and B. Mele, “Direct constraints on the  
 1629 top-Higgs coupling from the 8 TeV LHC data,” Journal of High Energy Physics,  
 1630 vol. 07, p. 073, (2013).
- 1631 [48] M. Farina, C. Grojean, F. Maltoni, E. Salvioni, and A. Thamm, “Lifting de-  
 1632 generacies in Higgs couplings using single top production in association with a  
 1633 Higgs boson,” Journal of High Energy Physics, vol. 05, p. 022, (2013).
- 1634 [49] T.M. Tait and C.-P. Yuan, “Single top quark production as a window to physics  
 1635 beyond the standard model”, Phys. Rev. D 63 (2000) 014018 [hep-ph/0007298].
- 1636 [50] F. Demartin, F. Maltoni, K. Mawatari, and M. Zaro, “Higgs production in  
 1637 association with a single top quark at the LHC,” European Physical Journal C,  
 1638 vol. 75, p. 267, (2015).
- 1639 [51] CMS Collaboration, “Modelling of the single top-quark pro-  
 1640 duction in association with the Higgs boson at 13 TeV.”  
 1641 <https://twiki.cern.ch/twiki/bin/viewauth/CMS/SingleTopHiggsGeneration13TeV>,  
 1642 last accessed on 16.01.2018.
- 1643 [52] CMS Collaboration, “SM Higgs production cross sections at  $\sqrt{s} = 13$  TeV.”  
 1644 <https://twiki.cern.ch/twiki/bin/view/LHCPhysics/CERNYellowReportPageAt13TeV>, last  
 1645 accessed on 16.01.2018.

- 1646 [53] S. Dawson, The effective W approximation, Nucl. Phys. B 249 (1985) 42.
- 1647 [54] S. Biswas, E. Gabrielli and B. Mele, JHEP 1301 (2013) 088 [arXiv:1211.0499  
1648 [hep-ph]].
- 1649 [55] F. Demartin, B. Maier, F. Maltoni, K. Mawatari, and M. Zaro, “tWH associated  
1650 production at the LHC”, European Physical Journal C, vol. 77, p. 34, (2017).  
1651 arXiv:1607.05862
- 1652 [56] LHC Higgs Cross Section Working Group, “Handbook of LHC Higgs Cross  
1653 Sections: 4.Deciphering the Nature of the Higgs Sector”, arXiv:1610.07922.
- 1654 [57] J. Ellis, D. S. Hwang, K. Sakurai, and M. Takeuchi.“Disentangling Higgs-Top  
1655 Couplings in Associated Production”, JHEP 1404 (2014) 004, [arXiv:1312.5736].
- 1656 [58] CMS Collaboration, V. Khachatryan et al., “Precise determination of the mass  
1657 of the Higgs boson and tests of compatibility of its couplings with the standard  
1658 model predictions using proton collisions at 7 and 8 TeV,” arXiv:1412.8662.
- 1659 [59] ATLAS and CMS Collaborations, “Measurements of the Higgs boson produc-  
1660 tion and decay rates and constraints on its couplings from a combined ATLAS  
1661 and CMS analysis of the LHC pp collision data at  $\sqrt{s} = 7$  and 8 TeV,” (2016).  
1662 CERN-EP-2016-100, ATLAS-HIGG-2015-07, CMS-HIG-15-002.
- 1663 [60] File:Cern-accelerator-complex.svg. Wikimedia Commons,  
1664 the free media repository. Retrieved January, 2018 from  
1665 <https://commons.wikimedia.org/wiki/File:Cern-accelerator-complex.svg>
- 1666 [61] J.L. Caron , “Layout of the LEP tunnel including future LHC infrastructures.”,  
1667 (Nov, 1993). A C Collection. Legacy of AC. Pictures from 1992 to 2002. Re-  
1668 retrieved from <https://cds.cern.ch/record/841542>

- 1669 [62] M. Vretenar, “The radio-frequency quadrupole”. CERN Yellow Report CERN-  
1670 2013-001, pp.207-223 DOI:10.5170/CERN-2013-001.207. arXiv:1303.6762
- 1671 [63] L.Evans. P. Bryant (editors). “LHC Machine”. JINST 3 S08001 (2008).
- 1672 [64] CERN Photographic Service.“Radio-frequency quadrupole, RFQ-1”, March  
1673 1983, CERN-AC-8303511. Retrieved from <https://cds.cern.ch/record/615852>.
- 1674 [65] CERN Photographic Service “Animation of CERN’s accelerator net-  
1675 work”, 14 October 2013. DOI: 10.17181/cds.1610170 Retrieved from  
1676 <https://videos.cern.ch/record/1610170>
- 1677 [66] C.Sutton. “Particle accelerator”.Encyclopedia Britannica. July 17, 2013. Re-  
1678 trieved from <https://www.britannica.com/technology/particle-accelerator>.
- 1679 [67] L.Guiraud. “Installation of LHC cavity in vacuum tank.”. July 27 2000. CERN-  
1680 AC-0007016. Retrieved from <https://cds.cern.ch/record/41567>.
- 1681 [68] J.L. Caron, “Magnetic field induced by the LHC dipole’s superconducting coils”.  
1682 March 1998. AC Collection. Legacy of AC. Pictures from 1992 to 2002. LHC-  
1683 PHO-1998-325. Retrieved from <https://cds.cern.ch/record/841511>
- 1684 [69] AC Team. “Diagram of an LHC dipole magnet”. June 1999. CERN-DI-9906025  
1685 retrieved from <https://cds.cern.ch/record/40524>.
- 1686 [70] CMS Collaboration “Public CMS Luminosity Information”.  
1687 [https://twiki.cern.ch/twiki/bin/view/CMSPublic/LumiPublicResults#2016\\_proton\\_proton](https://twiki.cern.ch/twiki/bin/view/CMSPublic/LumiPublicResults#2016_proton_proton)  
1688 last accessed 24.01.2018
- 1689 [71] J.L Caron. “LHC Layout” AC Collection. Legacy of AC. Pictures  
1690 from 1992 to 2002. September 1997, LHC-PHO-1997-060. Retrieved from  
1691 <https://cds.cern.ch/record/841573>.

- 1692 [72] CMS Collaboration. “The CMS experiment at the CERN LHC” JINST 3 S08004  
1693 (2008).
- 1694 [73] CMS Collaboration. “CMS detector drawings 2012” CMS-PHO-GEN-2012-002.  
1695 Retrieved from <http://cds.cern.ch/record/1433717>.
- 1696 [74] R. Breedon. “View through the CMS detector during the cooldown of the  
1697 solenoid on February 2006. CMS Collection”, February 2006, CMS-PHO-  
1698 OREACH-2005-004, Retrieved from <https://cds.cern.ch/record/930094>.
- 1699 [75] A. Dominguez et. al. “CMS Technical Design Report for the Pixel Detector  
1700 Upgrade”, CERN-LHCC-2012-016. CMS-TDR-11.
- 1701 [76] CMS Collaboration. “Description and performance of track and primary-vertex  
1702 reconstruction with the CMS tracker,” Journal of Instrumentation, vol. 9, no.  
1703 10, p. P10009,(2014).
- 1704 [77] CMS Collaboration and M. Brice. “Images of the CMS Tracker Inner  
1705 Barrel”, November 2008, CMS-PHO-TRACKER-2008-002. Retrieved from  
1706 <https://cds.cern.ch/record/1431467>.
- 1707 [78] M. Weber. “The CMS tracker”. 6th international conference on hyperons, charm  
1708 and beauty hadrons Chicago, June 28-July 3 2004.
- 1709 [79] CMS Collaboration. “Projected Performance of an Upgraded CMS Detector at  
1710 the LHC and HL-LHC: Contribution to the Snowmass Process”. Jul 26, 2013.  
1711 arXiv:1307.7135
- 1712 [80] L. Veillet. “End assembly of HB with EB rails and rotation in-  
1713 side SX ”,January 2002. CMS-PHO-HCAL-2002-002. Retrieved from  
1714 <https://cds.cern.ch/record/42594>.

- 1715 [81] J. Puerta-Pelayo.“First DT+RPC chambers installation round in the  
 1716 UX5 cavern.”. January 2007, CMS-PHO-OREACH-2007-001. Retrieved from  
 1717 <https://cds.cern.ch/record/1019185>
- 1718 [82] CMS Collaboration, “Search for the associated production of a Higgs boson  
 1719 with a single top quark in proton-proton collisions at  $\sqrt{s} = 8$  TeV”, JHEP 06  
 1720 (2016) 177,doi:10.1007/JHEP06(2016)177, arXiv:1509.08159.
- 1721 [83] B. Stieger, C. Jorda Lope et al., “Search for Associated Production of a Single  
 1722 Top Quark and a Higgs Boson in Leptonic Channels”, CMS Analysis Note CMS  
 1723 AN-14-140, 2014.
- 1724 [84] M. Peruzzi, C. Mueller, B. Stieger et al., “Search for ttH in multilepton final  
 1725 states at  $\sqrt{s} = 13$  TeV”, CMS Analysis Note CMS AN-16-211, 2016.
- 1726 [85] CMS Collaboration, “Search for H to bbar in association with a single top quark  
 1727 as a test of Higgs boson couplings at  $\sqrt{s} = 13$  TeV”, CMS Physics Analysis  
 1728 Summary CMS-PAS-HIG-16-019, 2016.
- 1729 [86] B. Maier, “SingleTopHiggProduction13TeV”, February, 2016.  
 1730 <https://twiki.cern.ch/twiki/bin/viewauth/CMS/SingleTopHiggsGeneration13TeV>.
- 1731 [87] M. Peruzzi, F. Romeo, B. Stieger et al., “Search for ttH in multilepton final  
 1732 states at  $\sqrt{s} = 13$  TeV”, CMS Analysis Note CMS AN-17-029, 2017.
- 1733 [88] B. WG, “BtagRecommendation80XReReco”, February, 2017.  
 1734 <https://twiki.cern.ch/twiki/bin/view/CMS/BtagRecommendation80XReReco>.